Remotely-sensed rip current dynamics and morphological control in high-energy beach environments

Isaac Rodriguez Padilla

université de BORDEAUX

THÈSE PRÉSENTÉE

POUR OBTENIR LE GRADE DE

DOCTEUR DE

L'UNIVERSITÉ DE BORDEAUX

ÉCOLE DOCTORALE: Sciences et Environnements (EDSE 304)

SPÉCIALITÉ: Physique de l'environnement

Par Isaac RODRÍGUEZ PADILLA

Télédétection par système vidéo de la dynamique des courants induits par les vagues et de l'évolution morphologique des plages soumises aux houles énergétiques

Sous la direction de : Bruno CASTELLE et Philippe BONNETON
Co-encadrant: Denis MORICHON

Soutenue le 30 septembre 2021

Membres du jury :

Stefan AARNINKHOF	Professeur	Delft University of Techonology	Rapporteur
Yann BALOUIN	Ingénieur de Recherche	BRGM	Rapporteur
Nadia SÉNÉCHAL	Professeure	Université de Bordeaux	Présidente
France FLOC'H	Maîtresse de Conférences	Université de Bretagne Occidentale	Examinatrice
Patricio CATALÁN	Maître de Conférences	Federico Santa María Technical University	Examinateur
Bruno CASTELLE	Directeur de Recherche CNRS	Université de Bordeaux	Directeur
Philippe BONNETON	Directeur de Recherche CNRS	Université de Bordeaux	Co-directeur
Denis MORICHON	Maître de Conférences	Université de Pau et des Pays de l'Adour	Co-encadrant
Vincent MARIEU	Ingénieur de Recherche CNRS	Université de Bordeaux	Invité

Titre : Télédétection par système vidéo de la dynamique des courants induits par les vagues et de l'evolution morpholoqique des plages soumises aux houles énergétiques

Résumé : Comprendre les circulations induites par les vagues et les évolutions morphologiques du littoral est important scientifiquement et répond à une forte demande sociétale. Toutefois l'acquisition de ces données sur le terrain est coûteuse et reste un véritable défi logistique. Le développement de la télédétection optique combiné à la démocratisation de plateformes vidéo et d'algorithmes ouverts d'analyse d'image permet maintenant d'obtenir à faible cout une grande quantité d'informations sur le littoral. Ce travail s'appuie sur techniques existantes en imagerie vidéo, et sur des nouveaux développements, afin d'inférer la bathymétrie de l'avant-côte et les courants dans la zone de déferlement. Les méthodes sont validées avec une campagne de mesures intensive sur la plage d'Anglet dans le sud-ouest de la France. Pour la première fois, l'évolution spatiale et temporelle à la fois des courants et de la morphologie de la plage sont étudiés en présence de vagues de tempête.

Mots clés : station vidéo; vagues de tempête; plages sableuses; courants d'arrachement; évolution morphologique; stabilisation d'images

Title : Remotely-sensed rip current dynamics and morphological control in high-energy beach environments

Abstract : Understanding the surf zone circulation and the morphological changes within the nearshore is essential for both scientific and societal interests. However, direct measurements with in-situ instruments are logistically challenging and expensive. The development of optical remote sensing techniques in combination with low-cost image platforms and open-source algorithms offers the possibility of collecting large amounts of information at a reasonable instrumental and computational cost. This work builds on existing and new video monitoring techniques to remotely sense the nearshore bathymetry as well as the surf zone circulation in a high-energy meso-macro tidal beach environment, including storm events. The methods are validated against a dense data set acquired during an intensive field campaign conducted at Anglet beach, SW France. For the first time the temporal and spatial variability of concurrent nearshore bathymetry and surface currents are addressed under high-energy wave forcing.

Keywords : video monitoring; storm waves; sandy beaches; rip currents; morphological change; image stabilization

UMR CNRS 5805 EPOC (Environnements et Paléoenvironnements Océaniques et Continentaux)
OASU – Université de Bordeaux
Allée Geoffroy Saint-Hilaire – CS 50025
33615 Pessac CEDEX – France

Dedication

To my friend Jacinto León Guzmán whose memory will last as long as the vast ocean

"Now he has departed from this strange world a little ahead of me. That means nothing. People like us, who believe in physics, know that the distinction between past, present and future is only a stubbornly persistent illusion."

Albert Einstein

Acknowledgments

Writing this last section of the manuscript means that this cycle is coming to an end. It has been a great adventure and experience to work surrounded by such brilliant minds with such humble and human personalities. Knowing that I was able to contribute my grain of sand by collaborating with such talented scientist fills me with pride and motivates me to continue on this (painful but satisfying) path of research. Although there are many people to thank, I would like to start with my wife Abril and my cat Simba, whose emotional support were essential in coping with the pandemic and the confinement while being far away from home.

Many persons have contributed to this work (either directly or indirectly) so I will try not to forget anyone. First of all, I'm eternally grateful to Bruno and Vincent for believing in me and giving me the freedom to explore my curiosity under their tutelage and expertise always in a good mood. Thanks Bruno for welcoming us into your home with your family even though we had a cat addicted to wrestling (apologies for the trauma caused to Osiris). You will always find a place in our home if you decide one day to visit Mexico. Thanks Vincent for your great ideas and suggestions and for always being available in case I got stuck with something (sorry for making you struggle using tmux and typing on my imaginary qwerty keyboard)... I guess you will be happy to know that the server (calcul02) will recover it's precious memory as soon as I'm gone ;)

In the same way I want to thank Philippe and Denis for providing me with supervision and insightful feedback. Thanks to all the METHYS team for integrating me as one of their members and all the kind staff in the EPOC Lab: Aldo, Isabel, Bertrand, Natalie, Guillaume and particularly Nadia Sénéchal for taking care of my administrative procedures with the university and being an active member along my PhD. I also want to thank the members of my jury (S. Aarninkhof, Y. Balouin, F. Floc'h and P. Catalán) for taking the time to read and review this thesis, as well as the persons who were present throughout my PhD in the evaluation committee (D. Sous and R. Almar).

I really enjoyed the opportunity to participate in Anglet 2018 field campaign (that was a really nice way to start my PhD) and collaborate with researchers from other institutions such as from the University of Plymouth and Université Pau et Pays de l'Adour. In this sense, I would like to thank J. McCarroll, T. Scott, A. Barrett and T. Poate for their valuable help in the field during drifter deployment. I would also wish to thank R. Holman, T. Liu, P. Dérian and E. Bergsma for their valuable comments along my PhD through email correspondence.

My sincere gratitude to all the PhD and Postdoc crew for always keeping the spirit up. Barbara, Cassandra, Mélanie and Quentin you were such a wonderful people! Thanks Arthur for all your help; I really enjoyed our hilarious conversations... It's sad that the research community and the world is not yet prepared to know about our

recently novel discovery "the penis rip" and the potential hazard of its flow (*that's what she said*). Thanks Kévin for all your support, I have no doubt that you have incredible skills and that you're an amazing researcher. I really admire your capacity to look beyond the data and the way you think out of the box, keep up the good work! I also enjoyed the good pre-covid times and the smooth atmosphere sharing the office with Elias and hanging around with Paulo and José, Brazilian ambassadors of the good life.

The return to normality after the pandemic allowed me to meet and interact with marvelous people. Thanks Carla for your patience in encouraging me to speak French without feeling uncomfortable. Marion, your mere presence always cheered me up. Junli, so kind and so cute. Olivier, always in good mood and ready for a beer. Among all the recent people I met in France, I would like to particularly thank Maurizio and Sophie for their genuine support, friendship and chill vibe... I really wish I had met you before and I will truly miss you (although I know we will meet again at some congress to catch up). *Hasta plus!*

Last but not least, I want to thank my parents Raúl and Yolanda for planting in me the seed of education, research and self-improvement (*una raya más al tigre*). I want also to thank my brother and sister, Josué and Erendira, and all my family back in Mexico for their endless support. I'm very grateful to Amaia Ruiz De Alegría-Arzaburu and the MORDICS team who supported me from the beginning and throughout the PhD. Thanks to my friends Ixetl and Aimie for helping me dealing with all the French administrative process and encouraging me to come to France. Thanks to Marco, Jessica and the recent member of the family, Marquito, for joining the experience of living in France. I wish to express my appreciation to all the crew from CICESE and UABC-IIO who generate excellent human resources with international competitiveness.

Finally, I would like to thank the University of Bordeaux for hosting me, and I would especially like to thank the Mexican government and CONACYT for granting me a scholarship and giving me the opportunity to expand my knowledge and skills to which I will ultimately contribute to the benefit of my country.

– Thanks to all of you – Merci à vous tous – Gracias a todos ustedes –

Contents

List of Figures

List of Tables

Chapter 1

Introduction

Contents

1.1 General context

The nearshore zone, extending from the beach to water depths of the order of 10 to 20 m, is the region of the coast where the forces of the sea react against the land (Simm et al., 1996). Although the nearshore zone constitutes only 10^{-3} of the ocean's surface area, it is a critical resource for recreation, industry, commerce and defense (Holman and Haller, 2013). Apart from these societal interests, the nearshore zone embodies a significant research interest since it is a highly dynamic environment where processes of circulation and sediment transport occur (Perkovic, 2008). Wave-induced currents transport and mix sediment, nutrients and pollutants along the surf zone and the offshore influencing the nearshore morphology at spatiotemporal scales of hours to decades and meters to tens of kilometers (Aarninkhof, 2003).

Along open sandy beaches longshore currents are produced under oblique incident waves (Figure 1.1a) and rip currents and associated circulation cell systems are produced mostly under near shore-normally incident waves (Figure 1.1b). Rip currents are narrow and concentrated seaward-directed flows that extend from close to the shoreline, through the surf zone, and varying distances beyond. Although rip currents and associated circulations are essentially driven by wave breaking, they are also controlled by beach morphology and modulated by the tide, thus resulting in a broad family of rips with different mechanisms and behaviors (Castelle et al., 2016b).

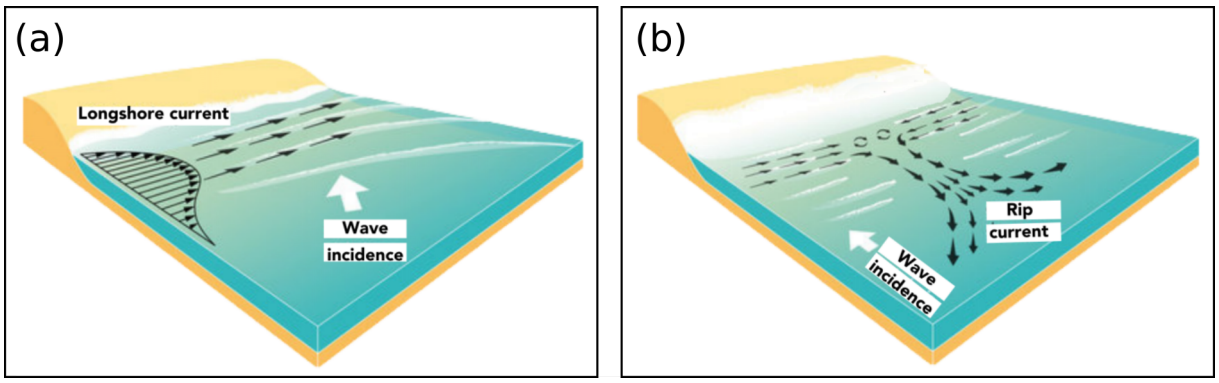

Figure 1.1 – Schematic of the flow patterns of a **(a)** longshore current and a **(b)** rip current under different angles of wave incidence. Figure modified from Winckler (2020).

The mutual adjustment between hydrodynamic processes and morphology towards and equilibrium relationship is what is known as morphodynamics (Wright and Thom, 1977). The morphodynamic system within the nearshore can be considered to be composed of two main interdependent components: the dynamics of a wave field over the shoaling bathymetry of a beach, and the reciprocal response through sediment transport of the beach bathymetry to that wave field (also influenced by tidal forcing) (Holman et al., 1993). The ability to capture the spatial and temporal variations in mean flows in the surf zone is key to predicting the morphological change of the nearshore topography and shoreline (Perkovic, 2008). Although the nearshore circulation along open sandy beaches is relatively well known (Jackson and Short, 2020), the coupled rip current morphodynamic system under high-energy wave forcing is still poorly understood (Castelle et al., 2016b). This is particularly true for geologically-constrained beaches containing features such as headlands or reefs (Mouragues et al., 2020b).

An explanation for this lack of quantitative understanding is that most of the studies in the nearshore zone are based on short-term field measurements, therefore limiting the range of wave, tide and morphological conditions. In situ instruments are typically deployed only for a short duration in single sparse points. Although measurements are very accurate, the deployment of instruments is expensive, time-consuming and logistically complicated, particularly under high-energetic wave-dominated beach environments. For storm events, breaking waves in the surf zone are violent and wave-driven currents can be strong, which makes work in the surf zone dangerous to both people and instruments (Holman and Haller, 2013). Moreover, fixed instruments are difficult to maintain since they can be buried over surprisingly short periods due to large morphological changes in sandy bottoms.

The previous limitations led to the concept of using remote sensing techniques to transform signals from different sensors into geophysical data in order to infer nearshore hydrodynamic and morphological processes away from the hostile marine conditions (Holman et al., 1993). Since many nearshore processes have optical signatures, video imaging offers the unique capability to collect high volumes of data at high temporal and spatial resolution over long periods with relatively low cost (Perugini et al., 2019). For this reason, shore-based video monitoring has been developed into a very popular method for sampling indirectly the nearshore environment (Holman and Stanley, 2007). It has become one of the fastest growing remote sensing techniques in the past 40 years due to its wider access by the international community. Examples of research-based video camera systems around the world are Argus (Holman et al., 1993), Cam-Era (www.niwa.co.nz), EVS (http://www.svm.it), Sirena (Nieto et al., 2010), COSMOS (Taborda and Silva, 2012), and Kosta (http://www.kostasystem.com). Typical standard image products derived from video systems are snapshot, 10-min averaged time-exposure images (timex), 10-min variance images and 10-min timestack images (pixel transect time series) (see Figure 1.2).

Figure 1.2 – Typical standard video-derived products. **(a)** Snapshot, **(b)** timex, **(c)** variance and **(d)** timestack image.

Oblique images can be transformed to a longshore/cross-shore local ground coordinate system through a standard photogrammetric transformation (Holland et al., 1997; Hartley and Zisserman, 2004). The mapping conversion (rectification) requires a camera calibration to correct lens distorsion effects and spatially distributed surveyed ground control points (GCPs) for georeferencing. When only one camera is used, the vertical coordinate of the projection is usually assigned to the instant sea level, which is usually retrieved from a nearby tide gauge or pressure sensor. As shown by the timex image in Figure 1.3, once the image is rectified, the visible signatures associated with nearshore morphological features can be analyzed and quantified.

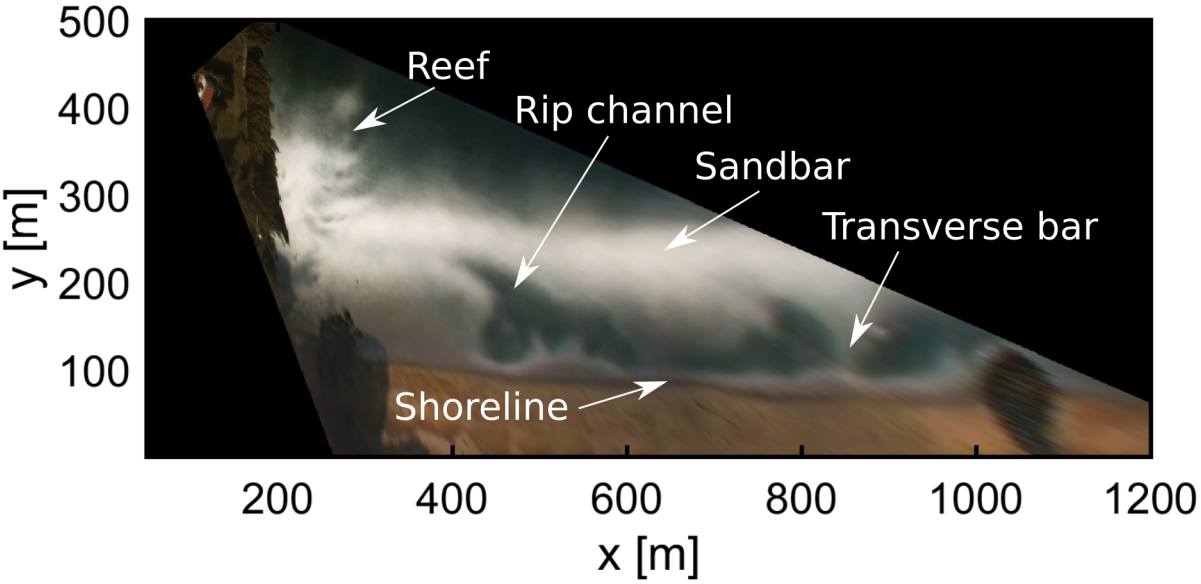

Figure 1.3 – Rectified timex image from Figure 1.2b emphasizing preferential wave breaking and depicting different nearshore morphological features.

The development of nearshore video techniques has taken place over many years. Optical signatures have been exploited to infer hydrodynamic processes such as surface currents and wave characteristics. For example, wave crests can be tracked to determine the wave celerity (Stockdon and Holman, 2000; Almar et al., 2009), the foam left by breaking waves can be used as a tracer to infer underlying currents (Chickadel et al., 2003; Almar et al., 2016; Dérian and Almar, 2017; Anderson et al., 2021) and the foam pixel intensity can be used as a proxy for wave dissipation (Aarninkhof and Ruessink, 2004). A summary of the key processes that have been examined by video remote sensing in the last decades with examples of related publications is shown in Table 1.1.

Table 1.1 – Key international research outcomes provided by video remote sensing. Modified from Splinter et al. (2018b).

Process	Example Publications
Shoreline behavior	Alexander and Holman (2004); Coco et al. (2005); Turner (2006); Davidson and Turner (2009) Pearre and Puleo (2009); Almar et al. (2012b); Davidson et al. (2013); Splinter et al. (2011b, 2014, 2017) Pianca et al. (2015)
Sandbar behavior	Plant et al. (1999); Van Enckevort and Ruessink (2003); van Enckevort et al. (2004) Ruessink et al. (2009); Castelle et al. (2010b); Pape et al. (2010); Splinter et al. (2011a, 2018a)
Nearshore morphology	Lippmann and Holman (1989, 1990); Price and Ruessink (2011, 2013)
Nearshore bathymetry	Stockdon and Holman (2000); Aarninkhof (2003); van Dongeren et al. (2008); Holman et al. (2013)
Inter-tidal topography	Holland and Holman (1997); Plant and Holman (1997); Aarninkhof and Roelvink (1999) Madsen and Plant (2001); Aarninkhof et al. (2003); Uunk et al. (2010); Didier et al. (2017)
Tidal inlet dynamics	Pianca et al. (2014); Harrison et al. (2017)
Rip current location and persistence	Bogle et al. (2001); Holman et al. (2006); Turner et al. (2007); Quartel (2009)
Nearshore wave celerity	Holland and Holman (1999); Stockdon and Holman (2000); Plant et al. (2008); Almar et al. (2009)
Nearshore wave angle	Holman and Chickadel (2005)
Nearshore wave dissipation	Lippmann and Holman (1989); Aarninkhof and Ruessink (2004); Aarninkhof et al. (2005)
Nearshore surface currents	Chickadel et al. (2003); Almar et al. (2016); Horstmann et al. (2017); Dérian and Almar (2017) Anderson et al. (2021); Rodríguez-Padilla et al. (2021)
Wave height from stereo pairs	De Vries et al. (2011); Shand et al. (2012); Vieira et al. (2020)
Swash characteristics	Stockdon and Holman (1996); Power et al. (2011); Senechal et al. (2011); Ibaceta et al. (2014) Palmsten and Splinter (2016); Blenkinsopp et al. (2016)
Dune erosion	Palmsten and Holman (2012)

Much effort has been dedicated to derive bathymetry maps from video imagery through the linear dispersion relationship for free surface waves. The cBathy algorithm (Holman et al., 2013) is nowadays the most popular algorithm to obtain two-dimensional bathymetries from video stations (Simarro et al., 2019). According to Holman et al. (2013), bathymetry maps are estimated with a typical accuracy of 10s of centimeters. Nevertheless, these estimates are obtained under quasi-ideal circumstances, e.g. micro tidal environment and moderate waves. As mentioned by Bergsma (2017), although the depth estimation technique is promising, it should be tested under more energetic wave conditions and larger tidal ranges since the accuracy depends to a large extent on the wave conditions; depth-inversion errors typically increase with increasing wave energy.

On the other hand, there is clear interest in the ability to directly measure currents and circulation in the nearshore (for example, for estimating longshore sediment transport and rip currents). It is important to note that prior to this manuscript (before 2018), existing works in the literature to determine two-dimensional surface currents from video imagery relied primarily on cross-correlation techniques, in particular using

particle image velocimetry (PIV; Adrian 1991; Holland et al. 2001). Within the surf zone, only a few studies were devoted to estimating surface currents (Chickadel et al., 2003; Almar et al., 2016), but only addressing the velocity component along a given transect. The work presented by Dérian and Almar (2017) shows the first attempt to optically derive two-dimensional surface currents using a technique common in the research field of computer vision based on optical flow. Part of the manuscript is inspired by the method proposed by Dérian and Almar (2017) which leads to the motivation to improve and fill the preceding knowledge gap of their work as it was designed to address surface flow in the swash.

Overall, the development and application of new concepts in video remote sensing techniques opens new perspective to monitor both surface currents (e.g., Dérian and Almar, 2017; Anderson et al., 2021) and the underlying bathymetry (e.g., Holman et al., 2013) on a high spatio-temporal scale, thus providing new insights into nearshore hydro- and morphodynamics processes.

1.2 Objectives and approach

The main aim of this work is to implement and develop optical remote sensing techniques to study nearshore morphodynamic and hydrodynamic processes under high-energetic wave conditions in a meso-macro tidal environment. For that purpose, Holman et al. (2013) cBathy algorithm and Liu (2017) optical flow algorithm are adapted in order to get nearshore bathymetry estimations as well as surf-zone surface velocities fields from high-sampled image sequences. An implicit objective is to seek image processing solutions that provide the highest accuracy in the final image product (e.g., image stabilization methods). These technical advances are then, as a preliminary study, used to address for the first time the temporal and spatial variability of nearshore circulation at a beach in southwest France under high-energy wave forcing.

1.3 Thesis outline

This manuscript is divided into six chapters and one appendix. Each chapter contains its own state of art for easier reading. The thesis is structured as follows:

- **Chapter 2: Field site and data.** We present the field site of La Petite Chambre d'Amour (PCA) beach, located in one of Anglet beaches (SW France) and describe the 3-week comprehensive field experiment carried out in October 2018.
- **Chapter 3: Image stabilization.** We investigate the impact of camera viewing angle deviation when monitoring the nearshore and present an efficient semi-automatic procedure to stabilize an image sequence using state-of-the-art techniques in order to remove unwanted camera movement after video acquisition.
- **Chapter 4: Nearshore bathymetric mapping from video imagery.** We apply a video-based linear depth inversion algorithm for three consecutive weeks (during daylight hours) to examine PCA beach morphological response under a wide range of wave and tide conditions.
- **Chapter 5: Optically derived wave-filtered surface currents.** We explore the potential to derive 2-D wave-filtered surface currents from video images by tracking the drifting foam, left after the passage of breaking waves, using an open-source optical flow algorithm.
- **Chapter 6: Conclusions and perspectives.** We summarize the concluding remarks and place the results in perspective for future investigation.

Chapter 2

Field site and data

Contents

2.1 Study site: La Petite Chambre d'Amour (PCA), Anglet Beach

The study site throughout this work is the beach of Anglet located on the Basque Coast in southwestern France (Figure 2.1). Anglet beach is a 4-km long sandy embayment delimited by a prominent 500-m long rocky headland (Cape Saint-Martin) in the South and by the southern Adour river training wall in the North. It is a major national and international tourism destination and a worldwide famous recognized surfing spot

(Benedet et al., 2007) that has been facing serious erosion issues over the last decades (Birrien et al., 2013). This has resulted in a number of coastal engineering works based on the implementation of coastal hard structures and beach nourishments to constrain shoreline variability. Anglet beach is structurally-engineered with 6 groins and 3 distinct sectors where the beach is backed by a seawall.

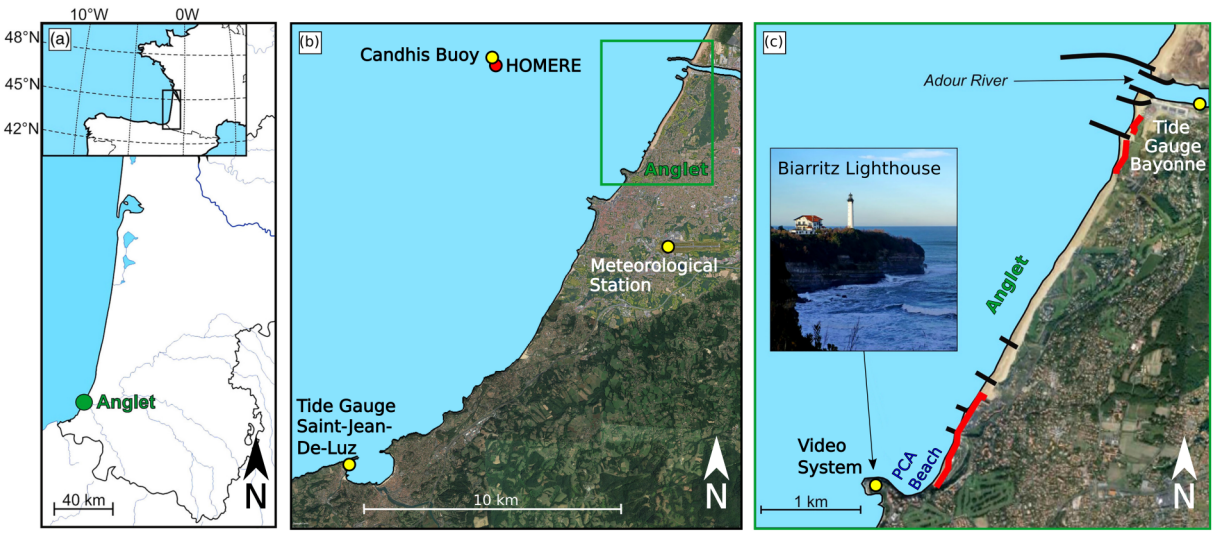

Figure 2.1 – (**a**) Location of Anglet along the Aquitaine south coast (SW France). (**b**) Location of available in situ instruments (yellow dots) and modelled wave data from HOMERE database (red dot). (**c**) Map of Anglet beach showing the location of the groins (black thick lines), the Adour river, the tide gauge from Bayonne and the video system (yellow dots), as well as a photo of Saint-Martin headland with the Biarritz lighthouse on which the video stations have been mounted. The red line indicates where the beach is backed by a seawall.

This study is primarily focused on the 3-week field experiment (October 2018) carried out in one of Anglet beaches, La Petite Chambre d'Amour (PCA) beach, located at the southern end of Anglet beach (Figure 2.7). PCA beach is bounded by the Saint-Martin rocky headland in the South and a 90-m long groin in the North. It is characterized by the presence of an approximately 20-m wide complex natural submerged rocky reef which exerts persistent wave breaking and occasionally bathymetrically-controlled rips at low tide under low-energy waves (Mouragues et al., 2020b).

The following subsections provide an overall description of the field site environmental conditions. The reader is also referred to subsections 3.3.3 and 5.3.4 for a summarized description of the field site and data used within the published research articles in the Journal of *Remote Sensing*.

2.1.1 Tide and wave forcing

There is no tide gauge at Anglet beach. The nearest tide gauges are the Bayonne-Boucau tide gauge, located within the mouth of the Adour river at 4 km north of PCA beach, and the Saint-Jean-De-Luz Socoa tide gauge, located 15 km southwest of the study site (see Figure 2.1). In this study, hourly water level measurements were retrieved from Saint-Jean-De-Luz Socoa tide gauge from SHOM website (https://data.shom.fr). Data from the Saint-Jean-De-Luz Socoa tide gauge were preferred to those from the Bayonne-Boucau tide gauge to avoid the influence of the Adour river discharge on the water level measurements. Figure 2.2 shows Saint-Jean-De-Luz reconstructed astronomical tide from 2010 to 2020 along with the tidal parameters indicating different mean water level positions with respect to the mean sea level (MSL). The tide is semi-diurnal (average period of 12 h 20 min) and is characterized by a meso-macro tidal regime with an average tidal range varying between 1.69 m (for neap tides) and 3.94 m (for spring tides).

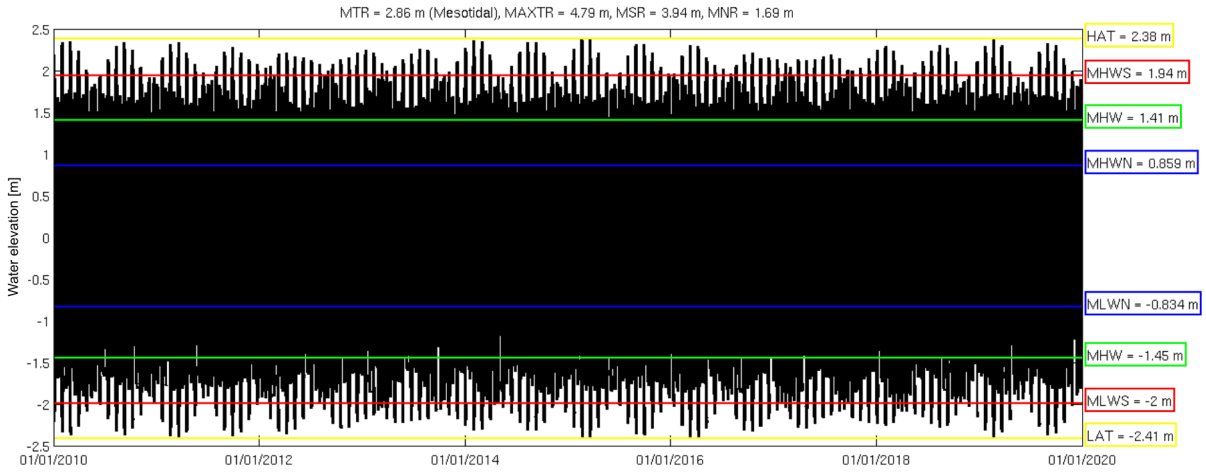

Figure 2.2 – Astronomical tide time series computed from Saint-Jean-De-Luz tide gauge. Water elevation is relative to the mean sea level.

In situ wave measurements were retrieved from a permanent directional wave buoy, CANDHIS (Centre d'Archivage National de Données de Houle In Situ; http://candhis.cetmef.developpement-durable.gouv.fr), located approximately 6 km offshore from the study site and moored in 50-m water depth (Figure 2.1). Wave parameters such as the significant wave height H_s, peak period T_p and the peak wave angle of incidence θ_p were collected every 30 min by the Candhis buoy from January 2013 to September

2018. In addition, hourly wave parameters were retrieved from HOMERE database (http://marc.ifremer.fr/produits/rejeu_d_etats_de_mer_homere) in order to fill the gaps present in Candhis time series (Figure 2.3a,b). The HOMERE database (Boudière et al., 2013; Accensi and Maisondieu, 2015) is a hindcast of oceanographical parameters covering the period 1994–2017. Outcomes are produced by WAVEWATCH III model (Tolman, 1991) over a high-resolution grid comprising the Channel - Bay of Biscay area. HOMERE wave data was extracted from the grid point located 300 meters away from the Candhis wave buoy position (see Figure 2.1). Following Castelle et al. (2014b), HOMERE significant wave height $H_{s_{\text{HOMERE}}}$ was corrected via a linear regression using Candhis buoy data $H_{s_{HOMERE}}$, as shown in Figure 2.3c and 2.4a.

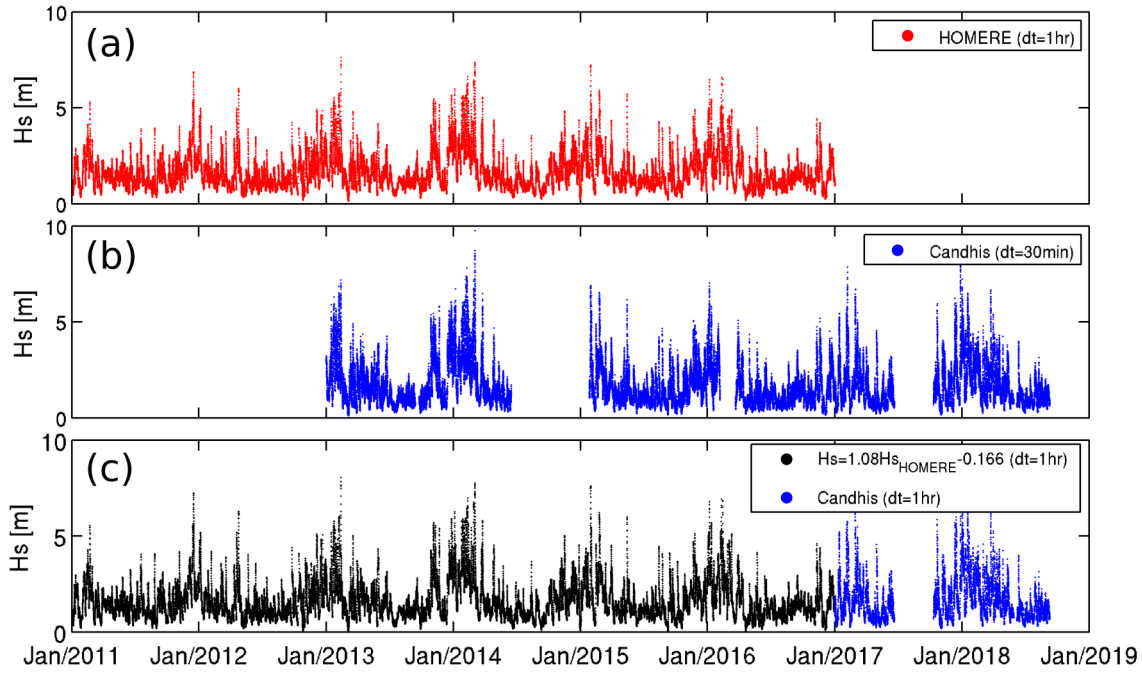

Figure 2.3 – Offshore significant wave height H_s long-term time series. H_s is displayed every 60- and 30-min using (**a**) HOMERE and (**b**) Candhis wave data, respectively. (**c**) Corrected significant wave height $H_s = 1.08H_{s_{HOMERE}} - 0.166$ (black line) merged with Candhis subsampled (60-min) wave data (blue line). The corresponding scatter diagram is shown in Figure 2.4.

Anglet beach is predominantly exposed to incident shore-normal high-energetic Atlantic swells coming from the WNW direction ($\bar{\theta}_p \approx 300°$; Figure 2.4b) generated by extra-tropical low-pressure systems tracking eastwards (Castelle et al., 2017b). The coast also experiences more variable locally generated wind waves (Abadie et al., 2005).

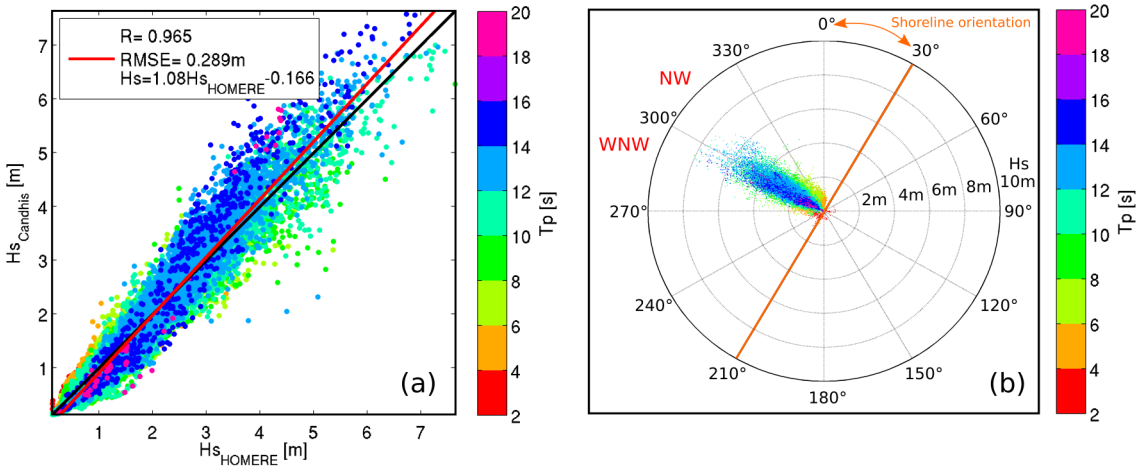

Figure 2.4 – (**a**) Scatter diagram of measured significant wave height at the Candhis buoy ($H_{s_{Candhis}}$) versus modelled significant wave height ($H_{s_{HOMERE}}$), with the red line indicating the linear regression giving $H_s = 1.08 H_{s_{HOMERE}} - 0.166$ and the black line the 1:1 perfect match. (**b**) Resulting scattered directional plot of significant wave height H_s for the long-term dataset (see Figure 2.3). The orange line indicates the 30° shoreline orientation at Anglet.

The incident wave energy is strongly seasonally modulated, with an annual mean significant wave height and peak period of $H_s = 1.57$ m and $T_p = 10$ s, respectively. The wave data present numerous storm events, including the outstanding winter of 2013/2014 (Castelle et al., 2015; Masselink et al., 2016), which resulted in waves up to 10 m height causing serious beach erosion and sea defense damage (Figure 2.5). Tide-induced currents are weak along the Anglet shore and breaking waves are by far the dominant driver of nearshore currents, with tide elevation affecting breaking patterns and in turn modulating nearshore currents (Sous et al., 2020).

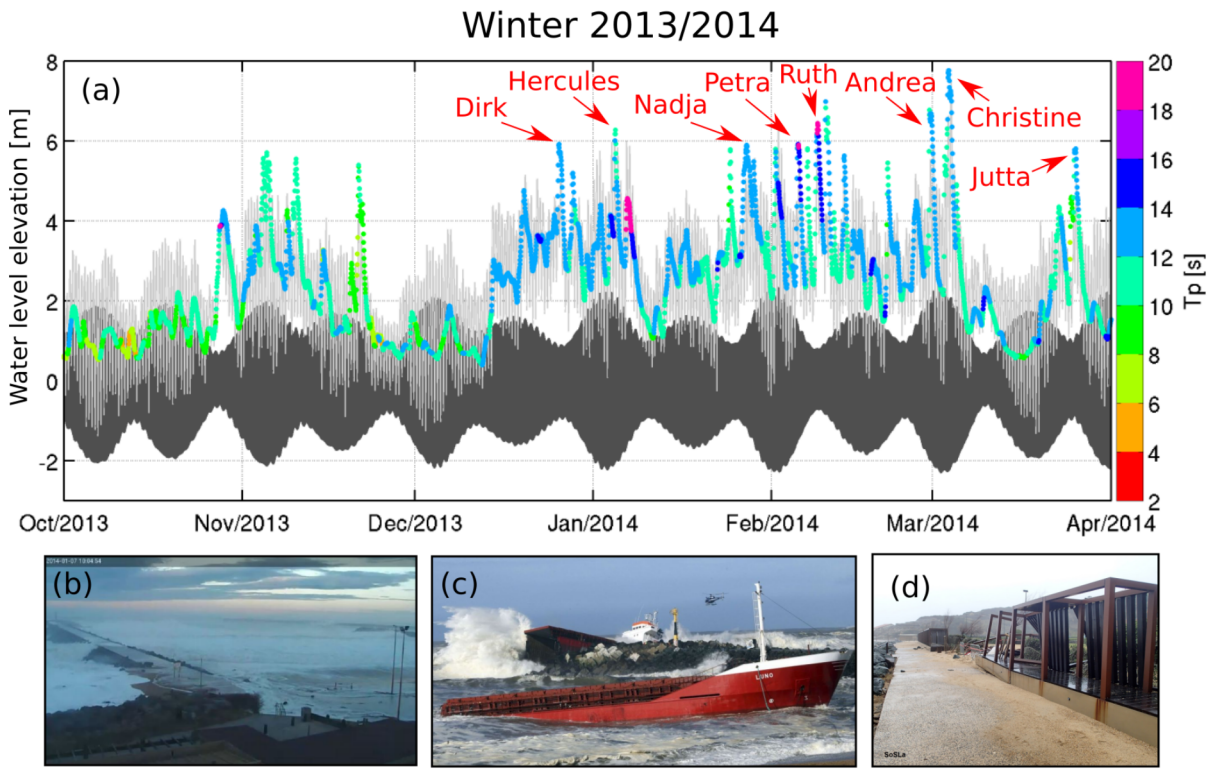

Figure 2.5 – Water level elevation time series during the outstanding winter of 2013/2014 computed from Saint-Jean-De-Luz tide gauge and Candhis offshore buoy (Figure 2.1). (**a**) Astronomical tide (dark gray filled area), total water level (TWL) defined as the sum of the astronomical tide and the vertical runup (light gray line) and significant wave height H_s with colors indicating the corresponding peak wave period T_p. The name of the most significant winter storms are indicated with red color. Snapshots during (**b**) storm "Hercules" (Jan 6, 2014), (**a**) storm "Petra" (Feb 5, 2014) and (**c**) storm "Christine" (Mar 3, 2014) causing flooding, serious erosion, infrastructure damage and even a shipwrecking in Anglet beach.

2.1.2 Morphology

According to Wright and Short (1984) classification, Anglet is a high energy intermediate beach with the presence of a seasonally modulated double-bar (occasionally single-bar) system (Huguet et al., 2016). Anglet beach is characterized by a non-dimensional embayment scaling parameter (Castelle and Coco, 2012) $\delta \approx 40$ and is therefore characterized by a normal beach circulation (Short and Masselink, 1999), meaning that Anglet beach tends to behave as an open coast, except close to the headland where PCA beach is located (Birrien et al., 2013). The beach is composed of medium to coarse sand ($D_{50} \approx 2$ mm) with a steep beach face ($\tan\beta \approx 1/10$) and a more gentle sloped surf zone ($\tan\beta \approx 1/50$) (Mouragues et al., 2020b). The relatively steep beach face

favors the formation of beach cusps with shoreline dynamics strongly controlled by the geometry of the surf-zone sandbar (Birrien et al., 2013).

Unlike the open sandy beaches along the northern Aquitaine coast, the Basque coastline is characterized by ubiquitous headlands exposing rocky substratum and coastal structures such as groins and training walls (Huguet et al., 2016). PCA beach in particular is barred with prominent inherited geology, characterized by the presence of a 500-m headland, bordered by rocks that emerge around low tide, and a natural submerged reef located approximately 150 m from the headland (Figure 2.7). These two morphological characteristics play an important role on beach circulation inducing headland rips and bathymetrically controlled rips with a potential competition/combination between one another that can favor sediment transport and headland bypassing (McCarroll et al., 2018; Mouragues et al., 2020b).

2.1.3 Biarritz lighthouse video monitoring system

In January 2013, a permanent video system composed of three cameras was installed on the top of Biarritz lighthouse (70 m above mean sea level) located near the tip of Saint-Martin headland (Figure 2.6). The combined video cameras monitor about 2 km of the southern beach that includes PCA beach and four groins. Each camera provides different image products in the daylight. From September 2013 to February 2017, single snapshot images, 10-min averaged time-exposure images (timex), 10-min variance images and 10-min timestack images (e.g., Figure 1.2) were collected every 20 min at 1 Hz. In March 2017, the configuration changed. From April 2017 to the present, images products were collected every 15 min at 1 Hz during an average period of sampling of 14 min. Moreover, since 2017, an additional single video camera was installed at the same location. This camera can, on demand, acquire continuously high-frequency (1 Hz) video images during particular events such as the field campaign of October 2018. However, the video-monitoring area of this camera comprises only PCA beach (Figure 2.6 and 2.7).

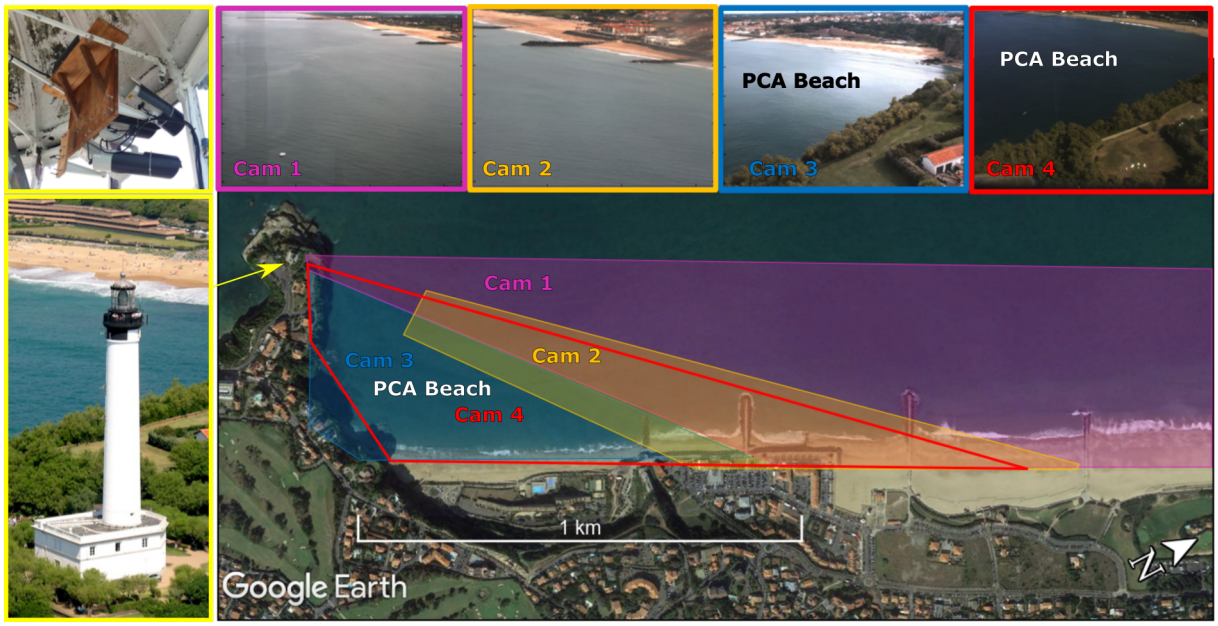

Figure 2.6 – Study site showing the video monitoring area and corresponding field of view of each camera. The fixed camera video system is installed at the top of Biarritz lighthouse near the tip of the headland. Cam 1, 2 and 3 provide standard video products every 20 min and cam 4 collects, on demand, continuously high-frequency (1 Hz) images.

2.2 October 2018 field experiment

An intensive field campaign was conducted at PCA beach from 3 to 26 October 2018 under a range of energetic wave conditions including a spring tide cycle (Figure 2.8). The 3-week field experiment was carried out in the frame of the MEPELS project, performed under the auspices of the DGA and led by SHOM. The experiment involved the collaboration of teams from three different laboratories (EPOC-University of Bordeaux, Coastal Marine Applied Research CMAR-University of Plymouth and SIAME-University of Pau and Pays de l'Adour) that coordinated the deployment and data collection of a large array of instruments including: four current profilers, six surf-zone drifters, topo-bathymetric surveys, image acquisition from a fixed video-camera and a camera-equipped Unmmaned Aerial Vehicle (UAV), as well as continuous tide, wave and wind data collection from nearby in situ stations (Figure 2.1 and 2.7). The following subsections describe the instruments and data collected during the three-week field experiment. The works of Mouragues et al. (2020a,b) provide a detailed analysis of PCA beach wave-induced circulation during October 2018 field campaign.

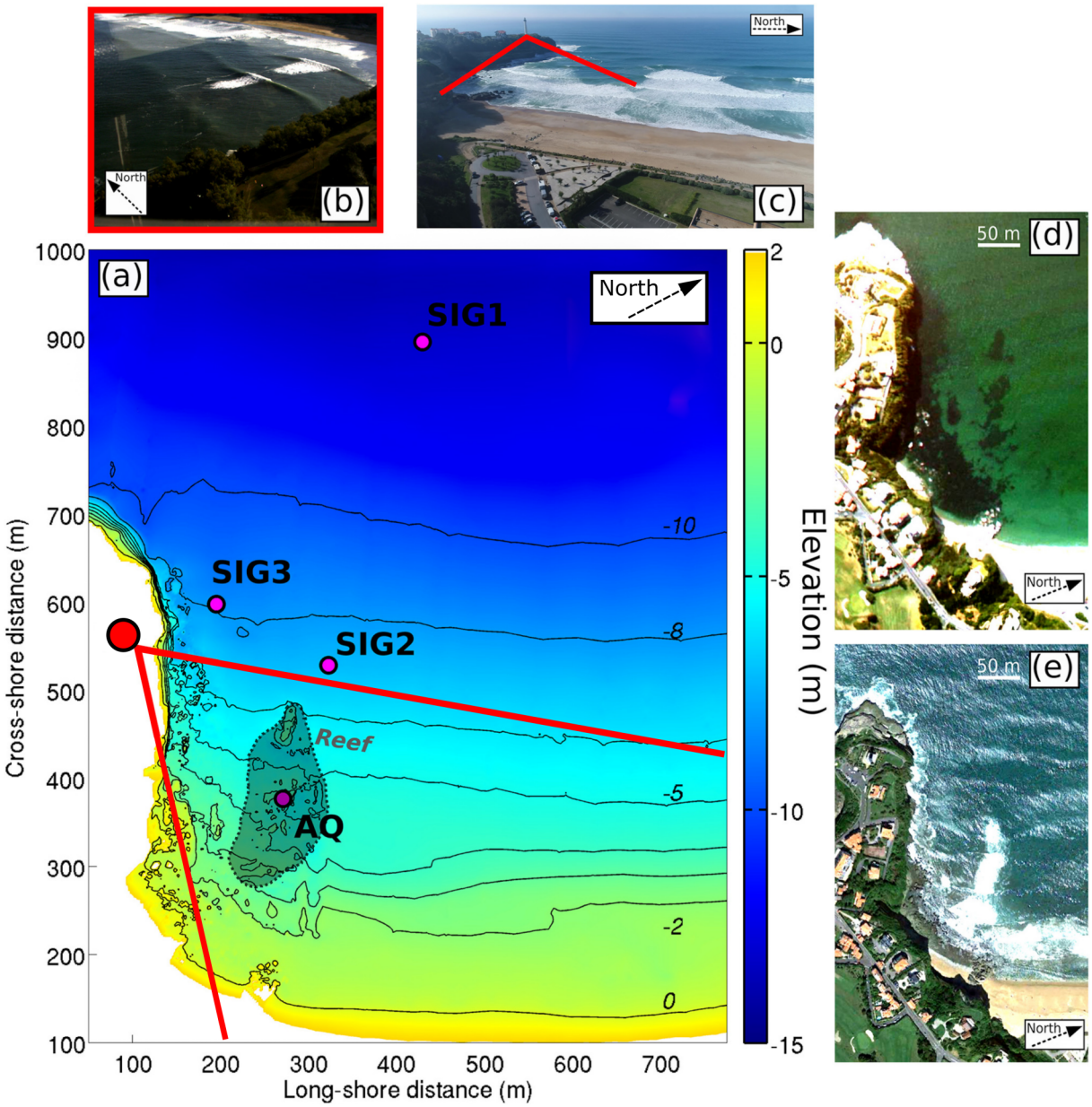

Figure 2.7 – Experimental setup of October 2018 field campaign at PCA beach (modified from Mouragues et al. 2020b). (**a**) Bathy-topo map of the field site during the begining of the experiment. Color represents elevation (m) in NGF-IGN69 (Global French Leveling). Magenta dots indicate the location of each current profiler. The shaded area and the red dot show the location of the reef and the lighthouse, respectively. Red lines indicate the headland-based camera field of view. (**b**) Example of a raw image recorded by the headland-based camera. (**c**) Aerial view of the field site. Google Earth images showing the headland and the submerged reef during low-energy wave conditions (**d**) and moderate-energy wave conditions (**e**).

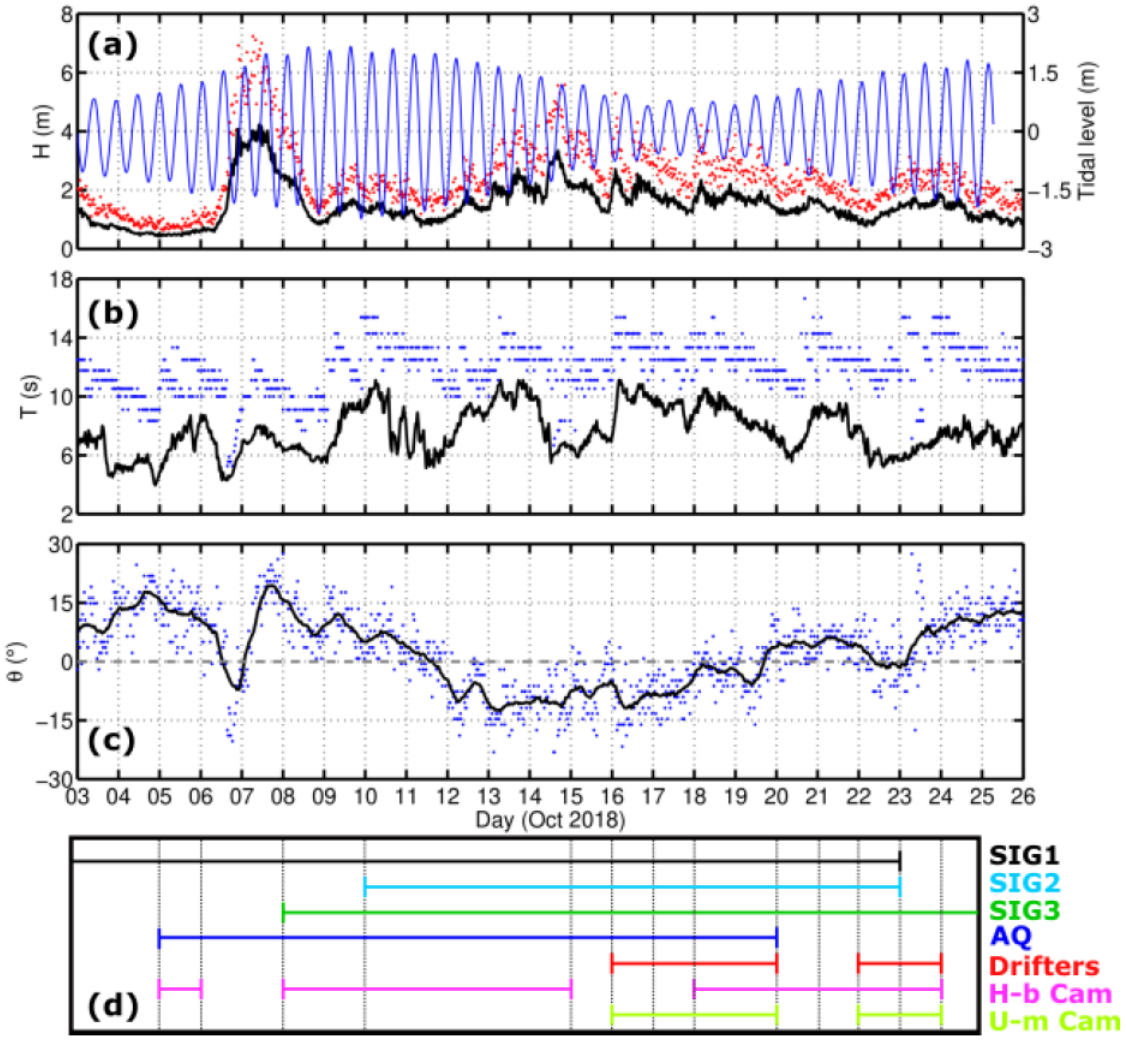

Figure 2.8 – Offshore wave and tide conditions during October 2018 field experiment at PCA beach (extracted from Mouragues et al. 2020b). (**a**) Tidal level (blue line), significant wave height (H_s; black line) and maximum wave height (H_{max}; red dots). (**b**) Peak wave period (T_p; blue dots) and mean wave period (T_{m02}; black line). (**c**) Peak wave incidence relative to shore normal (θ_p; blue dots) and its 12 h-averaged values (black line). (**d**) Deployment schedule for each measurement item. H-b Cam and U-m Cam stand for the headland-based and the UAV-mounted camera, respectively.

2.2.1 Topography and bathymetry data

An initial multi-beam bathymetric survey was conducted on 26 June 2018 to map the submerged reef and surrounding rocks of the headland. Two additional mono-beam bathymetric surveys with cross-shore transects spaced 50 m apart were carried out to capture the sandy beach morphology at the beginning (5/Oct/2018) and end (26/Oct/2018) of the field experiment. All bathymetries were obtained through Real

Time Kinematic Global Navigation Satellite System (RTK-GNSS) surveyed from a boat. The upper and intertidal beach topography were surveyed using a Post Processing Kinematic Differential Global Navigation Satellite System (PPK-GNSS) carried in by walk on 15 and 22 October 2018. In addition, a high-resolution topographic survey employing photogrammetry (Laporte-Fauret et al., 2019) obtained by an UAV was performed at spring low tide on 24 October 2018 to measure the headland topography as well as the upper shore-face topography. The vertical uncertainty (95% CI) from bathymetric and topographic surveys is estimated to be less than 0.20 and 0.07 m, respectively (Mouragues et al., 2020b). These numerous surveys were combined and gridded using a natural neighbor interpolation approach that took cross-shore transect anisotropy into account. Figure 2.7 shows a comprehensive bathy-topo map relative to NGF-IGN69 leveling resulted from combination of bathymetric (26 June and 5 October 2018), topographic (15 October 2018) and UAV-derived topographic surveys. The submerged reef's maximum elevation is around -2.9 m (NGF-IGN69), corresponding to -2.5 m relative to the mean sea level. Figure 2.7b,e depicts the reef's significant influence on wave breaking patterns. It is worth noting that the connection between the beach and the headland is rather curved (see Figure 2.7a,d,e).

2.2.2 Hydrodynamic data

2.2.2.1 ADCP data

Four Acoustic Doppler Current Profilers (ADCPs) were installed at different locations across the field site to continuously measure and store pressure and velocity data along the water column in order to assess the natural variability of bathymetrically controlled circulation and headland rips. As described in Mouragues et al. (2020b), SIG1 (Nortek Signature 500 kHz; 4 Hz; cell size: 0.5 m), SIG2 (Nortek Signature 1000 kHz; 8 Hz; cell size 0.2 m), SIG3 (Nortek Signature 1000 kHz; 1 Hz; cell size: 0.2 m) and AQ (Nortek Aquadopp; 2 MHz; 1 Hz; cell size 0.1 m) were deployed far offshore (800 m offshore), few meters off the reef, along the headland and in the vicinity of the reef, respectively (see Figure 2.7). For convenience, velocities components were transformed to a cross-shore/alongshore local coordinate system by rotating 60° (counter-clockwise

direction) the North-East velocity coordinate system (Figure 2.9) using the following equations (Sous et al., 2020):

$$\begin{aligned} u &= u_E \cos(\theta) + u_N \sin(\theta) \\ v &= -u_E \sin(\theta) + u_N \sin(\theta). \end{aligned} \tag{2.1}$$

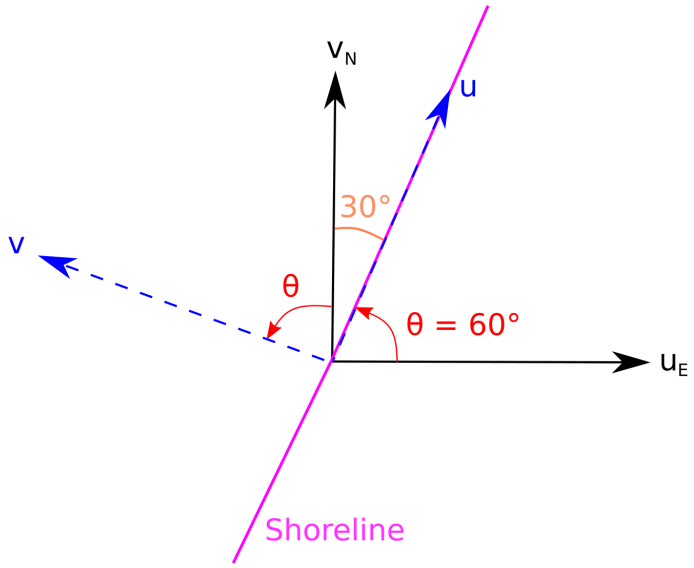

Figure 2.9 – Velocity frame rotation. The black arrows indicate the original North (v_N)/ East (u_E) velocity reference frame while the blue arrows indicate the cross-shore (v)/ alongshore (u) velocity local coordinate system after rotation. Anglet shoreline is indicated in magenta color and is oriented 30° with respect to the True North.

It is worth to note that only the Aquadopp current profiler (Figure 2.10a) is considered throughout this study since it is the only ADCP deployed within the fixed-camera view field that can be used to validate the video remote sensing techniques (see Figure 2.7).

2.2.2.2 Drifter data

The drifter experiment was supported by the very experienced team of CMAR (Coastal Marine Applied Research, coastal consultancy at University of Plymouth) who provided six surf-zone drifters and help in the field during drifter deployment. The drifters were released multiple times near the reef to measure Lagrangian surface current velocities and capture a wider spatial extent of circulation variability than Eulerian measurements. Deployment methods varied from surfzone seeding by hand (swimming the drifter into

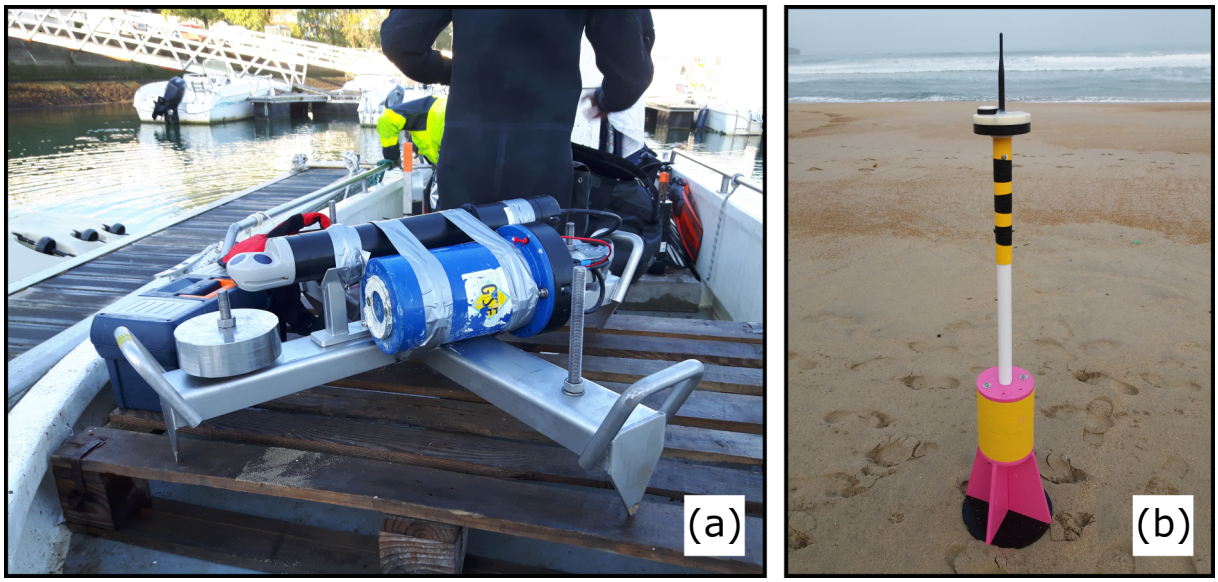

Figure 2.10 – (**a**) Aquadopp (AQ) current profiler and (**b**) one of the six surface drifters deployed during October 2018 field experiment.

position) and drifter seeding by jet ski. Drifters were based on the design of MacMahan et al. (2009) and consisted of a 110-cm long thin PVC pole with a GNSS antenna attached on top (Figure 2.10b). To minimize surfing behavior, the mast was coupled to a 40-cm long submerged PVC tube that served as ballast, with a dampening plate and exterior fins. This type of drifter design has been previously used to measure surface flows associated with rips (e.g., Austin et al. 2013; McCarroll et al. 2014; Scott et al. 2016). The drifter positions were telemetered in real time to a coastal ground station to facilitate deployment and retrieving logistics. QPS Qinsy hydrographic software was used to track drifter positions. Drifters' data collected at 2.5 Hz allowed studying surface current circulation patterns over the course of four days (18, 19, 22, and 23 October 2018). Individual deployment duration for each day ranged from 2 h to 3 h 30 min with spatial coverage ranging from 330 to 950 m relative to the shoreline position. According to Mouragues et al. (2020b), drifter position and velocity uncertainties are estimated to be less than 3 m and approximately 0.1 m/s, respectively. Furthermore, the error associated to the effect of wind slippage on drifter trajectory is below 0.04 m/s.

2.2.3 Video data

As shown in subsection 2.1.3 (Figure 2.6), high-frequency (1 Hz) sampled images recorded at 1624x1234 px were collected continuously during daylight hours for almost the entire three-week field experiment from a single video camera located inside Biarritz lighthouse (see Figure 2.8d; H-b Cam). Additional video monitoring was made using a camera-equipped UAV (e.g., Figure 2.7c).

2.2.4 Offshore wave, tide and wind conditions

During the field experiment, PCA beach was exposed to incident wave conditions characterized by long-period moderate- to high-energy wave events. Offshore significant wave height H_s ranged from 0.4 to 4.2 m, with a mean of 1.5 m (Figure 2.8a), while offshore peak wave period T_p and mean wave period T_{m02} ranged from 6 to 16 s and from 5 to 11 s, respectively (Figure 2.8b).

Wave conditions were also characterized by a wide range of wave incident obliquity, from shore-normal to very oblique waves (Figure 2.8c). The peak wave incidence (angle of wave incidence relative to the shore normal) θ_p ranged from -23 to 27°. The sign of θ_p is set depending on which side of the headland waves are coming from (Figure 2.8a). While $\theta_p = 0°$ indicates shore-normal waves (hereafter called shore-normal configuration), $\theta_p < 0°$ and $\theta_p > 0°$ mean that the headland is located at the updrift (hereafter called shadowed configuration) or downdrift (hereafter called deflection configuration) side of the embayment, respectively. Overall, the first and third weeks of measurements correspond to deflection configuration, while the second week was mostly shadowed configuration.

Hourly wind data was retrieved from the Biarritz airport meteorological station (71 m altitude) located approximately 3 km SW of the study site (Figure 2.1). wind conditions were relatively weak during the field experiment, with mean wind speed around 3 m/s coming primarily from the S-SE sector, reaching wind speed up to 12 m/s coming from the W-NW (roughly shore normal) direction. In addition to the offshore wave condition variability, the experiment was characterized by different tidal level with tidal range varying from 4.4 m during spring tides to 1.1 m during neap tides (Figure 2.8a).

Chapter 3

Image stabilization

Contents

3.1 Preamble

This chapter is based on the research article Rodriguez-Padilla et al. (2020) published in the Journal of *Remote Sensing*, available in open access: https://www.mdpi.com/602702

The motivation for this work arose in response to the need to overcome a quite common issue that is typically overlooked in most studies involving video-derived data,

remote sensing

MDPI

Article

A Simple and Efficient Image Stabilization Method for Coastal Monitoring Video Systems

Isaac Rodriguez-Padilla [1,*], Bruno Castelle [1], Vincent Marieu [1] and Denis Morichon [2]

[1] CNRS, UMR 5805 EPOC, Université de Bordeaux, 33615 Pessac, France; bruno.castelle@u-bordeaux.fr (B.C.); vincent.marieu@u-bordeaux.fr (V.M.)

[2] SIAME-E2S, Université de Pau et des Pays de l'Adour, 64600 Anglet, France; denis.morichon@univ-pau.fr

* Correspondence: isaac.rodriguez-padilla.1@u-bordeaux.fr

Received: 21 November 2019; Accepted: 21 December 2019; Published: 24 December 2019

which is concerned to unwanted camera movement. In the case of this study, during the early stage of image processing we realized that the images did not remain static over time, implying camera movement. Preliminary results obtained using this set of shifted images showed large errors associated to even slightly camera viewing angle deviation resulting in questionable and unreliable video-derived products. It is important to note that camera movement was sort of unexpected since the fixed-mounted cameras were located inside the lighthouse sheltered from the external elements (e.g., wind or rain) which would lead to the assumption that there should not be any factor that could alter its position. Nevertheless, thermal expansion was the responsible for this particular type of camera motion which evidently was an issue difficult to avoid or prevent. An alarming founding was that image-shifting was present and spread on a wide range of timescales over the total 5-year long image time series representing a major source of error for further video analysis. Thus, it was imperative to devote some time to investigate the impact of camera viewing angle deviation and find an approach to reorient (i.e., stabilize) each of the shifted images in order to guarantee an optimal accuracy.

This chapter summarizes an approach to correct/stabilize a low-sampled (daily) image sequence, as there was no straightforward image stabilization method available that worked under large variations of brightness between frames. The developed approach consists of quantifying the displacement in the image plane (induced by camera movement) by tracking fixed recognizable feature points and further using them to warp the image with respect to a reference position. What makes this method really unique from

other existing stabilization methods is the implementation of a Canny filter (Canny, 1986) which adds robustness to track features under varying brightness and contrast conditions making it suitable for large databases processing. This method is generic (pending fixed salient points) and has also been tested using UAV imagery proving to be useful against undesirable flight movements such as repositioning or high-frequency vibrations. Therefore, the present stabilization method opens new perspectives to routinely improve camera geometry of video monitoring systems to further derive higher quality remotely sensed hydrodynamic and morphological products.

3.2 Introduction

The use of shore-based video systems has become a very popular and accessible low-cost tool for coastal monitoring given their capability to deliver continuous and high-resolution temporal data over large enough spatial scales. However, the reliability of the final image products can be compromised by external factors, sometimes overlooked, that can alter the image geometry over time. In particular, unwanted camera movement, produced either by thermal or mechanical effects, can lead to significant geo-rectification errors if not properly corrected. Several studies (Bouvier et al., 2019; Holman and Stanley, 2007; Pearre and Puleo, 2009; Vousdoukas et al., 2011a,b) have acknowledged the presence of camera motion and have proposed different post-processing procedures, often referred to as image stabilization methods, to compensate for camera movement. This chapter addresses an alternative straightforward method to stabilize an either continuous or subsampled image sequence based on state-of-the-art techniques and available routines. This method can also be applied to remove high-frequency camera movements obtained when using unmanned aerial vehicles (UAVs) for monitoring purpose. Image stabilization is a fundamental post-processing step that should always be performed in general coastal imaging applications to increase the accuracy of video-derived products, such as shoreline/sandbar position and depths estimate.

3.3 Article: A Simple and Efficient Image Stabilization Method for Coastal Video Monitoring Video Systems

3.3.1 Abstract

Fixed video camera systems are consistently prone to importune motions over time due to either thermal effects or mechanical factors. These, even subtle, displacements are mostly overlooked or ignored, although they can lead to large geo-rectification errors. This paper describes a simple and efficient method to stabilize an either continuous or sub-sampled image sequence based on feature-matching and sub-pixel cross-correlation techniques. The method requires the presence and identification of different land-sub-image regions containing static recognizable features referred to as keypoints, such as corners or salient points. A Canny edge detector (CED) is used to locate and extract the boundaries of the features. Keypoints are matched against themselves after computing their two-dimensional displacement with respect to a reference frame. Pairs of keypoints are subsequently used as control points to fit a geometric transformation in order to align the whole frame with the reference image. The stabilization method is applied to 5 years of daily images collected from a three-camera permanent video system located at Anglet Beach, southwest France. Azimuth, tilt and roll deviations are computed for each camera. The three cameras showed motions on a wide range of time scales, with a prominent annual signal in azimuth and tilt deviation. Camera movement amplitude reached up to 10 pixels in azimuth, 30 pixels in tilt and 0.4° in roll, together with a quasi-steady counter-clockwise trend over the 5-year time series. Moreover, camera viewing angle deviations were found to induce large rectification errors of up to 400 m at a distance of 2.5 km from the camera. The mean shoreline apparent position was also affected by an approximately 10-20 m bias during the 2013/2014 outstanding winter period. The stabilization semi-automatic method successfully corrects camera geometry for fixed video monitoring systems and is able to process at least 90% of the frames without user assistance. The use of the CED greatly improves the performance of the cross-correlation algorithm by making it more robust against contrast and brightness variations between frames. The method appears as a promising tool for other

coastal imaging applications such as removal of undesired high-frequency movements of cameras equipping unmanned aerial vehicles (UAVs).

3.3.2 Introduction

Over the past decades, the use of shore-based video systems has become a very popular and accessible low-cost tool for coastal monitoring given their capability to deliver continuous, high-frequency (e.g., daily) data over large enough spatial scales (Holman and Stanley, 2007; Splinter et al., 2018b). Among the many applications using video-based remote sensing are shoreline and sandbar position tracking (van Enckevort et al., 2004; Coco et al., 2005; Huguet et al., 2016), nearshore bathymetry estimation (Stockdon and Holman, 2000; van Dongeren et al., 2008; Holman et al., 2013), determination of intertidal beach slope (Aarninkhof and Roelvink, 1999; Madsen and Plant, 2001), rip channel formation and evolution, (Bogle et al., 2001; Holman et al., 2006; Turner et al., 2007; Quartel, 2009), estimation of longshore currents (Chickadel et al., 2003; Almar et al., 2016), wave celerity, period and direction (Lippmann and Holman, 1991; Holland and Holman, 1999; Stockdon and Holman, 2000), as well as breaking wave height (Almar et al., 2012a).

Nevertheless, successful and reliable video-based products can only be produced if accurate image transformation into real-world coordinates is achieved. This is performed through photogrammetry techniques which provides relationship between the 2-D image geometry and the 3-D real-world coordinates. A common approach consists in using projective transformation (Holland et al., 1997; Hartley and Zisserman, 2004) that usually takes into account two types of calibration: an intrinsic calibration, which accounts for the physical characteristics of the camera lens and can be obtained directly in the lab prior to field installation (in order to remove distortion effects); and an extrinsic calibration, which depends on the camera location and orientation after installation, as well as a set of surveyed ground control points (GCPs), correspondingly manually digitized from the image. Both calibrations are often done just once assuming that the physical properties of the lens remain unchanged over time and that the video cameras and their mounting structure do not move. Hence, the real-world coordinates of the fixed GCPs are supposed to systematically coincide with the digitized GCPs image

coordinates for all video frames. However, the latter assumption is challenged by many observations showing that even fixed-mounted video cameras are never perfectly static (Holman and Stanley, 2007; Pearre and Puleo, 2009; Vousdoukas et al., 2011b; Bouvier et al., 2019).

Common non-anthropogenic causes that may produce camera movement or vibration are attributed to thermal expansion and insulation effects as well as rain and wind forcing (Holman and Stanley, 2007; Bouvier et al., 2019). This is particularly evident in outdoor installations where cameras are directly exposed to the elements. One possible but tedious solution to address this issue is to digitize all the GCPs for each presumably displaced image in order to obtain separately geometric solutions (Bouvier et al., 2019). Another potentially more efficient alternative is to use (semi-)automatic image stabilization.

Image stabilization refers to any technique used to create a video sequence in which any unwanted camera motion is removed from the original sequence. In coastal imagery, Holman and Stanley (2007) were the first to address the problem of camera viewing angle variations due to thermal and wind effects. In order to compensate the camera movement after acquisition, they used a template matching method that consisted in selecting small high-contrast regions of an image (including fixed objects and salient points) and match them with a reference image (from a survey date with a known geometry solution) to compute their displacement (deviations of tilt and azimuth) in terms of pixel shift. Using this technique they found an almost daily diurnal signal with an amplitude of approximately 2 pixels in tilt as a result of thermal response of the tower on which the cameras were mounted. After geo-rectification, this shift was equivalent to an error of approximately 30 m in the longshore direction 1000 m away from the camera. With the further increased use of Unmanned Aerial Vehicles (UAVs) such method has been refined and automatized to create and recognize features (virtual GCP's) within a user specified window and a brightness intensity threshold (Holman et al., 2017; Bergsma et al., 2019).

Similar automated feature matching image stabilization methods have been developed using the same principle of image comparison. Pearre and Puleo (2009) used correlation techniques, a procedure similar to particle image velocimetry (PIV; (Adrian,

1991)) to correct camera azimuthal and tilt movement. They showed that geo-rectified image errors owing to camera movement grows nonlinearly with the distance between the camera and the object of interest. Therefore, even small pixel variations can lead to large errors in real-world coordinates (500 m error 2300 m away from the camera at Rehoboth Beach, Delaware; (Pearre and Puleo, 2009)). Moreover, they found that despite all the cameras experienced slight movements, the motion effect after geo-rectification was more evident on the camera with the longest focal length as this camera was more sensitive to small changes in tilt. Another semi-automatic image stabilization procedure is described by Vousdoukas et al. (2011a,b) for UAVs and fixed cameras. Their method consists first in defining a mask to remove the sea from the land for all frames. The next step is to extract and match pairs of features (keypoints) between consecutive frames. This can be done either using a Scale-Invariant Feature Transform (SIFT; (Lowe, 1999, 2004)) or a Speeded-Up Robust Features (SURF) algorithm (Bay et al., 2008). Both algorithms are capable to detect and extract distinctive features such as corners and salient points, under some variations of illumination, scale, and orientation between frames. In order to identify the correct matches, a random sample consensus (RANSAC) algorithm (Fischler and Bolles, 1981) is implemented to filter the outliers, followed by a least squares fit approach, as well as a sub-sampling of keypoints pairs to reduce computation time.

All the above techniques rely upon the presence of land-based features or any fixed region that includes objects with high contrast in the camera field of view. However, in some cases, cameras just look at the ocean covering only a small beach portion offering little of no fixed salient features. Some studies have overcome this limitation by tracking the horizon and using it as a geometric constraint in order to estimate the camera position and stabilize the images (Schwendeman and Thomson, 2015; Sánchez-García et al., 2017). On the other hand, anticipating or predicting the movement of a camera can also be considered as an alternative approximation to reduce image deviation after acquisition when no features are available in the camera view field. Bouvier et al. (2019) identified the primary environmental parameters controlling cameras shift (air temperature, wind conditions, nebulosity and solar position) and used them to develop an empirical model to simulate camera movement. Their model showed a good agree-

ment against the observed camera viewing angles deviations (r^2 = 0.71, $RMSE$ = 0.12° for tilt and roll anomaly) confirming that, at their site, camera motion is primarily controlled by thermal expansion of the pole where the cameras were mounted, which is modulated in magnitude by the solar azimuth angle and cloud coverage. Bouvier et al. (2019) indicated that the rectification error is up to 200 m and 20 m in the long-shore and cross-shore direction, respectively, which can be decreased by 80% with their automated stabilization method.

Image stabilization is a fundamental topic in the research field of Computer Vision (Szeliski, 2010) with many applications in object recognition (Torii et al., 2011), motion analysis (Rawat and Singhai, 2011), image restoration (Wang and Tao, 2016), among others (Chalom et al., 2013). Similar stabilization methods have been developed with other purposes outside the field of coastal imagery (Hsieh and Kao, 2010; Chang Li and Yangke Liu, 2011; Kulkarni et al., 2017; Souza and Pedrini, 2018). One primary problem with existing stabilization methods is that they are sensitive to changes in illumination making them prone to failure (El-gayar et al., 2013). Brightness and contrast variations due to illumination changes are typical for image sequences and can often change within a few frames (Matas et al., 2003). Moreover, if the image sequence is sub-sampled, these parameters can substantially change between consecutive frames. The purpose of the present work is to develop a new straightforward method for image stabilization to overcome this limitation. This method provides a robust solution to stabilize an image sequence under varying illumination with the ability to process large databases. It builds on state-of-the-art techniques and available routines, with valuable input for the coastal imaging research community. The following sections will describe the basic steps to stabilize an image sequence compensating for camera motion to avoid positioning errors in the image. Furthermore, the image stabilization method will be applied to 5 years of continuous video data collected from a three-camera video system located at Anglet Beach, southwest France.

3.3.3 Study site and video data

Anglet Beach is a structurally-engineered embayed sandy beach located on the Basque Coast in southwest France (Figure 3.1). The beach is delimited by a prominent head-

land in the South and extends over 4 km up to a 1 km long jetty protecting the entrance of the river mouth. According to Wright and Short (1984) classification, Anglet Beach is an intermediate-reflective beach composed of medium to coarse sand with a steep beach-face slope ($\tan\beta \approx 0.1$) characterized by a mostly double bar system (Birrien et al., 2013; Huguet et al., 2016). Given the WNW beach orientation, the coast is predominantly exposed to North Atlantic high-energy swells coming from the WNW direction with an average annual significant offshore wave height $H_s = 1.57$ m (occasional wave heights > 10 m during winter storms) and average peak period $T_p = 10$ s (Enjalbert et al., 2011; Birrien et al., 2013). Tides in the area are semi-diurnal with average ranges of 3.94 m for spring tides and 1.69 m for neap tides (i.e., meso-macro tidal range).

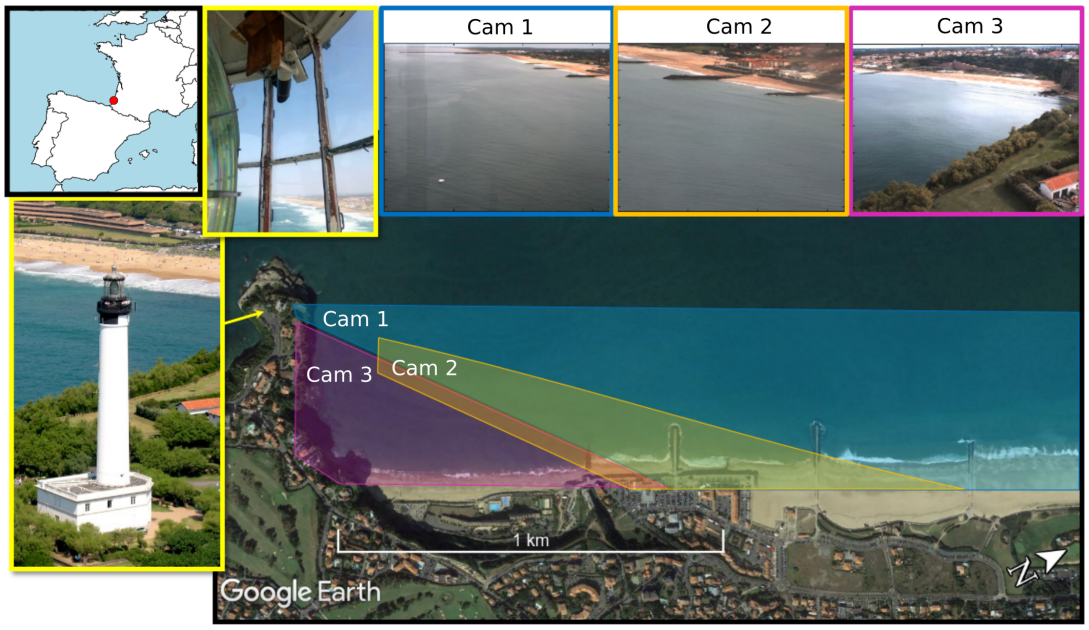

Figure 3.1 – Map of Anglet Beach (Basque Coast, southwest France) showing the location and field of view of the three-camera video system installed inside the Biarritz lighthouse (photo by M. Bourbon).

A permanent video-monitoring station has been operating since September 2013 at the southern end of Anglet Beach. It is installed inside the Biarritz lighthouse, 70 m above mean sea level. The station consists of three cameras: camera 1 (12 mm lens), camera 2 (25 mm lens) and camera 3 (8 mm lens) that together cover approximately 2.5 km of the southern beach shoreline, including 4 groins that extend about 100 m seaward (Figure 3.1). Each camera provides different image products during daylight.

From September 2013 to February 2017, single snapshot images, 10-min averaged time-exposure images (timex), 10-min variance images and 10-min timestack images (e.g., Holman and Stanley, 2007) were collected every 20 min at 1 Hz. In March 2017, the configuration of the video-station changed. Since April 2017 to the present, image products are collected every 15 min at 1 Hz during an averaged period of sampling of 14-min. According to Castelle et al. (2014b), the best shoreline proxy for meso-macrotidal multiple-barred beaches is obtained at mean high water level (MHW), since the inner-bar and berm dynamics have little influence on the shoreline cross-shore displacement for this elevation contour. In order to have at least one image per day, the lowest high tide level was preferred. For this study, time-exposure images were selected at mean high water neap level time (MHWN = 0.86 m) with a mean accuracy of $\pm$ 0.08 m and a maximum error of $\pm$ 0.28 m. This resulted in a 5-year daily time-exposure image time series consisting of approximately 1500 frames per camera spanning from October 1, 2013 to September 9, 2018. The timex time series will be treated as a continuous image sequence and will be further used to compute the long-term image displacement for each camera.

3.3.4 Image stabilization method

The image stabilization method developed below is based on feature matching and necessarily requires the presence of at least a few recognizable static features distributed in both dimensions in the field of view. Features should not be collinear so that the geometric transformation can be correctly applied to the whole image. The concept of the method is to compute the two-dimensional displacement (azimuth and tilt) of the features between frames and use them as matching control points to estimate a 2-D geometric transformation that incorporates translation, rotation and scaling to align the whole image with a reference image. The following subsections will describe the basic steps to stabilize an image sequence through a semi-automatic procedure using state-of-the-art techniques.

3.3.4.1 Reference image and sub-image regions selection

The first step consists of defining a reference image. All the frame motions will be estimated relative to this reference image. The selection of the reference image should correspond to the time when the GCPs were surveyed. The next step is to identify static recognizable features within the reference frame. The features should be easily visible fixed objects such as buildings or any inland hard structure containing corners or salient points. The features should not only appear in the reference image, but also in every frame of the whole time series. Around each feature, a sub-image region (hereinafter referred to as zone) should be manually defined. This user-defined zone surrounding the feature must also contain a single reference point, referred to as keypoint, specified by the user. Every zone will act as a search region to identify the keypoint, representing the feature, that will be drifting with time. This implies that the user needs to estimate a possible range of camera pixel shift to design the zone within which the feature and keypoint is always visible. This can be done easily through a visual inspection of the entire image sequence. To test if the zone size is adequate, the zone from the reference frame can be compared with the last frame of the image sequence (assuming that the last frame is shifted) or any other random frame to verify if the zone still isolates the feature containing the keypoint. It must also bear in mind that the user must design a not too large zone to keep computation time reasonable since every zone is treated as an individual sub-image sequence. The number of keypoints depends on the geometric transformation that will further be used (at least two keypoints are necessary; more is better) and should be distributed as much as possible throughout the reference image to avoid collinearity. The keypoint pixel positions will be defined as $(\kappa_u^{z,c}, \kappa_v^{z,c})$, where z is the sub-image zone index and c is the camera number index.

Figure 3.2 shows an example of the selection of four different sub-image zones for camera 2 of Anglet video station. The sizes of the zones vary but are kept to roughly 250×90 pixels. It is worth to mention that it is not advised to choose groins as keypoints since the corresponding zone will include non-stationary features from the water (such as foam patches) that can be mistakenly identified as keypoints and can introduce significant errors during the image stabilization method (Vousdoukas et al., 2011a). For the present study four zones were defined for camera 1 and 2, and five zones for camera

3. The reference image for each camera was defined as the first frame of each image sequence (Oct/01/2013 - 09:40:00 GMT).

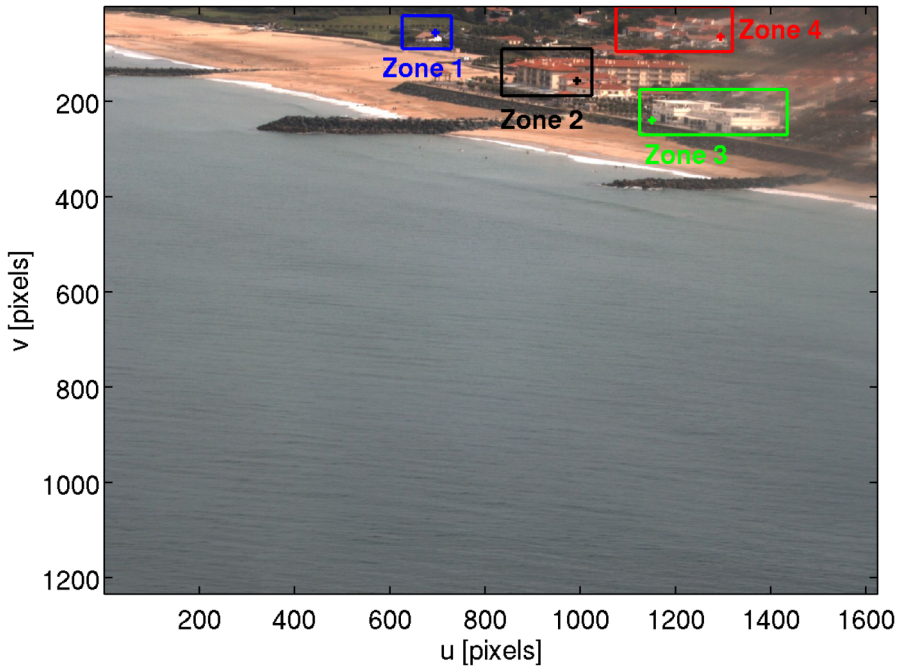

Figure 3.2 – Selection of different fixed land regions (zones) with their respective keypoints for camera 2.

3.3.4.2 Canny edge detector

Many popular algorithms automatically recognize, extract and match keypoints between frames without any a priori knowledge using corner and blob recognition under similar illumination conditions (Tareen and Saleem, 2018). Examples of widely used feature detection algorithms are: SIFT (Scale-Invariant Feature Transform; (Lowe, 1999, 2004)), FAST (Features from Accelerated Segment Test; (Rosten and Drummond, 2005)) and SURF (Speeded-Up Robust Features; (Bay et al., 2008)). Although these algorithms have proven to be very efficient in object recognition applications, their performance is only robust against small brightness changes between frames. This does not represent an inconvenience if the image sequence to stabilize is sampled at a high-frequency frame rate during a small period of time (e.g., UAV survey at 2 Hz during 17 min) since the contrast and brightness between frames barely change. However, in long-term coastal monitoring, it is common to work with sub-sampled image sequences (e.g.,

daily images as for this study) where consecutive frames usually change substantially in terms of brightness and contrast owing to different weather and daylight conditions leading the feature detector algorithms to degrade and fail.

The present stabilization method makes use of a Canny edge detector (CED; (Canny, 1986)) to enhance and extract the edges that define the boundaries of the primary features within a sub-image zone. Although the CED is not insensitive to changes in illumination, it is quite robust at recognizing the same edges between frames even under luminosity variations. The CED works in 5 steps: **a)** smooth the image using a Gaussian filter in order to remove the noise; **b)** determine the image intensity gradient in both vertical and horizontal directions; **c)** apply a non-maximum suppression to discard all the points that do not occur at the gradient local maximum; **d)** apply double threshold to preserve certain edges and **e)** track and keep weak edges that are connected to strong edges via an edge threshold (referred to as hysteresis).

3.3.4.3 Image sub-pixel cross-correlation and translation

Before registering and aligning images, a mathematical relationship should be established so that pixel coordinates can be mapped from one image to another. In this sense, a displaced image $g(u', v')$ can be expressed as a coordinate transformation (T) of a reference image $f(u, v)$. A 2-D affine transformation that considers only translation is valid to apply if the size, shape and orientation of the displaced image remain the same as that of the reference image. This mapping can be represented as a matrix multiplication $(\mathbf{g} = \mathbf{Tf})$ using homogeneous coordinates (Hartley and Zisserman, 2004):

$$\begin{bmatrix} u' \\ v' \\ 1 \end{bmatrix} = \begin{bmatrix} 1 & 0 & \Delta u \\ 0 & 1 & \Delta v \\ 0 & 0 & 1 \end{bmatrix} \begin{bmatrix} u \\ v \\ 1 \end{bmatrix} = \begin{bmatrix} u + \Delta u \\ v + \Delta v \\ 1 \end{bmatrix}, \tag{3.1}$$

where Δu and Δv denote the two-dimensional displacement (i.e., pixel shift) of $g(u', v')$ with respect to $f(u, v)$.

The 2-D pixel rigid translation $(\Delta u, \Delta v)$ is obtained using the optimized cross-correlation algorithm of Guizar-Sicairos et al. (2008a) (also referred to as single-step

discrete Fourier transform algorithm). This algorithm allows registering the image displacement within a user-specified fraction of a pixel. The algorithm starts by up-sampling two times the resolution of the image dimensions (M and N) and applying a discrete fast Fourier transform (DFT) over all image points (u, v) to get an initial estimate of the location of the cross-correlation peak. The cross-correlation (CC_{fg}) of $f(u, v)$ and $g(u', v')$ can be expressed as follows:

$$\begin{aligned} CC_{fg}(\Delta u, \Delta v) &= \sum_{u,v} f(u, v) g^*(u' - \Delta u, v' - \Delta v) \\ &= \sum_{m,n} F(m, n) G^*(m, n) \exp\left[i2\pi\left(\frac{m\Delta u}{M} + \frac{n\Delta v}{N}\right)\right], \end{aligned} \tag{3.2}$$

where $(*)$ denotes complex conjugation and uppercase letters represent the DFT of the images, as given by:

$$F(m, n) = \sum_{u,v} \frac{f(u, v)}{\sqrt{MN}} \exp\left[-i2\pi\left(\frac{mu}{M} + \frac{nv}{N}\right)\right]. \tag{3.3}$$

For a higher up-sampling factor, instead of computing all the up-sampled points of the array, only a small neighborhood around the initial peak estimate is up-sampled using a matrix-multiply discrete Fourier transform to refine the peak location. This dramatically reduces computation cost without losing accuracy. A detailed description of the algorithm is beyond the scope of the present contribution and can be found in (Guizar-Sicairos et al., 2007, 2008a). In addition, a MATLAB code version of the algorithm is freely available and can be found in the MATLAB MathWorks File Exchange (Guizar-Sicairos et al., 2008b).

Once Δu and Δv corresponding to the cross-correlation peak are found, the displaced image can be relocated to the reference image position through an inverse transformation by mapping the pixel coordinates back to the reference image ($\mathbf{f} = \mathbf{T}^{-1}\mathbf{g}$):

$$\begin{bmatrix} u \\ v \\ 1 \end{bmatrix} = \begin{bmatrix} 1 & 0 & -\Delta u \\ 0 & 1 & -\Delta v \\ 0 & 0 & 1 \end{bmatrix} \begin{bmatrix} u' \\ v' \\ 1 \end{bmatrix} = \begin{bmatrix} u' - \Delta u \\ v' - \Delta v \\ 1 \end{bmatrix}. \tag{3.4}$$

As the image shift has sub-pixel accuracy, pixel values at fractional coordinates need to be retrieved. This is achieved by interpolating the surrounding pixels onto the refer-

ence image grid in order to compute the new intensities.

2-D rigid image translation is properly valid only for a perpendicular oriented camera. For an oblique view, the 2-D pixel rigid translation between frames can be interpreted as projections of the camera movement in the azimuth and tilt direction ($\Delta u = \Delta Azimuth, \Delta v = \Delta Tilt$; (Holman and Stanley, 2007; Pearre and Puleo, 2009; Vousdoukas et al., 2011b)). Given the changes in perspective, the 2-D shifts between frames will also vary depending on the sub-region of the image. For the present method, 2-D shifts are computed only with the purpose to match keypoints distributed in different zones of the image. The stabilization of the whole image, on the other hand, will be performed using these keypoints with another type of geometric transformation with more degrees of freedom to account for the image deformation produced by the relative angle variation of the camera.

At this stage, the keypoints and their corresponding surrounding zones have been defined and filtered through the CED in order to extract the edges of the features and improve the performance of the cross-correlation algorithm. The next step consists to use these features along consecutive frames to estimate, via sub-pixel cross-correlation, the two-dimensional displacement of each zone and camera ($\Delta u^{z,c}_{j,r}, \Delta v^{z,c}_{j,r}$); where, j is the frame number index, and r is the reference frame used for the computation of the 2-D sub-pixel shift. Figure 3.3 shows an example of keypoint matching between a pair of sub-images from zone 1 ($z = 1$) of camera 2 ($c = 2$). First, the CED is applied to both sub-images: the reference sub-image ($r = 1$; Oct/01/2013 - 09:40:00 GMT) and the displaced sub-image ($j = 1301$; Feb/06/2018 - 09:15:00 GMT). The sub-pixel shift between frames is subsequently computed using an up-sampling factor of 20: $\Delta u^{1,2}_{1301,1} = -2$ pixels, $\Delta v^{1,2}_{1301,1} = -29.2$ pixels. Finally, the shift is used to translate the displaced sub-image to match with the keypoint of the reference sub-image represented by the green cross ($\kappa^{1,2}_u = \kappa^{1,2}_{u'} - \Delta u^{1,2}_{1301,1}, \kappa^{1,2}_v = \kappa^{1,2}_{v'} - \Delta v^{1,2}_{1301,1}$) in Figure 3.3.

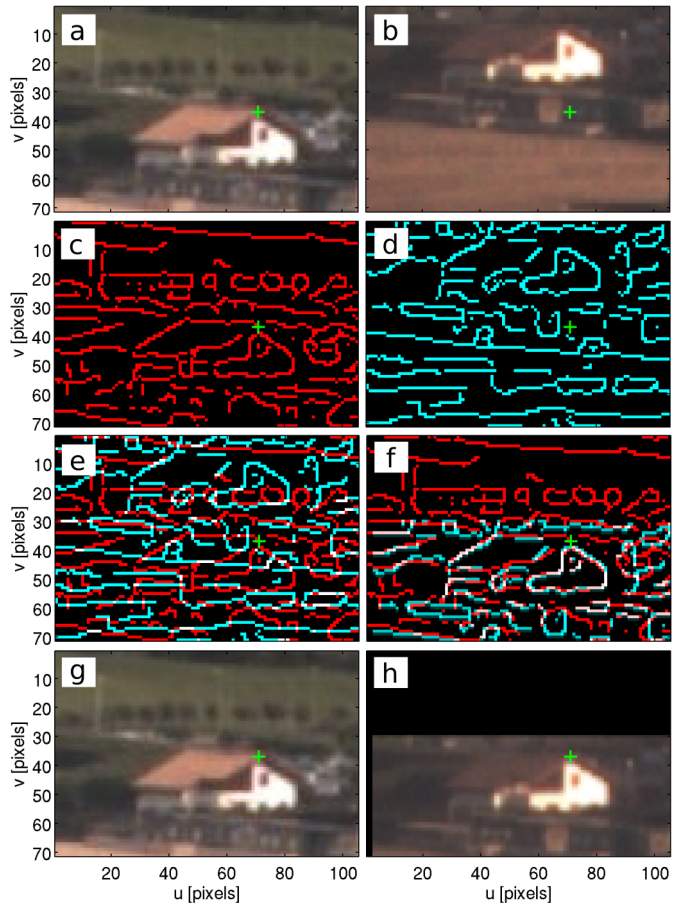

Figure 3.3 – Keypoint matching between a pair of sub-images corresponding to zone 1 of camera 2. (**a**) Reference sub-image: Oct/01/2013 - 09:40:00 GMT; (**b**) unstabilized sub-image: Feb/06/2018 - 09:15:00 GMT; (**c**) reference sub-image after applying the CED; (**d**) unstabilized sub-image after applying the CED; (**e**) reference and unstabilized sub-image overlapped; (**f**) sub-image translation after computing azimuth and tilt pixel shift; (**g**) same figure as (a); (**h**) stabilized sub-image: Feb/06/2018 - 09:15:00 GMT. The green cross represents the static keypoint that should match between frames.

A semi-automatic method is developed to perform the same steps as shown in Figure 3.3 for a given image sequence. Figure 3.4 illustrates a single iteration of this procedure. The goal is to compute the pixel shift of every frame with respect to the reference image ($\Delta u_{j,r}^{z,c}, \Delta v_{j,r}^{z,c}$) in order to retrieve the keypoints displaced positions ($\kappa_{u'_j}^{z,c}, \kappa_{v'_j}^{z,c}$). The routine works under a loop that iterates over all the frames of a given zone and camera. At each iteration, the algorithm automatically applies a CED to the sub-image zone and computes the pixel shift of the current frame with respect to the reference frame (case 1). An additional condition is used to assess the congruence of the estimated pixel shift. The condition assumes that the pixel shift between consecutive frames is small. A

typical diurnal signal due to thermal expansion is approximately 2-pixel range (Holman and Stanley, 2007), so even if the image sequence is sub-sampled it is reasonable to stipulate that the pixel shift of a frame with respect to the previous one should not be larger than 10 pixels, either in u or v directions. In the case that the condition is not fulfilled, there is no certain way to discern if the estimated pixel shift is anomalously large because the cross-correlation algorithm has been fooled or if the displacement is actually true and resulted from other factors (e.g., human intervention, strong wind, etc.). The CED plays a critical role in decreasing the effect of brightness and contrast changes between frames by just retrieving the edges, however, the cross-correlation algorithm is still likely to fail if some edge patterns of the same keypoint do not match, or even worst, if patterns resemble mistakenly while corresponding to different real-world patterns. To verify that the two frames are as similar as possible, a second option (case 2) is proposed to estimate $\Delta u_{j,r}^{z,c}$ and $\Delta v_{j,r}^{z,c}$ without directly computing the pixel shift with respect to the reference frame. Instead, the pixel shift is computed with respect to the previous stabilized frame: $f(u_{j-1}^{z,c}, v_{j-1}^{z,c}) = g(u'^{z,c}_{j-1} - \Delta u_{j-1,r}^{z,c}, v'^{z,c}_{j-1} - \Delta v_{j-1,r}^{z,c})$, which in turn is also relative to the reference frame. If despite the above two cases the pixel shift remains greater than 10 pixels, the algorithm enters in a semi-automatic mode and offers the user four different options:

- Keep the pixel shift computed by using the reference frame (case 1).
- Keep the pixel shift computed by using the previous stabilized frame as reference (case 2).
- Select manually the keypoint position to compute the pixel shift (case 3).
- Discard the frame (case 4).

An additional visual representation (similar to Figure 3.3) shows the user how the stabilized frame would look like if case 1 or case 2 pixel shift were used. If neither option is appropriate, the user has the possibility to select manually the keypoint position $(\kappa_{u'_j}^{z,c}, \kappa_{v'_j}^{z,c})$ in the current frame in order to compute the correspondent pixel shift (case 3). Alternatively, the frame can present serious contamination in the form of sun glint, raindrops or fog in which case the frame can be discarded (case 4). Finally, the pixel shift is stored at each iteration so that all the keypoints of a given zone and camera can be matched against themselves.

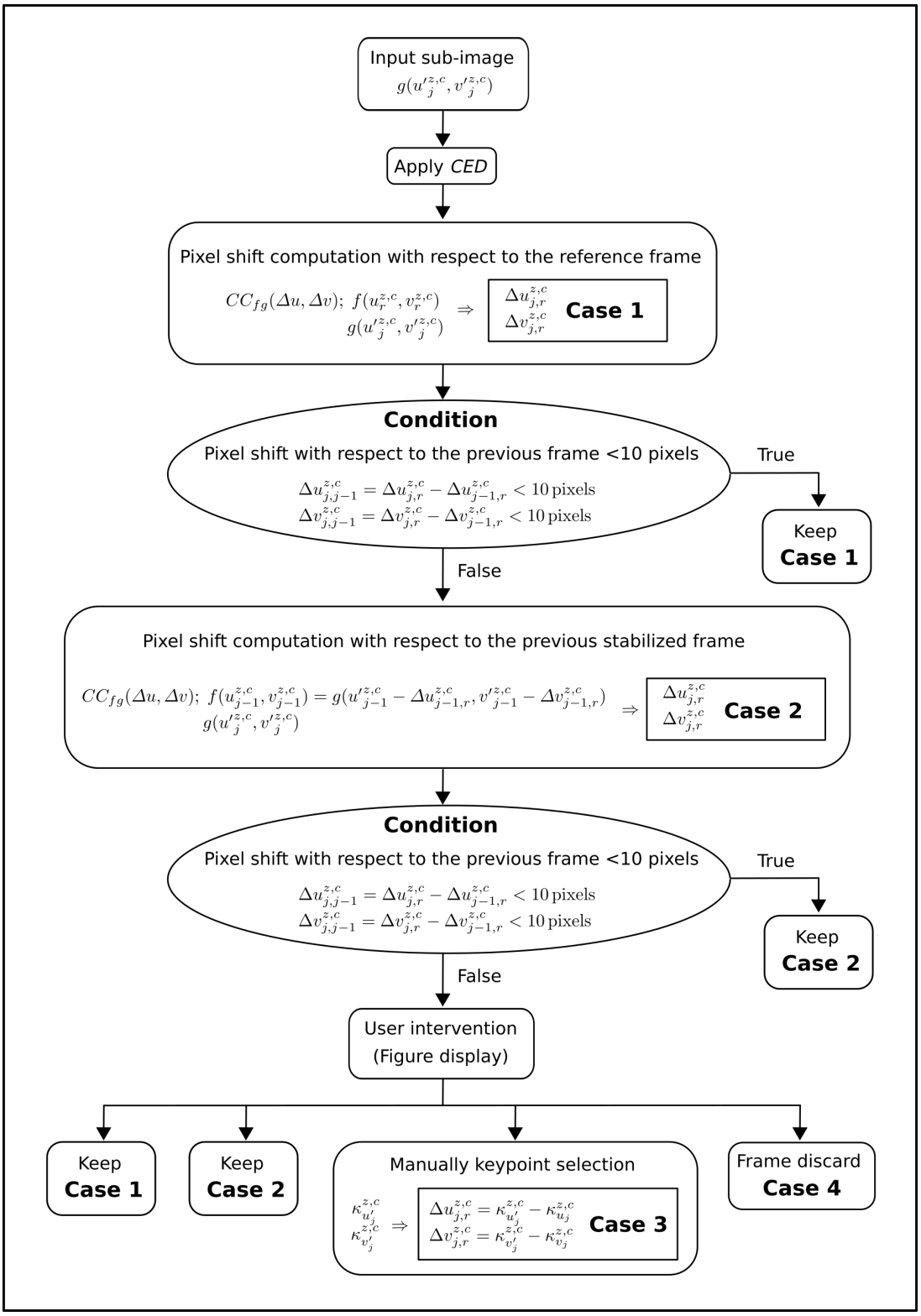

Figure 3.4 – Automatization steps to stabilize a sub-image zone of an image sequence by estimating the 2-D pixel shift with respect to a reference frame.

3.3.4.4 Geometric transformation

The number of corresponding keypoints identified between images establishes the type of geometric transformation that can be defined to map and relocate the displaced image points onto a reference image. A geometric transformation is constrained by the degrees of freedom (DOF). At least one corresponding keypoint is necessary to estimate the 2-D rigid translation motion between frames (2 DOF). Two pairs of non-collinear keypoints are enough to solve the four parameters of a similarity transformation:

$$\begin{bmatrix} u' \\ v' \\ 1 \end{bmatrix} = \begin{bmatrix} s\cos\theta & -s\sin\theta & \Delta u \\ s\sin\theta & s\cos\theta & \Delta v \\ 0 & 0 & 1 \end{bmatrix} \begin{bmatrix} u \\ v \\ 1 \end{bmatrix} = \begin{bmatrix} us\cos\theta - vs\sin\theta + \Delta u \\ us\sin\theta + vs\cos\theta + \Delta v \\ 1 \end{bmatrix}, \quad (3.5)$$

defined as a linear combination of translation ($\Delta u, \Delta v$), rotation (θ) and a scale factor (s). The rotation is defined as a counter-clockwise rotating angle with respect to the reference frame and can often be interpreted as the camera angle movement on its roll axis. The similarity transformation lacks the ability to represent a true three dimensional motion model, however, it can adequately estimate motion between frames if the camera movement or the scene are constrained to certain conditions (Ortiz Cayon, 2013). Jin et al. (2000) stated that if the translations of the camera are zero and the relative angle variation of the camera between frames is very small (e.g., less than 5°), the effect of the depth of scene points can be neglected. This means that camera roll is the main factor of image rotation ($\theta = \Delta Roll$) and small camera azimuth and tilt variations can be represented by 2-D translations of the image ($\Delta u = \Delta Azimuth, \Delta v = \Delta Tilt$). On the other hand, if image points are of the same depth, or the depth difference among image points is much less than the average depth (i.e., the camera is far away from the object), small camera translation will mainly cause homogeneous scaling and translation of 2-D images (Jin et al., 2001). The latter assumptions are valid for the case of fixed cameras as long as the viewing angles shift slightly. It is important to note that camera orientation always goes in the opposite direction from the relative frame displacements with respect to the reference image (Figure 3.5).

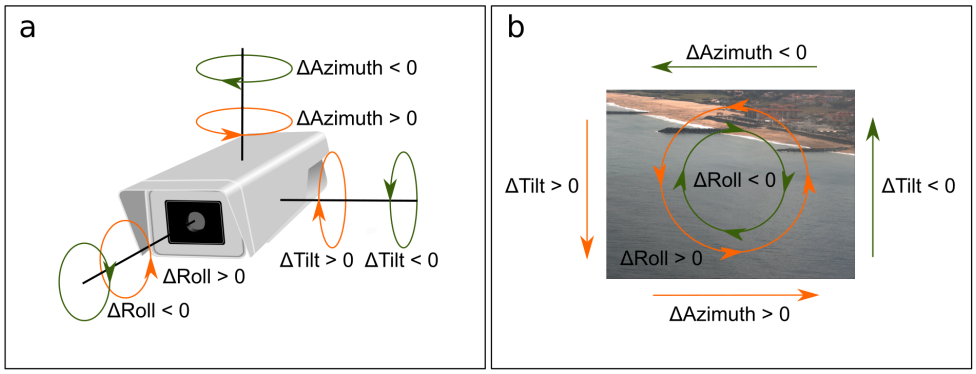

Figure 3.5 – (**a**) Camera angle movements according to (**b**) azimuth, tilt and roll deviations with respect to a reference image.

Working with a similarity transformation has the advantage to be fast and simple in terms of computational complexity (Lim et al., 2017). The similarity motion parameters can be estimated over an iterative process using the keypoints correspondences of all sub-images zones for every frame of a given camera. These parameters allow performing a global transformation to warp and stabilize the whole image sequence.

3.3.4.5 Image geo-rectification

After all the images are correctly stabilized, the coordinates of the 2-D images (u, v) must be transformed to 3-D real-world coordinates (x, y, z) through a photogrammetric transformation. The determination of the transformation is called camera calibration and involves two sets of parameters: extrinsic and intrinsic parameters. The extrinsic parameters contain the information related to the position and orientation of the camera (the three coordinates of the camera location and the three rotation angles) and the intrinsic parameters comprise the physical characteristics of the lens of the camera (the image center coordinates, the effective focal length and the scale factors). Direct linear transformation (DLT) developed by Abdel-Aziz and Karara (1971) is perhaps the most commonly used camera calibration method because it does not require initial knowledge of the extrinsic and intrinsic parameters (Sánchez-García et al., 2017). These parameters are implicit in the 11 transformation parameters, however, nonlinear effects such as radial distortion are not taken into account and can lead to coupling errors between parameters affecting the camera calibration accuracy (Zhao et al., 2016). DLT

method represents a closed form solution requiring non-coplanar real-world surveyed GCPs with corresponding image coordinates. Each GCP generates two linear equations that can be expressed as the following matrix multiplication:

$$\begin{pmatrix} x & y & z & 1 & 0 & 0 & 0 & 0 & -ux & -uy & -uz \\ 0 & 0 & 0 & 0 & x & y & z & 1 & -vx & -vy & -vz \end{pmatrix} L = \begin{pmatrix} u \\ v \end{pmatrix}, \tag{3.6}$$

where $L = (L_1, L_2, ..., L_{11})^T$ are the transformation parameters. At least six GCPs are necessary to build an overdetermined set of linear equations to estimate the 11 transformation parameters using a least square method. The limitation of working with one single camera, or many cameras that are not looking at the same object, is that one coordinate must be constrained to a fixed value to allow inverse mapping. When studying the nearshore zone, the vertical coordinate (z) is usually assigned to be equal to the instant sea level. However, if the topography is known and the swash zone is the subject of study (e.g., wave runup), an iterative rectification method using the beach topography can be applied to reduce rectification positioning errors as described by Blenkinsopp et al. (2016).

Another popular calibration method is the one proposed by Holland et al. (1997). In their method, they solve the five intrinsic parameters in lab and solve the six remaining extrinsic parameters using at least three GCPs and a standard nonlinear solver (Holman et al., 2017; Bergsma et al., 2019). The intrinsic parameters can be estimated using the Caltech camera calibration toolbox for Matlab (Bouguet, 2015) prior to camera installation in order to remove lens distortion. Although there are many well-documented camera calibration methods (Faig, 1975; Tsai, 1987; Clarke and Fryer, 1998; Wang et al., 2010), deciding which one to use is up to the user convenience.

For this particular paper, DLT was used to generate the plan-view (geo-rectified) images considering 8-10 GCPs per camera. Images were merged and projected into a horizontal plane with a grid size of 1×1 m and elevation equal to mean high water neaps (z_{MHWN} = 0.86 m). In addition, non-stabilized and stabilized geo-rectified images were compared to estimate the induced real-world positioning error due to camera movement.

3.3.5 Results

3.3.5.1 Keypoint tracking

The stabilization method was applied to 5 years of daily images collected from the permanent three-camera video system located at Anglet Beach. Figure 3.6 illustrates estimates of horizontal (azimuth) and vertical (tilt) displacements of the four keypoints distributed at different sub-image regions of camera 2 (see Figure 3.2). Azimuth and tilt deviations were expressed as pixel differences from the initial image position (Oct/01/2013 - 09:40:00 GMT). Results show a high variability in the position of the four keypoints indicating that the camera has been moving throughout the study period. Deviations of azimuth and tilt varied respectively from -10 pixels to 8 pixels and -33 pixels to 2 pixels. The standard deviation of the detrended pixel displacement, which is a measure of the magnitude of camera movements, was 2 and 5 pixels in the horizontal and vertical directions, respectively. The camera oblique view generated an approximately constant offset (0.2 pixels horizontal; 0.4 pixels vertical) in the displacement between zones. An annual motion signal (≈4 pixels amplitude) together with a quasi-steady trend (1.6 pixels/year horizontal; -3.4 pixels/year vertical) can be identified, suggesting that camera 2 orientation has been gradually moving towards the southwest direction.

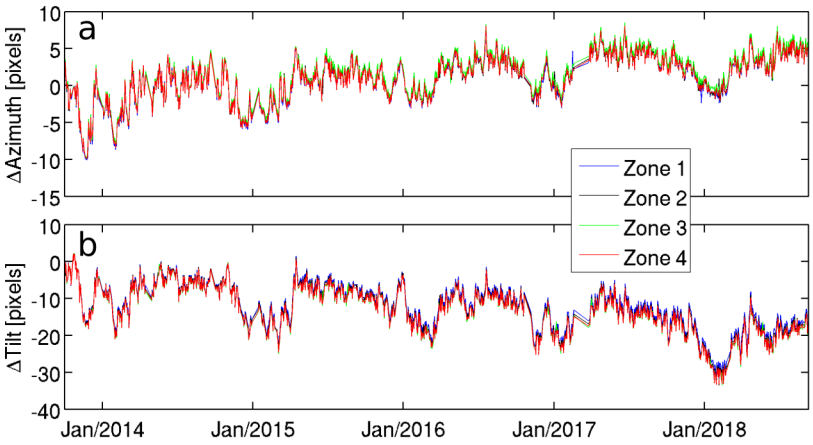

Figure 3.6 – Daily (**a**) azimuth and (**b**) tilt displacements of the different sub-image zones in cam 2 expressed in terms of pixel shift. The deviations are computed with respect to the reference image: Oct/01/2013 - 09:40:00 GMT.

3.3.5.2 Camera movement correction

Figure 3.7 shows the evolution of the transformation parameters (translation, rotation and scaling) derived from a Euclidean (a.k.a Similarity) transformation for the three-camera video system. All cameras showed motion throughout the study period on a wide range of time scales. Camera 1, 2 and 3 movement amplitude reached approximately 5.6 pixels, 10.4 pixels and 5.7 pixels in azimuth and 9.5 pixels, 30.7 pixels and 15.1 pixels in tilt, respectively. The standard deviation of detrended azimuth for the three cameras was 1.5 pixels, 2.5 pixels and 1.4 pixels with trends of -0.8 pixels/year, 1.6 pixels/year and -0.4 pixels/year. Respectively, the standard deviation of detrended tilt was 2.9 pixels, 4.7 pixels and 1.8 pixels with trends of 0.8 pixels/year, -2.9 pixels/year and -2.1 pixels/year. An annual signal of about 0.6 pixels (camera 1), 2.3 pixels (camera 2) and 0.4 pixels (camera 3) in azimuth and 1.9 pixels (camera 1), 4.2 pixels (camera 2) and 1.8 pixels (camera 3) in tilt deviation were apparent on the total record. Moreover, the three cameras presented variations in roll angle up to 0.4°, 0.2° and 0.1° with a standard deviation of 0.05°, 0.03° and 0.03° for camera 1, 2 and 3, respectively. Camera 1 and 2 exhibited an increasing counter-clockwise trend in roll angle (0.08°/year and 0.03°/year, respectively) over the 5-year time series. An overall enlargement was notable after 2015, particularly for camera 1. The scale factor (s) increased up to 10% the image size of camera 1 and 3% the image size of camera 2. Camera 3 presented no significant changes in image scale (maximum of 0.6%).

The transformation parameters were used to warp and align the whole image sequence with the reference frame. Figure 3.8 shows the long-term averaged video (spanning the complete time series) using raw video frames and corrected frames from camera 2. The raw input mean is blurry (Figure 3.8a) indicating significant image shifts induced by the camera movement. The mean of the corrected frames (Figure 3.8b) shows the efficacy of the stabilization method by preserving the same image sharpness (of the fixed features) as the reference frame.

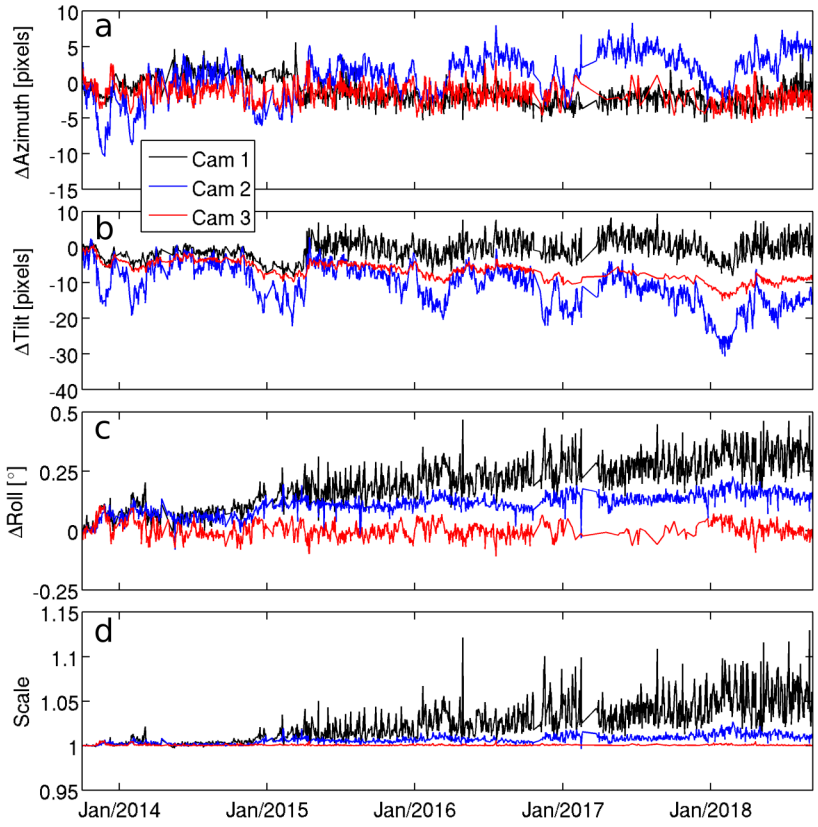

Figure 3.7 – (**a**) Azimuth, (**b**) tilt, (**c**) roll and (**d**) scale parameters of the similarity transformation matrix computed for the three cameras relative to the reference image: Oct/01/2013 - 09:40:00 GMT.

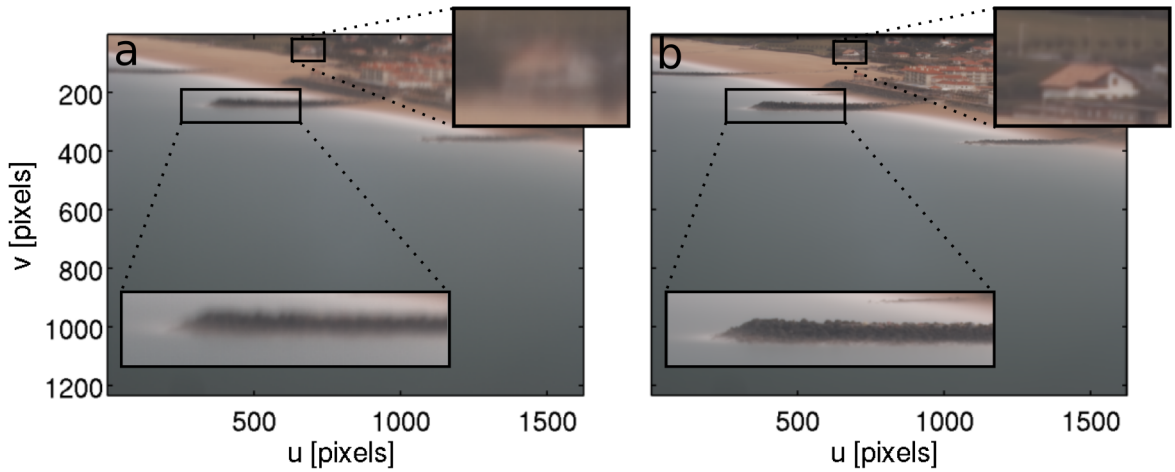

Figure 3.8 – Time series average (spanning Oct/01/2013 - Sep/09/2018) of all the (**a**) unstabilized frames and (**b**) stabilized frames of camera 2.

3.3.5.3 Geo-rectification error

Camera movements result not only in image deformation but also in geo-rectification errors. Figure 3.9 provides an example of positioning error due to camera motion. A comparison between stabilized and unstabilized geo-rectified images for a specific date is presented together with a spatial description of the error to highlight the impact of camera viewing angle deviations. Figure 3.9a shows the reference frame (Oct/01/2013 - 09:40:00 GMT) plain view image in real-world coordinates obtained after geo-rectification of the time-exposure images collected from the three-camera video system. Figure 3.9b,c show geo-rectification of a subsequent image when large camera viewing angle deviation was present (Feb/06/2018 - 09:15:00 GMT; same date chosen as for Figure 3.3). Figure 3.9b considers stabilization of the time-exposure images before geo-rectification, while Figure 3.9c does not take it into account. Figure 3.9d presents the associated geo-rectification error ($\sqrt{\text{alongshore error}^2 + \text{cross-shore error}^2}$) of Figure 3.9c produced by camera movement. This error depends on the grazing angle and lens properties and typically increases with increasing distance from the camera (Bouvier et al., 2019). The comparison between images highlights the differences in position, size and shape of fixed objects when stabilization is omitted. For this particular date, horizontal errors exceed 400 m (400 m in the alongshore and 100 m in the cross-shore direction). For instance, a displacement of the groins is readily apparent, with the alongshore location of the right-hand groin varying from 1750 m to 2000 m. Furthermore, the whole beach area appeared to shrink approximately 50 m in contrast to the stabilized geo-rectified image. The geo-rectified image that considered stabilization kept the groins well aligned with respect to their original position, with all the fixed objects retaining their initial size and shape.

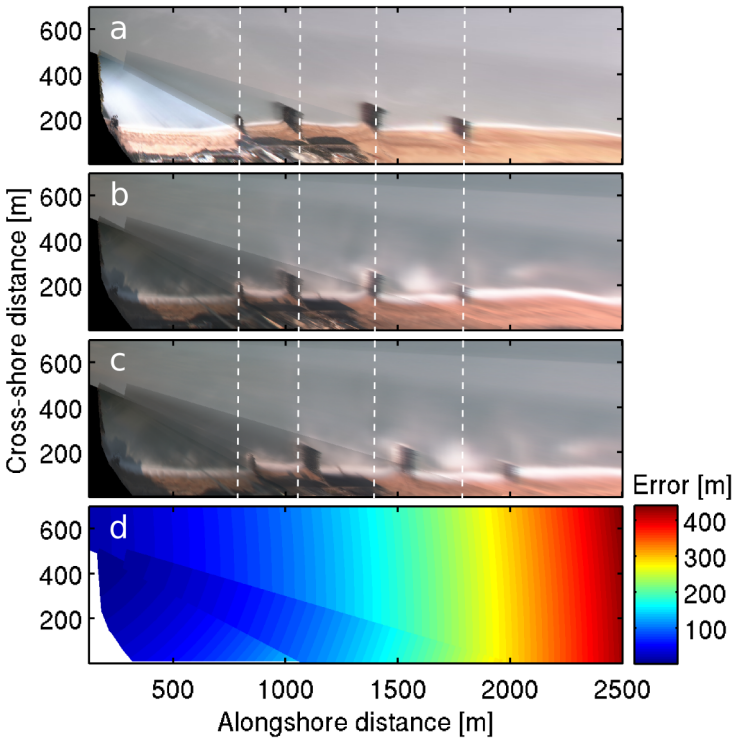

Figure 3.9 – Anglet Beach geo-rectified time-exposure images highlighting the impact of camera viewing angle deviation. (**a**) Reference geo-rectified image: Oct/01/2013 - 09:40:00 GMT; (**b**) stabilized geo-rectified image: Feb/06/2018 - 09:15:00 GMT; (**c**) unstabilized geo-rectified image: Feb/06/2018 - 09:15:00 GMT; (**d**) positioning error due to camera movement for Feb/06/2018 - 09:15:00 GMT. White dashed lines indicate groins original position.

3.3.6 Discussion

The semi-automatic stabilization method was applied to 5 years of daily time-exposure images collected from three synchronized cameras located at Anglet Beach, southwest France. For keypoint matching, approximately 1500 frames were processed for each sub-image zone requiring an average processing time between 1 s and 4 s per frame on a standard commercial personal computer (4^{th} generation Core i5-4690, 3.5 GHz). The distribution of cases used to compute the 2-D pixel shift displacement for each keypoint (Figure 3.4) gives an estimation of the performance of the algorithm in terms of how much user assistance was required. For example, just for sub-image zone 1 of camera 2, 97% of the pixel shifts were computed using case 1, 0.92% were computed using case 2, 0.26% using case 3 and 1.7% using case 4. This means that four frames,

corresponding to that zone, required manually pixel shift computation and 26 frames were manually discarded. The overall distribution of cases used for all cameras and all sub-image zones was: 90.42% (case 1), 1.38% (case 2), 4.91% (case 3) and 3.28% (case 4). It is important to note that some matching cases corresponding to case 1 and case 2 also required user visual control. User confirmation for those cases was necessary when the automatically computed pixel shift between consecutive frames was larger than the threshold (10 pixels) but still correct. Much of the user intervention essentially consisted of discarding low-quality frames. For future work, a possible improvement could be achieved by pre-selecting frames or explore this issue further by developing a separate procedure to automatically keep/discard frames prior to image stabilization.

The use of the CED is crucial for a robust performance of the cross-correlation algorithm when differences in contrast, brightness and illumination conditions between frames are present. Figure 3.10 shows the effect of the CED on the stabilization with respect to a reference sub-image (Figure 3.10a,e,i) under three representative cases of illumination conditions: under shinny (overexposed image; Figure 3.10b), cloudy (high-contrast image; Figure 3.10f) and foggy (low-contrast image; Figure 3.10j) weather conditions. The cross-correlation between sub-images without CED determines the similarity between frames based on their color/grayscale pixel intensity. This means that the performance of the cross-correlation not only depends on the features present in the frame, but also on changes in light conditions between frames. Large changes can lead to errors as shown in Figure 3.10c,g,k. On the other hand, when using the CED, pixels intensities are converted to only two possible values: 1 if edges that define the boundaries of the features are detected and 0 if not. The efficiency of the cross-correlation in combination with the CED relies upon the fact that the amount of data to be processed is reduced. Moreover, the cross-correlation algorithm together with the CED estimates the similarity between frames based only on the boundaries and edges detected, regardless of contrast and brightness variations between frames, as long as the features are still visible and easily recognizable by their shape and form (Figure 3.10d,h,l).

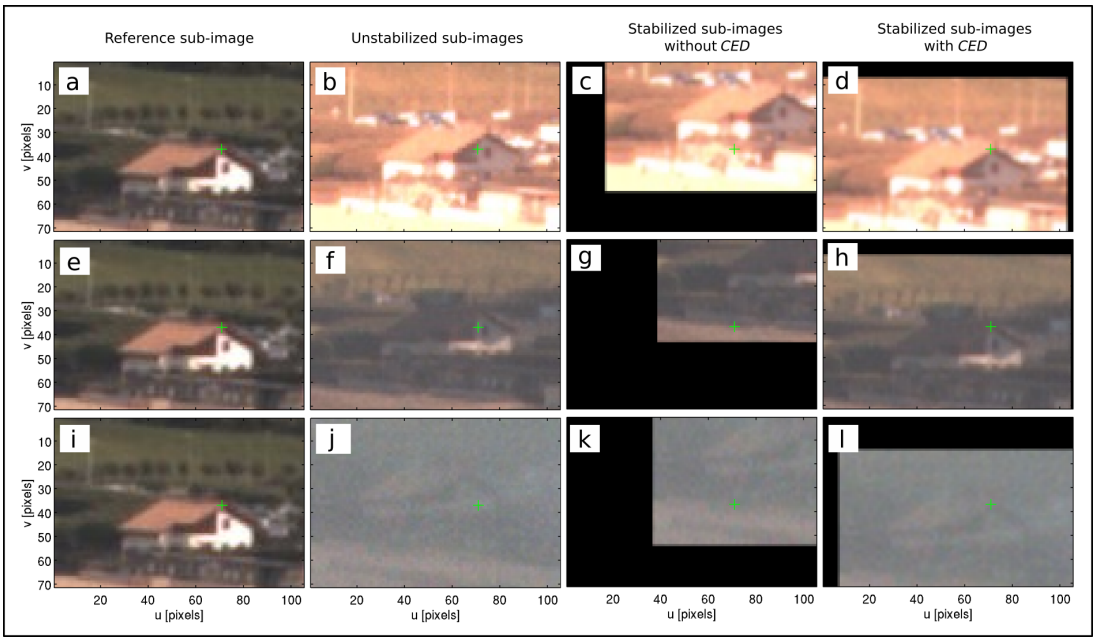

Figure 3.10 – Sub-image stabilization of zone 1 of camera 2 under different illumination conditions. (**a,e,i**) Reference sub-image: Oct/01/2013 - 09:40:00 GMT; (**b,f,j**) unstabilized sub-images under shinny, cloudy and foggy weather conditions; cross-correlation between the reference sub-image and the unstabilized sub-images with (**d,h,l**) and without (**c,g,k**) using the CED. The green cross represents the static keypoint that should match between frames.

The performance of the cross-correlation algorithm (together with the CED) depends strongly on the land-region zone selected, therefore the sub-image region selection is the most important step of the method. It is advised to define a large enough window to allow inter-frame movement not only for the keypoint, but also for the whole feature (e.g., building structure, billboard, road, etc.) to guarantee better results and reduce as much as possible user assistance during the pixel shift computation process. The compromise of having a larger zone-size is just related to the computation time that it will take for the cross-correlation algorithm to work on each frame. However, it is more important to be careful to not choose a very small zone where the feature (including the keypoint) might drift out of view, which in this case, would lead the cross-correlation algorithm to fail. A limitation of the method is that it requires the presence of fixed features in the camera view field. However, for fixed video systems where usually camera viewing angles shift slightly (e.g., less than 5°) and camera translational movements are small, a similarity transformation (4 DOF) can be performed to

stabilize the images with a minimum of two non-collinear pairs of keypoints between frames. The advantage of this approach, besides requiring fewer keypoints, is that it is computationally efficient and robust enough to achieve good results. Nevertheless, registration reliability and accuracy can be increased by selecting more landmarks in the image. Having more spread keypoints in the image reduces foreground-background bias and also allows the possibility to implement other more complex types of geometric transformations with higher degrees of freedom (Hartley and Zisserman, 2004), such as a 2-D affine (6 DOF) or planar nonlinear homography (8 DOF) transformation to remove perspective deformation introduced by the camera oblique view (really necessary for UAVs). The method has been tested on UAV flights (data not shown) showing that the performance largely improves (with 99% matches for case 1 and case 2) when using higher frequency frame rates (>1 Hz) during smaller periods of time (<20 min), although other geometric transformations with higher degrees of freedom are necessary due to the fact that camera translation movements become significant.

The time evolution of the transformation parameters show that camera movements occur on a wide range of timescales (see Figure 3.7). The annual signal in azimuth and tilt deviation can potentially be attributed to the sun position and thermal expansion fluctuations (Bouvier et al., 2019). It is important to note that all cameras were installed inside the lighthouse mounted in a wooden structure and isolated by an acrylic glass from the outside elements, so wind is not expected to be a source of camera motion for the present study. While movements were likely occurring for all cameras, the effects of azimuth and tilt motion were most notable for camera 2 (which had the longest focal length; 25 mm lens) and less evident for camera 3 (wide-angle 8 mm lens). This is in line with Pearre and Puleo (2009), who previously showed that the longer the focal length (e.g., 50 mm), the smaller the angle of view and the larger the sensitivity to cause significant changes in image location even for small changes in the tilt of the camera. Moreover, small changes in perspective were found to modify the size of the objects (uniform scaling) when objects were far away from the camera, as shown in Figure 3.7d for camera 1. On the other hand, the quasi-steady counter-clockwise trend observed in roll angle (Figure 3.7c) suggests that the wooden structure where the cameras are mounted is gradually arcing with time, although this cannot be verified.

Previous studies have shown that small camera viewing angle deviations can induce significant changes in image location and, in turn, introduce large geo-rectification errors (Pearre and Puleo, 2009; Bouvier et al., 2019; Bergsma et al., 2019). However, besides camera variation angles, the related error is also modulated with the pixel footprint that depends on the distance from the camera and the lens properties. For example, even though camera 2 presented the largest deviations in azimuth and tilt (see Figure 3.6), its associated geo-rectification error was slightly lower with respect to the other cameras for the same distances (see Figure 3.9d). This result might be explained by the fact that camera 2 has a higher pixel resolution and hence a lower pixel footprint that counteracts for the induced pixels real-world location error. Nevertheless, evidence still points out that geo-rectification errors induced by camera movement can become significant and should not be neglected. In an attempt to demonstrate the impact of this error (in perhaps the most common coastal video application), 2.5 km of shoreline were manually digitized for the outstanding winter period of 2013/2014 (Castelle et al., 2015; Masselink et al., 2016; Castelle et al., 2017a) using non-stabilized and stabilized time-exposure geo-rectified images to estimate the real-world horizontal positioning error due to camera movement (Figure 3.11). The mean shoreline position (intersection of wet and dry parts of the beach (Coco et al., 2005)) was defined as the alongshore-averaged shoreline position. The alongshore standard deviation of the shoreline position was also computed to give a measure of the alongshore variability of the cross-shore position. During the winter period of 2013/2014 high-energy wave conditions ($H_s > 5$ m) drove important changes in Anglet Beach shoreline dynamics (Huguet et al., 2016). Part of the seasonal erosion cycle is captured in Figure 3.11 where the shoreline position varied around a range of 30 m. The mean shoreline apparent position was also affected by an approximately 10-20 m bias showing that incorrect tilt may bias positions of features by condensing or stretching the image in the cross-shore direction. This result highlights that overlooking camera movement can result in strongly under- or over- estimation of shoreline response to extreme events.

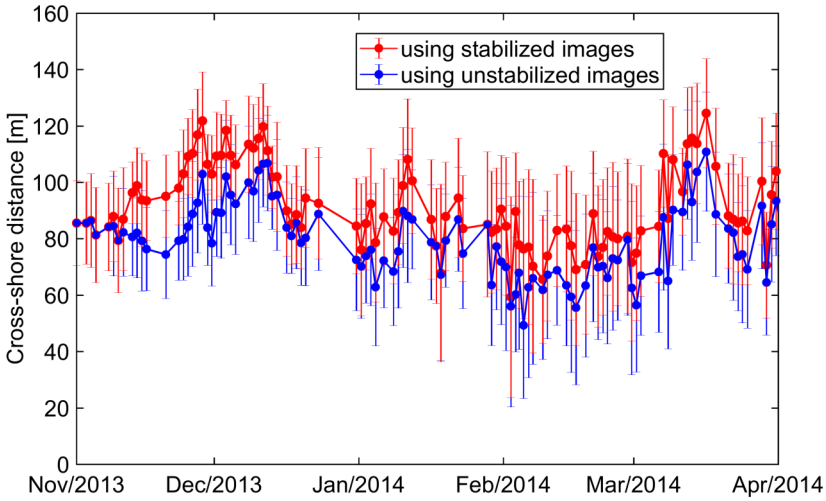

Figure 3.11 – Daily alongshore averaged shoreline position extracted from stabilized (red dots) and unstabilized (blue dots) geo-rectified images for the outstanding winter period of 2013/2014. The alongshore standard deviation of the cross-shore position is indicated by the vertical error bars.

3.3.7 Conclusions

In this paper, we developed an efficient semi-automatic method to remove unwanted camera movement after video acquisition. The method consisted in defining and tracking a few fixed feature points between consecutive frames using Guizar-Sicairos et al. (2007) sub-pixel cross-correlation algorithm together with a CED (Canny, 1986). The use of the CED greatly improved the performance of the cross-correlation algorithm by making it more robust against contrast and luminosity brightness variations. The tracked features allowed to compute the parameters of a similarity transformation (translation, rotation and scale) to estimate the motion between frames and compensate for it. For the keypoint matching, the method worked under a scheme of four cases. The algorithm was capable of computing automatically the 2-D sub-pixel shift of a keypoint with respect to an initial position as long as the displacements between consecutive frames remained smaller than 10 pixels. Otherwise, user input was required to discern if the calculated pixel shift was legitimate or the frame had to be discarded. Results showed that the semi-automatic method is able to process at least 90% of the frames without user assistance. However, future work should examine the possibility to automatically discard low-quality images acquired under adverse rain or foggy conditions in

order to reduce user intervention. Image stabilization is a fundamental post-processing step that should always be performed in coastal imaging applications to increase the accuracy of video-derived products, such as shoreline/sandbar position, wave celerity and depths estimate. The framework presented here opens new perspectives and appears as a promising tool for other coastal imaging applications such as removal of undesired high-frequency jitters from UAVs.

Chapter 4

Nearshore bathymetric mapping from video imagery

Contents

4.1 Preamble

This chapter comprises the results of the work performed during my second year of my PhD. Once the images were stabilized and corrected from camera movement, the main objective was to implement an existing video-based linear depth inversion algorithm (cBathy; Holman et al. 2013) in order to investigate PCA beach morphological response and time evolution during the storm events of October 2018 field campaign. One important aspect was to assess video-derived bathymetries with available topo-bathymetry surveys and evaluate the performance of cBathy under high-energy wave conditions since cBathy has been rarely tested in beach environments with waves larger than 2 m height.

The following sections of this chapter describe the most popular methods, currently available, for obtaining intertidal and subtidal bathymetry based on video remote sensing techniques. The spectral depth inversion method cBathy (Holman et al., 2013) is introduced, applied and discussed, and the results are placed into perspective with the limitations of the optical conditions and the physics assumptions.

4.2 Introduction

Bathymetry is probably the most critical variable for understanding and modelling the hydro-sedimentary processes and variability of the nearshore, yet it is often poorly known (Holman et al., 2013). Morphological changes of the beach profile are spread over a wide range of spatio-temporal scales that vary from a few hours (storm) to several weeks (changes in swell regimes) at the scale from ripples to sandbars. Decisions on coastal zone management are mainly based on understanding sediment budgets and the location and health of beach sand volumes (Davidson et al., 2007). This is a challenging task since, the impact on, and recovery rate of the sub- and inter-tidal zone varies greatly depending on the location (Masselink et al., 2016).

Until the 1990s, one common way of directly measuring beach profiles was through the use of bottom-contacting vehicles such as the Coastal Research Amphibious Buggy (CRAB; Birkemeier and Mason 1984) in combination with a fathometer to compile a comprehensive bathymetry. Nowadays, in situ bathymetric data is traditionally obtained using an echo sounder mounted behind a jet ski (Dugan et al., 2001) or a small vessel (MacMahan, 2001) equipped with a Real-Time Kinematic and Differential Global Positioning System (RTK DGPS) sensor that can retrieve depths within a couple of centimeters accuracy (Van Son et al., 2009). Although these methods are accurate, for logistical and economic reasons, in situ beach surveys are usually performed at most twice per month and are restricted to periods of fair weather conditions with low waves (Honegger et al., 2019). Consequently, considerable effort has gone into the development of a wide range of depth measurements techniques based on remote sensing that exploit various depth signatures in order to fill the spatial and temporal gaps in surveyed bathymetry Holland et al. (2018).

4.3 Indirect bathymetric mapping

The following subsections will give a brief overview regarding the research that have been done using remote sensing, with special focus on optical methods, to estimate the nearshore bathymetry.

4.3.1 Intertidal bathymetry mapping

Plant and Holman (1997) proposed the first method to map the intertidal beach bathymetry based on the composition of different shoreline elevation contours throughout a tidal cycle. Greyscale timex images are used to detect the shoreline (defined as the transition zone between beach pixels and water pixels) by extracting the pixel "Shore-Line Intensitiy Maximum" (SLIM) at which wave breaking is maximized. High-frequency intensities that are caused by individual waves and foam motion are smoothed by time-averaging images to isolate a mean shoreline position. As the tidal elevation is known at each time, the video-detected shoreline can be associated to a particular elevation. Thus, a time series of shoreline elevation contours from low tide to

high tide can be combined to reconstruct the three-dimensional intertidal bathymetry. Aarninkhof et al. (2003) improved this method by incorporating RGB-color timex images for an easier shoreline detection as well as concurrent tide and wave data. Pixels are clustered in a hue-saturation-value (HSV) color space where the shoreline is defined as the transition between water and land pixels. Almar et al. (2012b) extended this approach by using a Minimum Shoreline Variability (MSV) method to detect shorelines at complex meso-macro tidal beaches subject to high energy waves.

Although intertidal bathymetry mapping based on video techniques has proven to be very useful, it is not the main challenge of this work, as one can survey the intertidal zone by traditional means at low tide. The scope and interest relies on estimating the subtidal bathymetry which is both expensive and highly time consuming through surveys.

4.3.2 Subtidal bathymetry mapping

Maximum pixel intensities corresponding to wave breaking can also be used to estimate two- and three-dimensional subtidal morphology. For example, the location of the sandbar(s) can be determined by identifying one or more white alongshore bands of high intensity (Lippmann and Holman, 1989, 1990; Van Enckevort and Ruessink, 2003; van Enckevort et al., 2004). Several remote sensing approaches have been suggested to estimate the subtidal bathymetry. Among these group of methods are the one based on light penetration in the water column and the subsequent reflection of the seabed (see subsection 4.3.2.1) and the one based on sea surface characteristics. The latter group can broadly be subdivided into methods that rely on wave dissipation patterns caused by depth-induced wave breaking (see subsection 4.3.2.2) and changes in local wave celerity over a varying depth profile (see subsection 4.3.2.3).

4.3.2.1 Multi- and hyperspectral depth inversion

For clear water with a visible bottom, multi- or hyperspectral sensors display color variations that can be correlated to depth (Lyzenga and Ahrens, 1978; Lee et al., 1999; Mobley et al., 2005; Lyzenga et al., 2006). As different colors penetrate water at differ-

ent depths, the disparity between them can provide information about the depth. For example, Mobley et al. (2005) created a database based on remote-sensing reflectance according to different water depths, so that the measured reflectance for a particular image pixel could be matched with a look-up-table and inverted to retrieve water depth. Although this depth-by-colour method can provide relatively inexpensive high-spatial resolution bathymetry maps, the method generally requires in-situ ground calibration which limits this technique to accessible areas only (Almar et al., 2019). Moreover, inversion methods from multi- or hyperspectral satellite are subject to atmospheric and water clarity, while coastal waters in many areas of the world, including the current study site, are often turbid (Gao, 2009).

4.3.2.2 Depth estimation from wave energy dissipation

Local depth information can be obtained by coupling the pixel intensities to wave energy dissipation rates in relation to an underlying depth profile (Battjes and Janssen, 1978). Under this concept, Aarninkhof and Ruessink (2004); Aarninkhof et al. (2005, 2006) developed a method where cross-shore breaking-wave dissipation patterns from timex images are compared with numerical modelled dissipation proxies over a series of test bathymetries to find the one that is most consistent with observations. van Dongeren et al. (2008) extended this wave dissipation method through a data-model assimilation framework called Beach Wizard. Moreover, Wilson et al. (2010) showed that through further data assimilation (the addition of wave and current measurements) using an ensemble Kalman filter, the accuracy of an updated modelled bathymetry can be enhanced. The main drawback of wave energy dissipation methods is that evidently they are limited to wave breaking areas (e.g., surf zone) and require full numerical model run for each guess which makes it difficult for operational purposes.

4.3.2.3 Depth inversion through wave dispersion relationship

One of the most common approach to estimate water depth is through the wave dispersion relationship which for the simplest case is derived from linear wave theory under the assumption of small amplitude waves and locally horizontal bottom. In this case, the radial frequency ω ($2\pi/T$) is directly related to the water depth h, the gravitational

acceleration (g) and the radial wave number k ($2\pi/L$), as shown in the following equation:

$$\omega = \sqrt{gk\tanh(kh)} + uk. \tag{4.1}$$

The term uk accounts for the Doppler shift due to mean currents (u). This term is often neglected for open beaches with small influence of rip currents since u is considered to be small compared to the wave celerity in the same direction as u. Wave celerity or phase speed c in the absence of Doppler shifts is expressed as:

$$c = \frac{\omega}{k} = \frac{L}{T}. \tag{4.2}$$

From Eq. 4.1 and 4.2 the celerity of a wave, based on linear wave theory is:

$$c = \sqrt{\frac{g}{k}\tanh(kh)}, \tag{4.3}$$

which can be inverted to estimate the water depth:

$$h = \frac{\tanh^{-1}(\frac{c^2k}{g})}{k} = \frac{\tanh^{-1}(\frac{\omega^2}{gk})}{k} = \frac{L}{2\pi}\tanh^{-1}\left(\frac{2\pi L}{gT^2}\right) \tag{4.4}$$

Attemps to retrieve nearshore bathymetry from Eq. 4.4 have been investigated since World War II (Williams, 1947). Sequences of air photos of enemy-held beaches were manually analyzed to determine wavelengths L and wave periods T (Johnson, 1949; Fuchs, 1953). Nowadays, the use of depth inversion from linear wave dispersion has been extended to X-Band radars (Bell, 1999; Bell and Osler, 2011), satellites (Mancini et al., 2012; Bian et al., 2020) and of course video-monitoring stations (Stockdon and Holman, 2000; Holman et al., 2013). It is important to note that the linear dispersion relation implies that depths can only be inverted to a limited depth which theoretically corresponds to intermediate water depths (in practice: $h < L/2$). The validity of the linear dispersion relation is also bounded to the increasing degree of wave nonlinearity (finite amplitude effects) as waves approach the shore leading to larger propagation speeds for higher waves (Grilli, 1998; Bergsma and Almar, 2018). Correction for finite-amplitude dispersion in shallow water requires a modification in the wave celerity equation, i.e., $c = \sqrt{g(h+H)}$ which implies knowledge of the wave height H that is

usually unknown and difficult to obtain remotely. Examples of depth inversion through non-linear wave dispersion relationship are addressed by Holland (2001); Catálan and Haller (2008); Almar et al. (2011). The application of non-linear depth inversion requires either in-situ wave data or a computation effort which is additional compared to the linear dispersion relationship (Bergsma, 2017).

Two different approaches for depth inversion using the linear dispersion relationship are applied in nearshore video camera systems; a temporal and a spectral method (Bergsma and Almar, 2018). The temporal method (Almar et al., 2009) correlates time-varying wave signals between neighboring positions from timestack images to find the best correlation that is related to wave celerity. The spectral method (Plant et al., 2008; Holman et al., 2013) transforms a spatial neighborhood of pixel intensity time series to the frequency domain for cross-spectral analysis and complex Empirical Orthogonal Function (EOF) analysis in order to derive the most coherent and dominant frequency and wavenumber pairs. Although both approaches result in depth estimates with similar accuracy using synthetic cases (Bergsma and Almar, 2018), the spectral method has the advantage to be extended into two spatial dimensions while the cross-correlation temporal method is limited to one-dimension and subject to errors for an oblique wave incidence angle (Thuan et al., 2019). Another advantage of the spectral method over the temporal method is that a larger amount of signals in space and time are used for each point where the bathymetry is intended to be estimated. For weakly monochromatic noisy wave conditions, the spectral method is then often more robust than the temporal method (Bouvier, 2019).

The cBathy algorithm, developed by (Holman et al., 2013), is a spectral depth inversion method that has been widely used in nearshore regions (intermediate and shallow water) to remotely estimate bathymetric data (Brodie et al., 2018). It incorporates a temporal Kalman filter (Kalman, 1960) based on present and prior bathymetric estimates to provide robustness in case of sporadic camera or weather problems such as fog or rain. Although cBathy was originally conceived for fixed shore-based coastal monitoring video stations, its implementation has also been tested on X-band radars (Honegger et al., 2019, 2020) and UAVs (Aarnink, 2017; Bergsma et al., 2019). The cBathy algorithm consist of three phases that will be explained in the section below.

4.4 cBathy algorithm

The cBathy algorithm (Holman et al. 2013; https://github.com/Coastal-Imaging-Research-Network/cBathy-toolbox) is based on the linear wave dispersion relationship to estimate depth and thus requires a time series of images with the presence of waves in intermediate and shallow water. Images are typically sampled at 1 or 2 Hz over a 17-min collection to yield a burst or stack of images. Data runs are typically collected hourly but can be reduced to half-hourly for field experiments or places where conditions (for example, tide or morphology) change rapidly. The image spatial resolution should be adequate to resolve the anticipated dominant wavelengths. It is recommended that no fewer than four pixels per expected wavelength be used for sampling. For the case of Anglet beach, the wavelength for a typical 10-s wave in 1 m depth is ∼31 m. This means that for a cross-shore (Δx_p) and alongshore (Δy_p) spacing of 5 and 10 m, respectively, 6 points will be provided in the cross-shore to resolve the wavelength, which is fine to keep computation time reasonable (alongshore scales are longer, so can be well resolved with a larger sample spacing). Once the stack of images is recorded the analysis is carried out sequentially at a series of user-selected analysis points (x_m, y_m) for which a group of neighboring pixels is used within a user-specified range $(x_m \pm L_x, y_m \pm L_y)$ or tile (Figure 4.1).

cBathy algorithm consist of three processing steps or phases. The objective of phase 1 is to estimate a wavenumber k at the point (x_m, y_m) for a user-defined set of candidate frequencies f_b. These frequencies f_b are typically defined between 0.056 and 0.250 Hz and correspond to wave periods ranging from 4 to 18 s. Each pixel within the analysis tile $(x_m \pm L_x, y_m \pm L_y)$ is treated as an individual pixel intensity time series and converted to the frequency domain through a Fourier transformation. A cross-spectral matrix is then computed between all possible pixel pairs inside the tile for each of the desired frequency bands f_b. A selection of the most coherent frequencies (commonly four; cBathy default value) are identified and extracted through spatial empirical orthogonal function (EOF) to determine the dominant spatial phase of the wave. The corresponding wavenumbers k are derived by fitting the wave patterns of the observed spatial phase to a forward modelled wave train. A skill value is provided to indicate the percentage

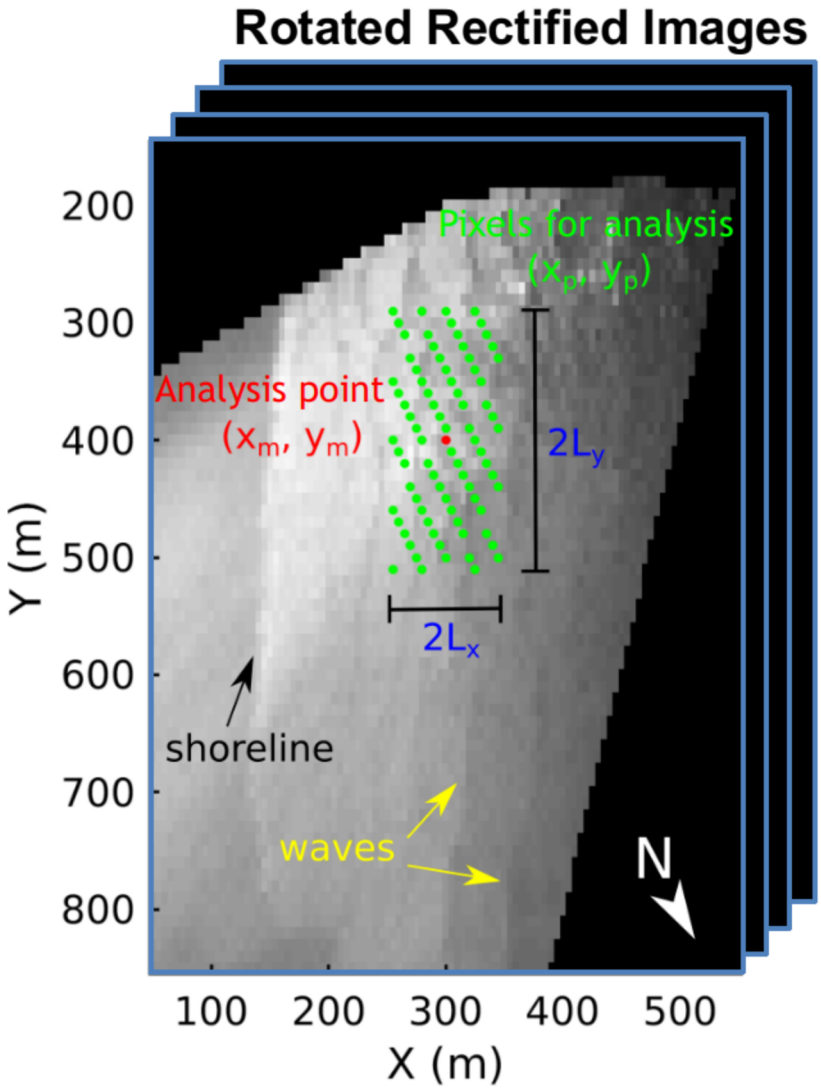

Figure 4.1 – Pixel array used for cBathy analysis. Time series are collected at every pixel. Analysis at any example location (e.g., red dot) is based on data from the surrounding tile of pixels (green dots) of size +/- L_x and L_y. The image is rotated, since cBathy assumes that the x-axis increases offshore.

of the variance explained by the fit where a skill score of 1 corresponds to a perfect match. Finally, for each $f_b - k$ pair, a depth $\tilde{h}(x_m, y_m)$ can be estimated using the linear dispersion relationship (Eq. 4.4). Since cBathy estimates depth, not bathymetry, tidal elevations must be subtracted from estimates to yield depths relative to a fixed tidal datum.

In phase 2, a single depth $\hat{h}(x_m, y_m)$ is computed by combining the multiple $f_b - k$ pairs estimated from phase 1 through a weighted non-linear least squares fit so that the best correspondence to the linear dispersion relationship is found. Phase 2 depths,

like those of phase 1, must be tide-corrected to yield bathymetry data referenced with respect to a tidal datum.

Phase 3 uses a Kalman filter (Kalman, 1960) to smooth and average the datum-referenced depths in order to provide a robust and reliable depth estimate, $\overline{h}(x_m, y_m)$. As the Kalman filter depends on both the current and the previous cBathy-estimated bathymetry, this step only works if more than one video-derived bathymetry is available. The purpose of the Kalman filter is to provide an estimate of beach morphology over certain areas even when in situ conditions are not favorable by filling gaps in coverage and objectively averaging new estimates with prior estimates.

4.5 cBathy results and previous validation

The quality of bathymetric estimates derived from cBathy has previously been compared with conventional bathymetric surveys obtained from echo sounder and acoustic altimeters for a number of different beaches (summarized in Table 4.1). However, cBathy has rarely been tested in beach environments with waves bigger than 1.7 m, and almost never in presence of waves bigger than 2 m with T_p >10 s due to the difficulty of conducting in situ surveys in the presence of large waves (Brodie et al., 2018). As shown in Table 4.1, the discrepancies between measured and computed (cBathy) bathymetric data range from 0.34 to 2.05 m and from 0 to 0.92 m, RMSE and bias, respectively. The error variability depends largely on the resolution of the video system, site morphology, and hydrodynamic conditions at the time of acquisition. Maximum errors are usually located offshore, several hundred meters away from the video system due to the alteration of the pixel footprint, and close to the shoreline where analysis tiles tend to mix information from waves, swash and static dry sand (Holman et al., 2013). Moreover, saturation of the surf zone, due to (large) waves breaking, affects the readability of the wave signature and thus compromises the accuracy of cBathy performance (Bouvier et al., 2020). As stated before, errors are often larger in shallow waters where linear theory becomes less valid due to wave breaking and finite amplitude effects (Holland et al., 2001; Bergsma and Almar, 2018).

Table 4.1 – cBathy performance statistics from prior work, organized by decreasing H_s. Adapted from Brodie et al. (2018).

Date	H_s [m]	T_p [s]	Bias [m]	RMSE [m]	Tide [m]	Location	# Obs.	Reference	Notes
Sep/2015 to Sep/2016	0.3-4.3 m	4-18	-0.26	0.75	-	Beach near Duck, NC, USA	8	Brodie et al. (2018)	
2009-2011	0.25-2.00	-	0.19	0.51	0.98	Duck, NC, USA	16	Holman et al. (2013)	
Mar/2013 to Mar/2014	<1.65	-	0.59	0.79	-	SandEngine Netherlands	6	Rutten et al. (2016)	-10<depth<-5 m
Mar/2013 to Mar/2014	<1.65	-	-0.01	0.34	-	SandEngine Netherlands	6	Rutten et al. (2016)	-5<depth<-1 m
Mar/2013 to Mar/2014	<1.65	-	-0.92	0.34	-	SandEngine Netherlands	6	Rutten et al. (2016)	-1<depth<0 m
4-13/Dec/2016	1.52	9.2	-	1.28	0.4-1.6	Saint Louis, Senegal	1	Bergsma et al. (2019)	$\hat{h}$ results; via UAV
13/Jul/2013	-	7.1	-0.41	0.56	>3	Agate Beach, OR, USA	1	Holman et al. (2013)	
17/May/2012	1.19	5-7	0	0.52	-	New River Inlet, NC, USA	1	Holman and Stanley (2013)	
10/Apr/2014	1.16	10.5	-	1.06	2.78	Porthowan, Cornwall, England	1	Bergsma et al. (2016)	
9-17/Sep/2010	0.5-1	-	0.26	0.49	-	Duck, NC, USA	1	Honegger et al. (2019)	via X-band radar
July-Aug/2013	-	-	0.11	0.35	-	Benson Beach, WA, USA	1	Honegger et al. (2019)	via X-band radar
Feb/2017	0.70-0.97	-	-	0.37-0.87	-	Scheveningen, Netherlands	1	Aarnink (2017)	via UAV
20/Feb/2013	0.64	5.8	-0.18	1.01	1.4-1.9	Kijkduin, Netherlands	1	Wengrove et al. (2013)	$\hat{h}$ results
17/Abr/2014	0.52	10.4	-	2.05	6.03	Porthowan, Cornwall, England	1	Bergsma et al. (2016)	
Jan-Mar/2018	0.52	8	0.01	0.38	0.2	Lido of Sète, France	1	Bouvier et al. (2020)	
Jul-Dec/2018	0.52	8	0.02	0.37	0.2	Lido of Sète, France	1	Bouvier et al. (2020)	
1-4/Jul/2013	<0.50	-	-	0.48-0.66	-	SandEngine Netherlands	1	Radermacher et al. (2014)	
17/Feb/2013	0.22	8.5	-0.5	1.27	1.4-1.9	Kijkduin, Netherlands	1	Wengrove et al. (2013)	$\hat{h}$ results
	Average:		-0.08	0.72					

4.6 cBathy settings for PCA beach field experiment

The objective of this study is to determine PCA beach morphological time evolution during October 2018 field experiment and assess the ability of cBathy algorithm to estimate nearshore bathymetries under high-energy waves. For this purpose, 1-Hz sampled images were continuously collected during daylight hours on 5,8-15,18-30/Oct/2018 (Figure 2.8d and 4.5). Images were collected from a single camera (cam4) located on top of Biarritz lighthouse (Figure 2.6 and 2.7). Following subsection 4.4, time series of images were rotated and rearranged into stacks of ∼17 min (1024 s) duration yielding one image-stack every 30 min. cBathy algorithm (v1.2) was then applied to a total of 330 image-stacks. The parameters used for cBathy are shown in Table 4.2. Time series of water depth were estimated on a 25×10 m analysis grid (alongshore × cross-shore spacing) and further referenced to NGF-IGN69 (Global French Levelling) to produce bathymetry maps. The Kalman filter was then consecutively applied over time to yield a stable running average depth by automatically weighting better estimates from prior information. It should be noted that for the 5^{th} of October 2018 (the same day as the first bathymetry survey) only one image-stack was available, meaning that the Kalman filter could not be applied during that day.

Table 4.2 – cBathy Parameters used for October 2018 field experiment.

Description	Value
Pixel cross-shore spacing (Δx_p)	5 m
Pixel alongshore spacing (Δy_p)	10 m
Cross-shore depth analysis spacing (Δx_m)	10 m
Alongshore depth analysis spacing (Δy_m)	25 m
Cross-shore analysis smoothing scale (L_x)	30 m
Alongshore analysis smoothing scale (L_y)	75 m
Temporal resolution (Δt)	1 s
Record length of each stack (τ)	1024 s
Number of stacks (N_{stack})	330
Minimum acceptable depth (h_{min})	0.25 m
Analysis frequency bins (f_b)	$\left[\frac{1}{18\,s} : \frac{1}{100\,s} : \frac{1}{4\,s}\right]$
Number of frequency bins to retain (N_{keep})	4

4.7 Topo-bathymetry surveys comparison

As previously described in subsection 2.2.1, during October 2018, several surveys were conducted with the purpose to quantify inter- and sub-tidal morphological variations throughout the experiment. Inter-tidal topography surveys were performed on 15 and 24 October, and bathymetry surveys were performed on 5 and 26 October 2018. As shown in Figure 4.3, comparison between surveys indicate the formation of an alonghore uniform sandbar centered at cross-shore position = 300 m with a net deposition of sand (around 1-m of accretion) at the respectively longshore and cross-shore position (400 m, 300 m). The overall erosion in the cross-shore distance between 400 and 600 m indicates an overall onshore sediment transport that drove the development of the bar, as well as beach accretion (at cross-shore position ≈ 100 m), despite the moderate- to high-energy wave conditions during that period. The development of a shallow rip channel is also observed at alongshore distance = $400-500$ m and cross-shore distance = 250 m.

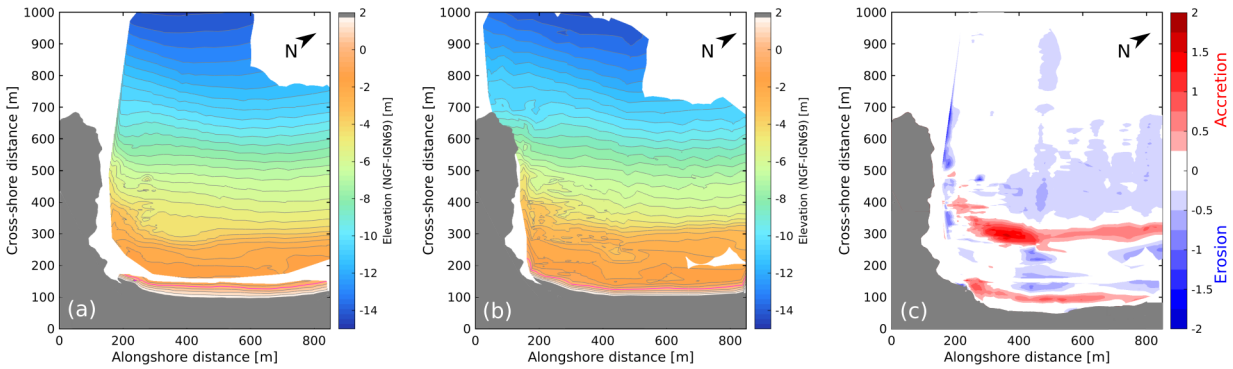

Figure 4.2 – Topo-bathymetry surveys comparison. (**a**) Interpolated bathymetry (05/Oct/2018) and intertidal topography (15/Oct/2018). (**b**) Interpolated bathymetry (26/Oct/2018) and intertidal topography (24/Oct/2018) merged together into a single bathy-top map. (**c**) Difference between surveys where red colors indicate sand accretion and blue colors sand erosion.

It was decided not to merge the bathymetry data collected on 5 October with the topography collected on 15 October, as a high-energy wave event occurred between both dates (H_s up to 4 m on 7 October 2018; see figure 2.8) potentially inducing changes in the sea bed morphology. On the other hand, the topographic and bathymetric data collected on 24 and 26 October 2018, respectively, were interpolated and merged together to produce a single bathy-topo map. Thus, only the bathymetry data (05/Oct/2018), as well as the topo-bathymetric ensemble (24,26/Oct/2018) representing the morphological conditions during the beginning and end of the experiment, respectively, will be used as ground truth to further validate cBathy estimations.

4.8 cBathy results

4.8.1 cBathy video-derived bathymetries vs. surveys

Figure 4.3 presents the non-filtered cBathy bathymetry estimation computed for the same day as the first bathymetry survey (05/Oct/2018). Wave and tide conditions during cBathy computation (H_s = 0.55 m; T_p = 12.5 s; θ_p = 3.6°; Tide = 1.58 m) showed no wave breaking as illustrated in the standard deviation image (Figure 4.3a). The bulk performance of cBathy to reproduce morphological features present in the first bathymetry survey achieves 0.57 m root-mean-square-error (RMSE) with 0.37 m bias. The intermediate water region comprised between alongshore distance = 350−800 and

cross-shore distance = 300−450 is well reproduced by cBathy. However, the remaining shallow water regions, including the sandbar, are fairly reproduced in shape, but overestimated in depth (inaccuracies around 1 m), as shown in Figure 4.3d and the cross-shore and alongshore profile transects in Figure 4.3e,f.

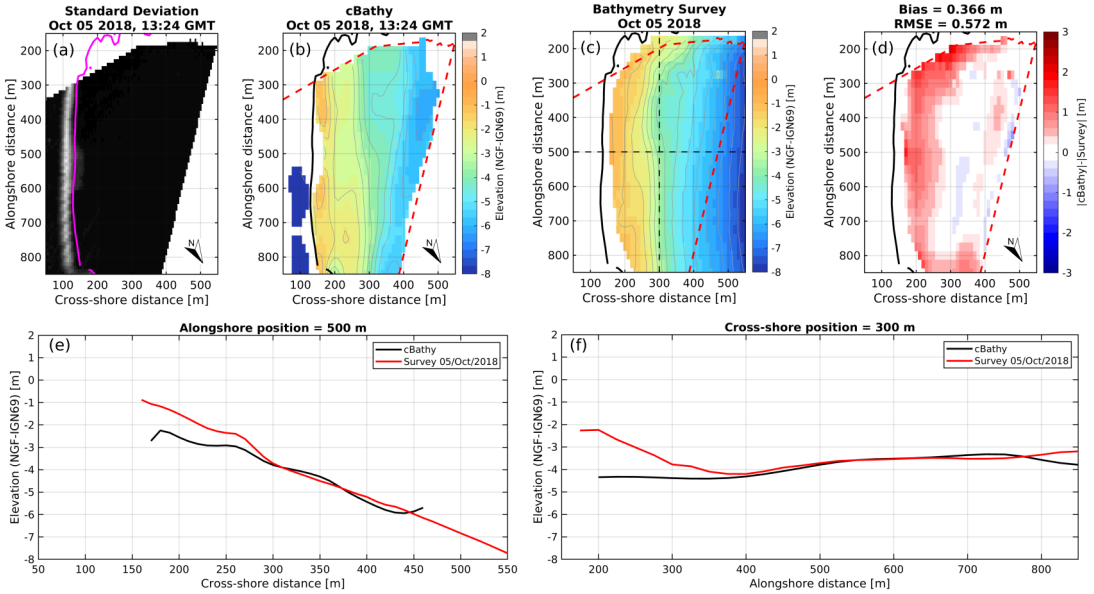

Figure 4.3 – cBathy vs. surveyed bathymetry for the 5^{th} of October 2018. (**a**) Standard deviation image to highlight preferential wave breaking; the magenta line indicate the zero-elevation contour. (**b**) cBathy-derived bathymetry, (**c**) surveyed bathymetry and (**d**) difference between both, where red (blue) colors indicate depth overstimation (underestimation) in cBathy results. (**e**) Cross-shore and (**f**) alongshore transects, indicated by the black dashed lines in panel (**c**), showing the comparison bewteen cBathy (black solid line) and the surveyed profile (red solid line).

Figure 4.4 shows the estimated Karman-filtered cBathy bathymetry corresponding to the topo-bathymetry survey conducted by the end of the field experiment (24,26/Oct/2018). The standard deviation image (Figure 4.4a) depicts an oblique rip channel within the surf zone between alongshore distance = 400-500 consistent with the surveyed topo-bathy map (Figure 4.4c). However, this rip channel is not resolved by cBathy estimations. cBathy shows an overall RMSE and bias of 0.56 and 0.29 m, respectively, with larger errors near the steep shoreline and reef location, as shown in Figure 4.4d and the cross-shore and alongshore profile transects in Figure 4.4e,f. cBathy performance is hypothesized to be lowered by wave breaking due to low tide and relatively large waves (H_s = 0.85 m; T_p = 12.5 s; θ_p = 16°; Tide = -1.28 m).

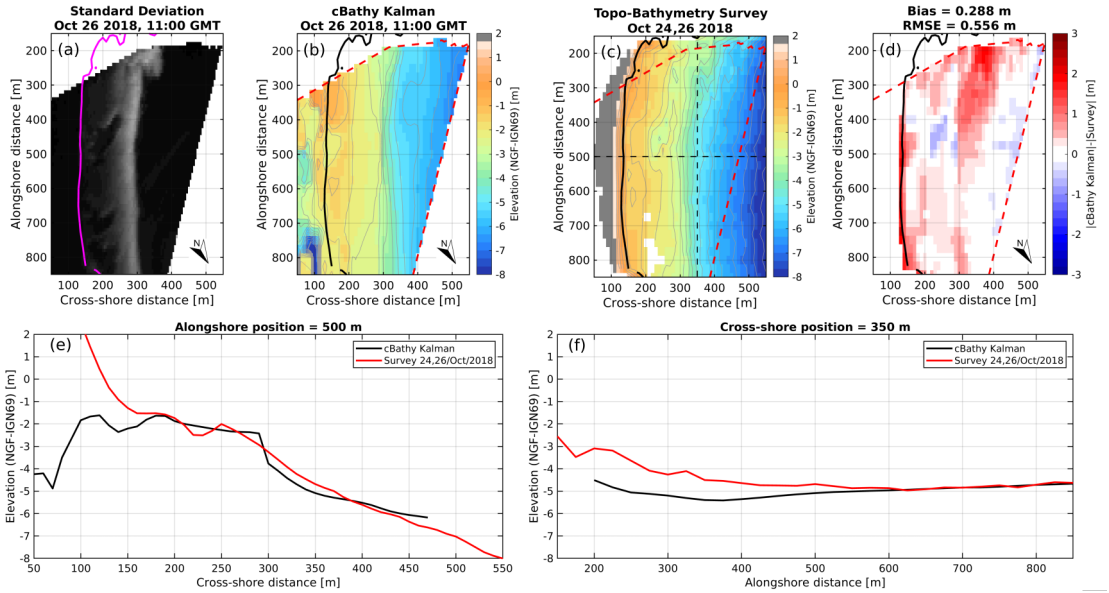

Figure 4.4 – cBathy (26/Oct/2018) vs. interpolated topo- (24/Oct/2018) bathymetry (26/Oct/2018) survey. (**a**) Standard deviation image to highlight preferential wave breaking; the magenta line indicates the zero-elevation contour. (**b**) cBathy-derived bathymetry, (**c**) surveyed topo-bathy and (**d**) difference between both, where red (blue) colors indicate depth overstimation (underestimation) in cBathy results. (**e**) Cross-shore and (**f**) alongshore transects, indicated by the black dashed lines in panel (**c**), showing the comparison bewteen cBathy (black solid line) and the surveyed profile (red solid line).

4.8.2 cBathy video-derived morphological evolution

Figure 4.5 shows the two bathymetric surveys conducted on 5 and 24-26 October 2018 (top panels), as well as six of the most representative cBathy video-derived bathymetries. Standard deviation images are also included to highlight preferential wave breaking and provide visual aid to detect morphological features and validate if they are in agreement with the corresponding bathymetric estimates. The hours of video recording from which the 330 bathymetries were computed are indicated over the time series of tidal elevation and significant wave height H_s. The bathymetry time evolution shows the transition from a Low Tide Terrace (LTT) to a Transverse Bar and Rip (TBR) beach state according to Wright and Short (1984) classification. During the beginning of the field experiment, the sandy bed morphology was reasonably uniform alongshore showing a terrace bar attached to the shore with a slight central crest located around 250 m in the cross-shore. At high tide when waves were less than 1 m height, waves passed over the sandbar without breaking until they reach the beach face, much like in a reflective beach. Throughout the experiment wave energy increased over time ($H_s > 1$ m up to 4 m on 07/Oct/2018) inducing the formation of rip channels with an oblique orientation and thus introducing morphological discontinuities in the surf zone area.

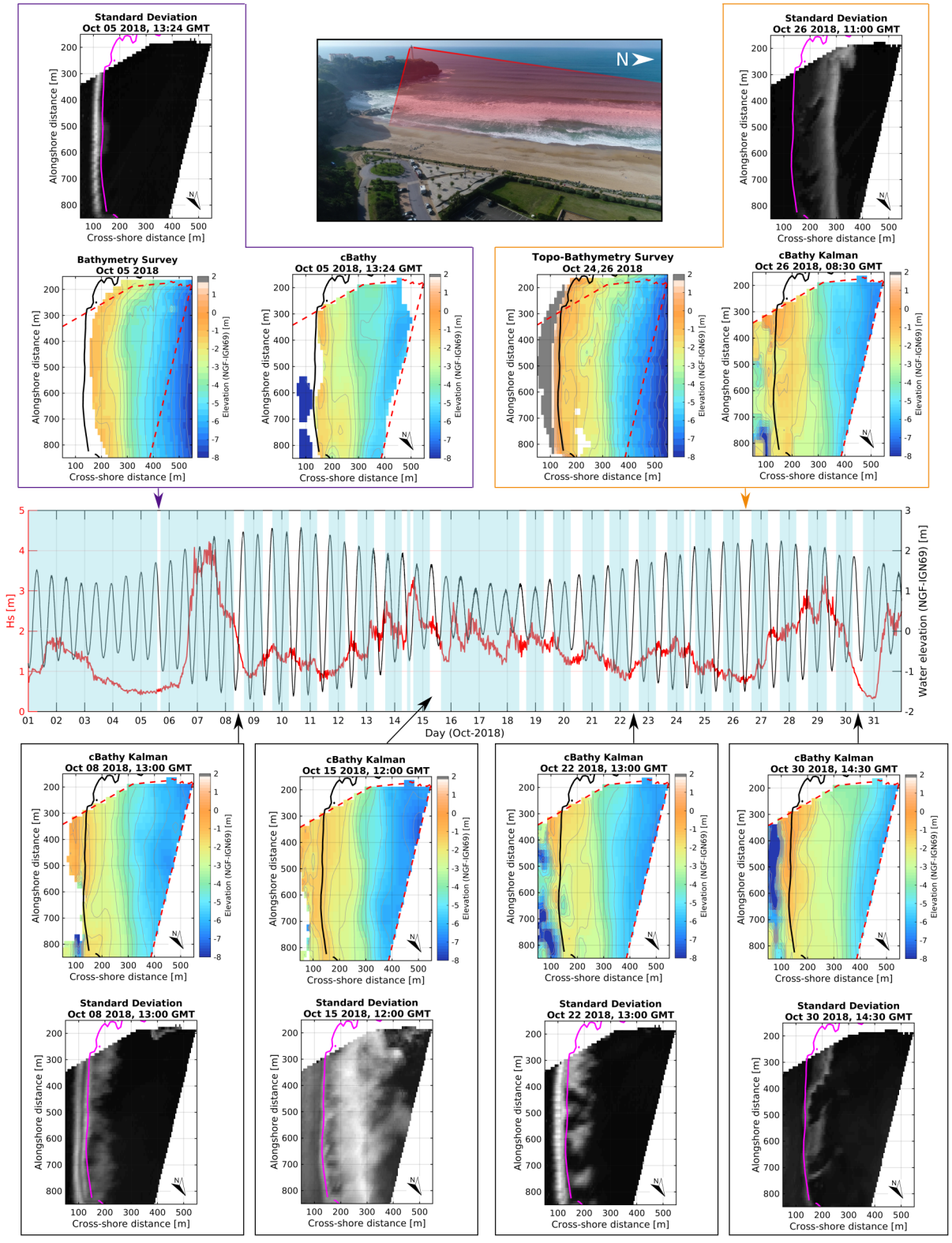

Figure 4.5 – cBathy video-derived bathymetries during October 2018 field experiment. The middle panel shows the wave and tide conditions during cBathy implementation. Non-shaded regions in the time series indicate video recording during daylight hours. The magenta and black lines depict the zero elevation contour line and the red line indicates the camera monitoring area. Standard deviation images are included to emphasize preferential wave breaking and provide visual aid to identify morphological features.

4.8.3 cBathy video-derived profile response

Different cross-shore profile transects were selected (Figure 4.6e) to investigate the temporal evolution of the sandbar position over the 3-week field experiment. Wave and tide conditions are presented in order to associate morphological evolution to hydrodynamic conditions at PCA beach (Figure 4.6a). Unexpectedly, all beach profiles (Figure 4.6e,f,g) show an unusual diurnal fluctuation in depth (around 1- to 1.5-m depth amplitude). A close inspection of the profile temporal evolution reveals a direct tide dependency on this high-frequency depth fluctuation, where high (low) tide is associated with deeper (shallow) profiles. This non-physical depth inaccuracy was removed by applying a moving-average with a temporal window of two (daylight) days over the whole bathymetry time series.

The smoothed cross-shore profile time-evolution (Figure 4.7e) shows an overall sand deposition close to the reef by the end of October 2018 linked by the increasingly energetic wave conditions after 27 October 2018, which is consistent with the sand accretion for the same region in the topo-bathymetric survey conducted at the end of the experiment (Figure 4.3c). The temporal evolution of the smoothed cross-shore profile transect centered at alongshore distance = 700 m (Figure 4.7g) illustrates the temporal detachment of the sandbar from the beach face creating a rip channel on 20-22/Oct/2018 (see standard deviation images for the same period in Figure 4.5). Overall, the cBathy-derived cross-shore profiles transects (Figure 4.7h,i,j) are consistently below the surveyed profiles with a positive bias of around 1 m depth.

Similarly, Figure 4.8 shows PCA beach 2-day time-averaged vertical profile response over time for three different alongshore transects depicted in Figure 4.8e,f,g. A systematic change in sea bed elevation is evident after 23 October 2018 with more sand accumulation close to the reef's alongshore-distance location ($\sim$300 m). The temporal evolution of the alongshore transect corresponding to the shallowest sub-tidal region (Figure 4.8f) shows an overall bias with respect to the ground truth surveys that might be related with non-linear effects resulting in depth overestimation.

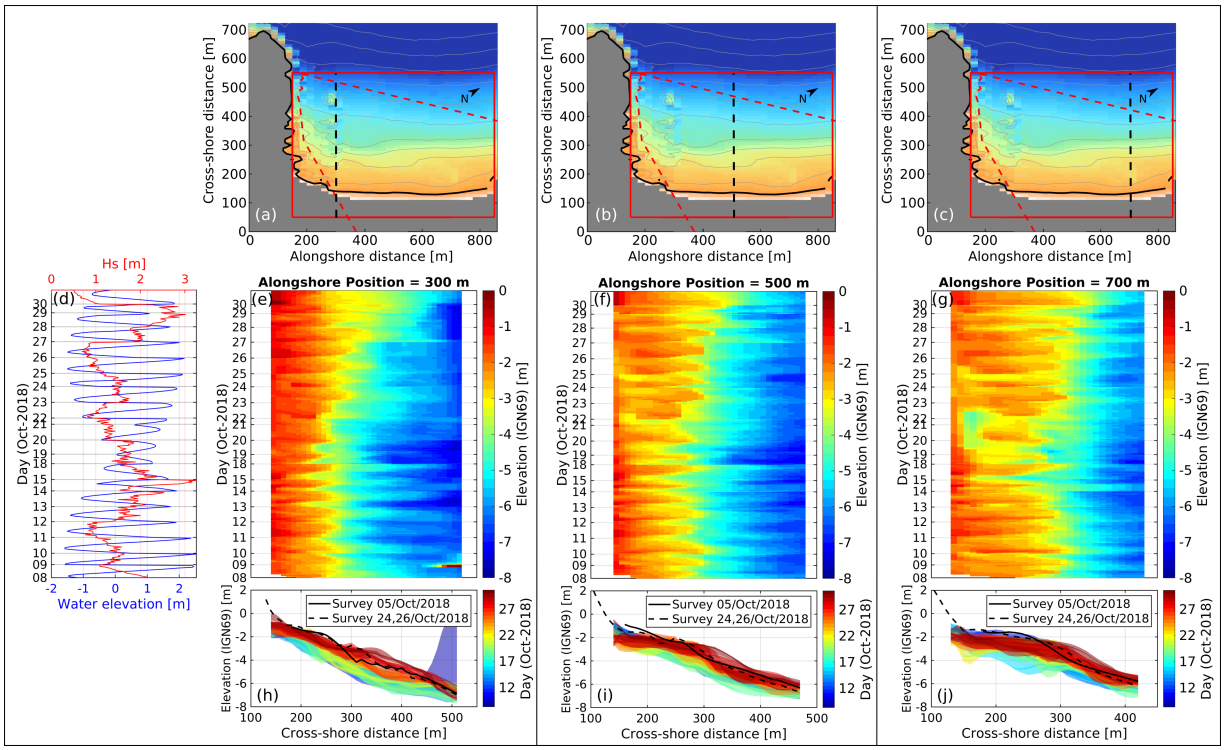

Figure 4.6 – PCA beach cross-shore profile morphological evolution over October 2018 derived from cBathy estimates. (**a,b,c**) The cross-shore profile transects are indicated by the black dashed lines. (**d**) Offshore significant wave height H_s (red line) and tidal elevation (blue line) time series corresponding to the computed cBathy Kalman-filtered stacks. (**e,f,g**) cBathy-derived timestacks along with (**h,i,j**) the time evolution of each cBathy cross-shore profile (shown with different colors). The solid and black dashed lines correspond respectively to profile transects obtained from bathymetry (05/Oct/2018) and topo-bathymetry (24,26/Oct/2018) surveys. For better visualization, the time is concatenated during available cBathy stacks (e.g., nightlight hours and absent data from 16 and 17 October are removed).

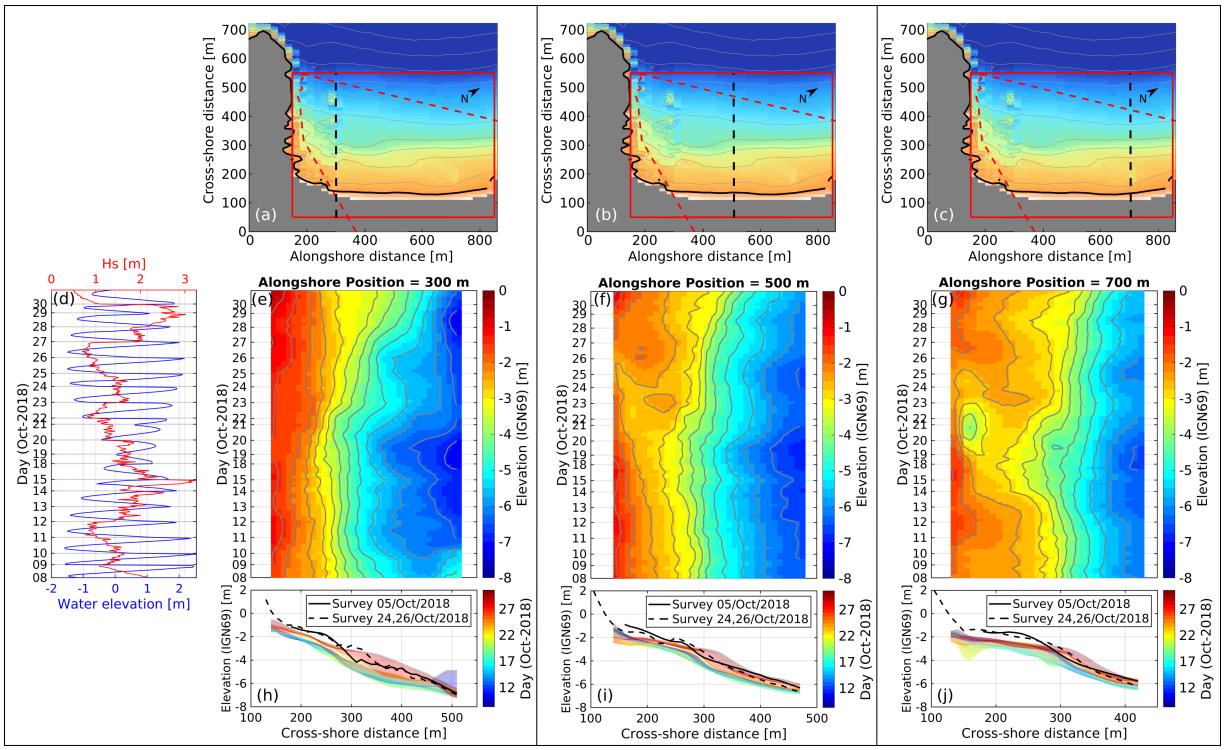

Figure 4.7 – PCA beach cross-shore profile morphological evolution over October 2018 derived from 2-day time-averaged cBathy estimates. (**a,b,c**) The cross-shore profile transects are indicated by the black dashed lines. (**d**) Offshore significant wave height H_s (red line) and tidal elevation (blue line) time series corresponding to the computed cBathy Kalman-filtered stacks. (**e,f,g**) cBathy-derived timestacks along with (**h,i,j**) the time evolution of each cBathy cross-shore profile (shown with different colors). The solid and black dashed lines correspond respectively to profile transects obtained from bathymetry (05/Oct/2018) and topo-bathymetry (24,26/Oct/2018) surveys. For better visualization, the time is concatenated during available cBathy stacks (e.g., nightlight hours and absent data from 16 and 17 October are removed).

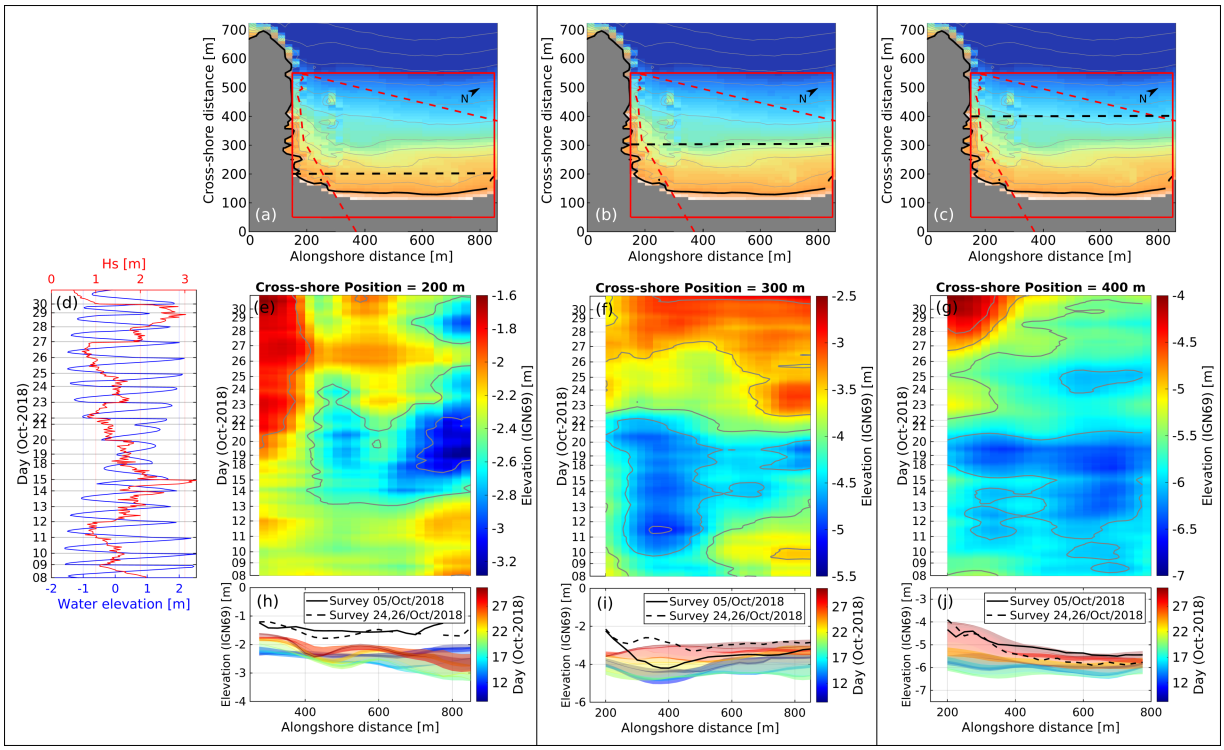

Figure 4.8 – PCA beach alongshore profile morphological evolution over October 2018 derived from 2-day time-averaged cBathy estimates. (**a,b,c**) The alongshore profile transects are indicated by the black dashed lines. (**d**) Offshore significant wave height H_s (red line) and tidal elevation (blue line) time series corresponding to the computed cBathy Kalman-filtered stacks. (**e,f,g**) cBathy-derived timestacks along with (**h,i,j**) the time evolution of each cBathy alongshore profile (shown with different colors). The solid and black dashed lines correspond respectively to profile transects obtained from bathymetry (05/Oct/2018) and topo-bathymetry (24,26/Oct/2018) surveys. For better visualization, the time is concatenated during available cBathy stacks (e.g., nightlight hours and absent data from 16 and 17 October are removed).

4.9 cBathy error assessment

Following the approach proposed by Bouvier et al. (2020), a quality assessment was computed for each of the non-filtered cBathy-derived bathymetries $\hat{h}(x_m, y_m)$ by counting the number of points for which the cBathy algorithm returns a physical value (skill higher than 0.5 with associated depth errors lower than 1 m). The quality assessment (Qual) of video-derived bathymetries was assessed in percentage terms in relation to the total number of grid points inside the camera viewfield delimited by values below the zero-elevation contour line. In other words, the quality assessment counts how many non-NaN depth estimates are retrieved from cBathy within the sampled area. Figure 4.9 shows the cBathy quality assessment for the 330 computed bathymetries according to their corresponding tidal elevation and offshore significant wave heights (H_s).

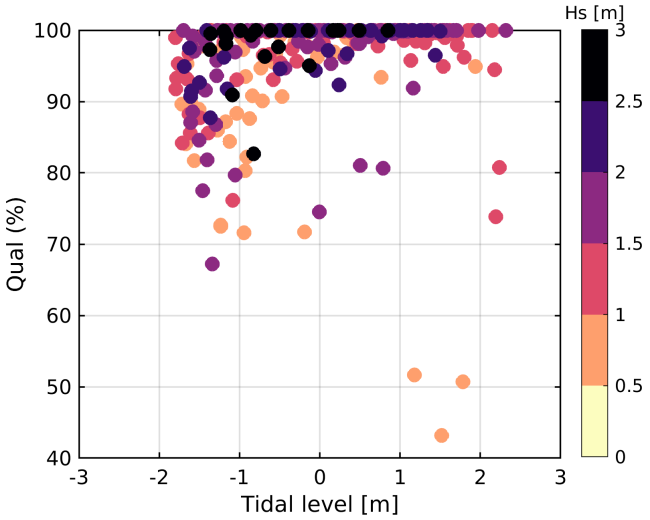

Figure 4.9 – Bathymetric inversion quality (Qual) as a function of tidal elevation (with respect to MSL) and offshore significant wave height (H_s).

Tidal elevation has an influence on the quality of depth inversion with appreciable errors associated to low tide stage. During low tide, waves break over the reef and sandbar affecting the readability of the wave signature and resulting depth estimates. Surprisingly, large waves ($H_s > 2$ m) do not appear to significantly reduce cBathy estimations in the sampled area, as opposed to Bouvier et al. (2020) results. Nevertheless, it is important to note that this quality assessment is based only on the total number of individual depth outputs within the grid which performance at the end is given by the same cBathy algorithm.

4.10 Discussion

Video-derived bathymetry estimations showed noticeable depth deviations modulated by a diurnal signal dependent on the tide. As only half of the tide-period is captured during daylight hours video-recording, depth deviations appear to fluctuate around a diurnal cycle (rather than at the semi-diurnal tide) due to an aliasing effect. Tide-dependent bias in cBathy depth estimation has been previously addressed by Bergsma et al. (2016) as a consequence of the limited inclusion of tidal elevation in the code. cBathy assumes fixed geographical pixel locations over the entire stack period. As described by Bergsma et al. (2016), the pixel spatial footprint changes as the water level rises and lowers with the tide. As the water level rises, pixels move towards the camera contracting its size, while during a falling tide the opposite occurs, a relative expansion of the pixel footprint is produced as the distance with the camera increases (see Figure 4.10). Incorrect pixels positions result in a shorter sensed wavelength than in reality at low tide, leading to an overestimation of the wave number and thus an underestimation of the depth, and vice versa for high tide. To overcome this issue, before cBathy computation, we rectified all images within a ∼17 min stack by setting the reference level (tidal elevation) according to the time of the middle image of the stack. Consequently we updated the tidal elevation for every stack. The maximum horizontal shift as a percentage of the distance between pixel and camera system can be found with the ratio TE/z_{cam} where TE is the vertical tidal excursion and z_{cam} is the vertical position of the camera system. For the case of PCA beach, the camera height is 70 m and the tide varies approximately 0.1 m during 8.5 min. Thus, a ratio of 0.14% is found to produce pixel shift inaccuracies in the horizontal plane. This means that when the camera viewfield reach a distance in the far end of the domain (around 900 m) the pixels move around 1.3 m back and forth within the ∼17 min duration of a stack. Therefore, we suspect that this deviation in accuracy due to pixel shifting is not sufficient to induce significant variations in depth after cBathy computations. However, vertical inaccuracies in bathymetry estimates can become significant if, for example, a longer video recording period is desired for a stack (>17 min) in an environment where tidal elevation varies rapidly such as the present field study.

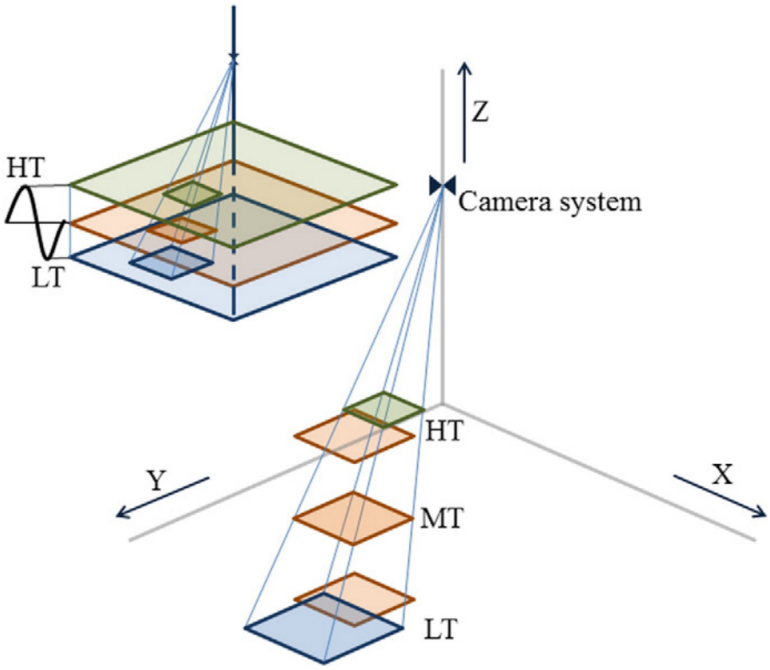

Figure 4.10 – The squares represent a selection of pixels moving up and down with the tidal elevation. The pixel set moves respectively towards the camera system and away from it. At the same time, relative contraction and expansion between pixels take place. Figure and caption extracted from Bergsma et al. (2016).

In any case, the spurious tide-dependent depth-modulation seems likely to be related with an inaccuracy on how the vertical fixed elevation is taken into account for the pixel to ground coordinate transformation (subsection 3.3.4.5). An absolute error in rectification (unreliability in the extrinsic and intrinsic parameters) obtaining the 11 transformation parameters can also lead to positioning errors. Therefore, these non-physical sources of errors will require further investigation.

The very upper part of the beach face is related with less accurate results as analysis tiles can contain partly wet/dry pixels at the sea-land interface mixing unuseful sub-aerial and acceptable subaqueous signals (Rutten et al., 2016). The systematic shallow water bias (overestimation of true depth) can also be explained by finite amplitude effects that increase wave celerity as waves shoal and break reducing the validity of the linear dispersion relationship (Bergsma and Almar, 2018; Brodie et al., 2018). Figure 4.11 illustrates an example of this case. Since the depth inversion estimation depends upon accurate estimates of frequency and wave number pairs, we selected a stack (under typical wave conditions at high tide) and compared the $f - k$ pairs, estimated from

cBathy, with the linear dispersion relationship relative to the spectrum at the specific depth and location given by the Aquadopp (AQ) current profiler installed within the reef (see AQ position in Figure 2.7). As shown in Figure 4.11, the cBathy-derived wave numbers according to the sea-swell frequency band are overall deviated from the linear dispersion relationship. The straight line for the wave numbers is indicative of non-linear interactions and that high-frequency components are bound or phase locked to the wave group. Indeed, bound high harmonics contribute to an increase in skewness and height of wave crests, which has for effect to enhance their propagation speed (Martins et al., 2021). Nevertheless, the overall mismatch between the cBathy-derived wave numbers and the analytical linear dispersion relationship is too large to be attributed solely to non-linear effects. As the cBathy computed wave numbers are smaller than the predicted linear theory, when inverted, large depth overestimation are produced, up to 70% than the real water depth as shown for the case of the shallow water AQ location, even though associated skill values (>0.5) indicate confident estimates. As mentioned before, this large discrepancy in depth may be due to rectification errors although it remains unclear.

The current cBathy version does not include the effects of currents and Doppler shifting in the dispersion relation (Eq. 4.1). For the case of PCA beach, persistent rip currents (e.g., near the headland) can potentially interact with incident (short-period) waves, shortening their wavelength (k increases) and thus underestimating local depth. However, with cBathy typical settings (Table 4.2), short-period waves and rapid cross-shore depth changes over the sample domain cannot be resolved, unless a denser pixel spacing is defined and more (higher) frequencies are accounted for analysis (thus requiring more computational effort) (Holman et al., 2013; Brodie et al., 2018). On the other hand, several studies have reported significant variation in cBathy performance with increasing wave height (Holman et al., 2013; Bergsma et al., 2016; Bouvier et al., 2020), since breaking waves are spread over a wider surf zone, obscuring the optical wave signal. Despite this issue, the quality assessment computed using Bouvier et al. (2020) approach, indicates the capability of cBathy to return depth estimates for more than 70% of the domain even under waves larger than 2 m. However, the fact that depth outputs (with a skill score > 0.5) are still retrieved even under large wave condi-

tions does not necessarily mean that they are correctly estimated, as previously shown in Figure 4.11.

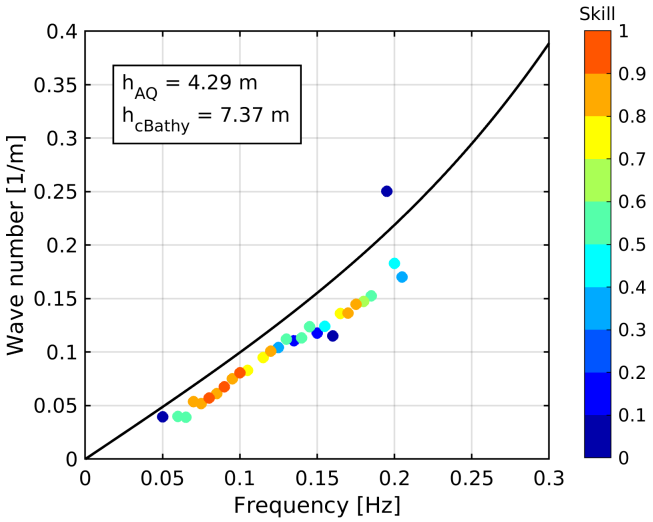

Figure 4.11 – Frequency and wave number pairs estimated from cBathy using a ∼17 min stack from 11 October 2018 at 07:00 GMT. Field conditions according to the sampled stack: Tide = 1.18 m (high tide); H_s = 1 m; T_p = 11.8 s; θ_p = 3.6° (respect to shore normal). The curve shows the linear dispersion relationship for the specified water depth (4.29 m) given by the Aquadopp (AQ) during the same time. The markers indicate the $f - k$ pairs estimated from cBathy at the Aquadopp grid position. The color of the markers is proportional to the skill used as a threshold quality control within cBathy code; $f - k$ pairs with a skill score below 0.5 are usually rejected for depth inversion.

4.11 Conclusions

Video-based depth inversion through the linear dispersion relationship for free surface waves using the cross spectral correlation analysis, cBathy (Holman et al., 2013) was applied consecutively for 3-weeks in a highly energetic macro-tidal environment. The comparison between surveys and cBathy estimates reveals an overall RMSE = 0.37 m and bias = 0.57 m for the beginning of the experiment (05/Oct/2018), and a RMSE = 0.29 m and bias = 0.56 m over the whole domain by the end of the experiment (24-26/Oct/2018). With exception of the rip channel formed by the end of the experiment, the morphological features are in approximately the right places but with a significant vertical offset (1−1.5 m) over the whole domain and enhanced at the shallowest parts (reef and beach shore face) where depth is consistently overestimated. Application of

cBathy revealed two main issues: 1) inaccurate depth estimations dependent on the tidal level and 2) less accurate depth estimates due to non-linear effects occurring in shallow water regions. The first issue is most probably related with a rectification inaccuracy and is currently under investigation. The second issue might be addressed by incorporating non-linearity into the phase speed which requires additional knowledge of the local wave height (Catálan and Haller, 2008). In conclusion, our results are in agreement with Brodie et al. (2018) findings (the only study considering waves bigger than 2 m), suggesting that bathymetric inversion should not be used to quantify morphological evolution during storms, but rather when conditions are calmer at the time of the rise or fall of each storm.

Chapter 5

Optically derived wave-filtered surface currents

Contents

5.1 Preamble

This chapter is based on the research article Rodríguez-Padilla et al. (2021) published in the Journal of *Remote Sensing*, available in open access: https://www.mdpi.com/1104840

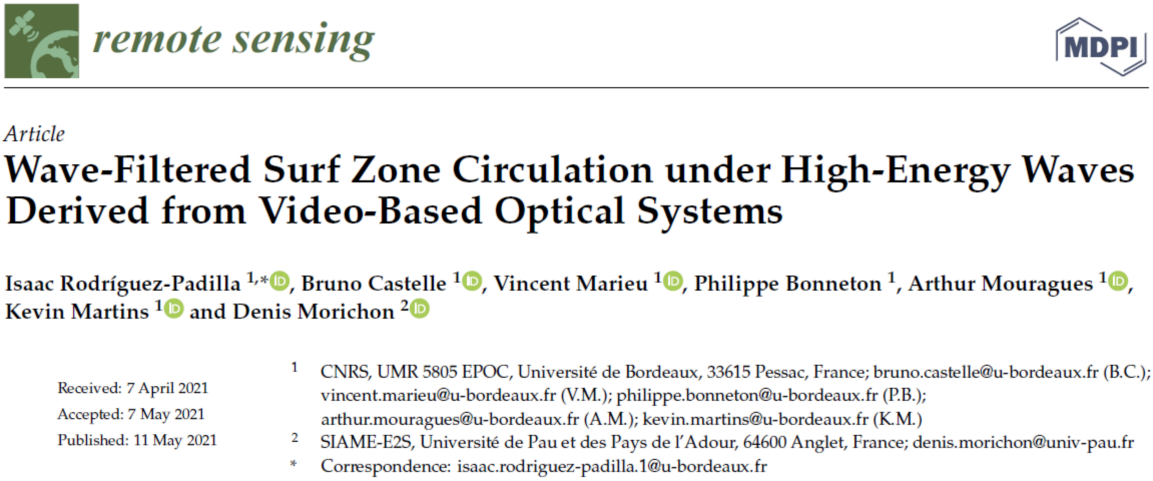

remote sensing

MDPI

Article

Wave-Filtered Surf Zone Circulation under High-Energy Waves Derived from Video-Based Optical Systems

Isaac Rodríguez-Padilla [1,*], Bruno Castelle [1], Vincent Marieu [1], Philippe Bonneton [1], Arthur Mouragues [1], Kevin Martins [1] and Denis Morichon [2]

Received: 7 April 2021
Accepted: 7 May 2021
Published: 11 May 2021

[1] CNRS, UMR 5805 EPOC, Université de Bordeaux, 33615 Pessac, France; bruno.castelle@u-bordeaux.fr (B.C.); vincent.marieu@u-bordeaux.fr (V.M.); philippe.bonneton@u-bordeaux.fr (P.B.); arthur.mouragues@u-bordeaux.fr (A.M.); kevin.martins@u-bordeaux.fr (K.M.)
[2] SIAME-E2S, Université de Pau et des Pays de l'Adour, 64600 Anglet, France; denis.morichon@univ-pau.fr
* Correspondence: isaac.rodriguez-padilla.1@u-bordeaux.fr

The work behind this paper comprises a year of my PhD searching for a methodology on how to estimate nearshore currents from consecutive video images. By the time we started this research, we knew that the optical signature was always there; foam left by breaking waves carried by the flow, as suggested by previous studies (e.g., Chickadel et al. 2003; Almar et al. 2016). The challenge with respect to previous studies was to find a method to track the two-dimensional foam displacement in the image plane without tracking the influence of the passing waves. For this purpose, we built on Dérian and Almar (2017) approach which consisted of tracking the foam trajectories using an optical flow algorithm. Through trial and error and a lot of testings, we found a way to filter out the wave signal from the image sequence in order to track the remnant foam supposedly advected by the underlying currents. Nevertheless, it is important to mention that during the period of writing this research article, Anderson et al. (2021) simultaneously published a very similar article, which delayed the publication of our manuscript as we had to restructure the content to put their work in context.

Before introducing the article, a brief recompilation of different methods to estimate surface velocities using remote sensing is provided.

5.2 Introduction

5.2.1 Surface currents estimation based on remote sensing techniques

The observation and monitoring of nearshore currents is an important task for coastal protection, erosion control, flood mitigation, marine operations and beach safety (Novi et al., 2020). However, direct measurements of currents in the nearshore are logistically challenging and expensive. Remote sensing of the current field is typically achieved using radar-based techniques (Streßer et al., 2017). Aircraft and satellite-based scatterometers, altimeters and synthetic aperture radars are able to scan large areas of the ocean, however, the coarse spatial resolution, infrequent sampling and interference by adjacent land areas limits the measurements to regions well seaward of the surf zone (Perkovic, 2008). On the other hand, ground-based radars such as high-frequency (HF) radars (3−30 MHz) and microwave (S-band: ∼3 GHz or X-band ∼10 GHz) marine radars have shown to be very useful to measure surface currents over coastal areas of different extension (Novi et al., 2020). HF systems reach larger offshore distances (1.5−200 km; "over the horizon") at lower spatial resolutions (0.25−3 km), which limits its utility inside the nearshore, whereas X-band systems achieve a smaller offshore range (2−5 km; "line-of-sight"), but with a significantly higher spatial resolution (5−10 m) sufficient to resolve the dominant surface wave motions.

HF radars measure ocean surface currents by calculating the Doppler shift of returning energy that is Bragg scattered from surface gravity waves (Paduan and Graber, 1997; Kaplan et al., 2005). The difference between expected and observed Doppler shift is used to calculate the radial surface current moving toward or away from the radar station. Therefore, at least two HF radar stations are needed to combine these radial currents to produce total surface current vectors.

For X-band radars, currents are estimated based on their Doppler shifting from the predicted dispersion relationship (Holman and Haller, 2013). As described by Young et al. (1985), a three-dimensional fast Fourier transform (3-D FFT) is applied to a series of spatial wave images to determine the three-dimensional spectrum $E(k_x, k_y, \omega)$. In the absence of a surface current the spectral energy in the three-dimensional wave number

frequency space is expected to lie on a shell defined by the dispersion relationship. Any deviation from the analytical dispersion relationship is attributed to a current shifting the wave frequency. Therefore, a least square curve fitting technique can be used to determine the surface current required to account for the observed Doppler shift (Streßer et al., 2017). The main limitation of this approach is that 3D-FFT methods maximize spectral information at the expense of spatial resolution (Honegger et al., 2020). Thus, the inherent limitation of spatial resolution make this method unsuitable for solving currents within the surf zone (Holman and Haller, 2013).

The use of video imagery to detect surface currents relies on tracking contrasting features that are assumed to move from frame to frame with the flow velocity (Anderson et al., 2021). In the surf zone, foam and bubbles generated by the breaking process create contrast with the ambient water and provides a means to observe currents by quantifying the passive advection of coherent features (Perkovic et al., 2009). However, optical images also sense light reflections from sloped water surfaces and turbidity that alters background color (Anderson et al., 2021). Thus, the challenge is to separate the foam that is carried only by the flow from wave-breaking rollers that propagate at wave celerity (Dérian and Almar, 2017).

A few studies were dedicated to the estimation of surface currents along one dimension using timestack approaches (Chickadel et al., 2003; Almar et al., 2016). The alongshore orientation allows to isolate the drifting foam motion and filter out breaking waves that appear as horizontal streaks in the timestack. To estimate two-dimensional surface velocities from optical imagery, most approaches rely on cross-correlation methods such as particle image velocimetry (PIV), borrowed from the fluid mechanics community (e.g., Adrian, 1991) or more recently on optical flow techniques, borrowed from the computer vision community (e.g., Horn and Schunck, 1981). Both methods have the capability to extract velocity vector fields from consecutive images and have been used to estimate surface currents in the swash and surf zone (Holland et al., 2001; Puleo et al., 2003; Perkovic et al., 2009; Wilson et al., 2014; Dérian and Almar, 2017; Anderson et al., 2021). However, none of the previous studies (with the exception of Anderson et al. 2021) have addressed an approach to remove the dominant optical clutter of incident waves from the image sequence to avoid capturing foam patterns

superimposed on propagating waves.

Therefore, in this contribution, we propose a new approach to filter the dominant optical signal associated with sea-swell waves from an image sequence. Moreover, we explore the potential of computing two-dimensional wave-filtered surface currents by tracking the residual drifting foam using an open-source optical flow algorithm.

5.3 Article: Wave-Filtered Surf Zone Circulation under High-Energy Waves Derived from Video-Based Optical Systems

5.3.1 Abstract

This paper examines the potential of an optical flow video-based technique to estimate wave-filtered surface currents in the nearshore where wave-breaking induced foam is present. This approach uses the drifting foam, left after the passage of breaking waves, as a quasi-passive tracer and tracks it to estimate the surface water flow. The optical signature associated with sea-swell waves is first removed from the image sequence to avoid capturing propagating waves instead of the desired foam motion. Waves are removed by applying a temporal Fourier low-pass filter to each pixel of the image. The low-pass filtered images are then fed into an optical flow algorithm to estimate the foam displacement and to produce mean velocity fields (i.e., wave-filtered surface currents). We use one week of consecutive 1-Hz sampled frames collected during daylight hours from a single fixed camera located at La Petite Chambre d'Amour beach (Anglet, SW France) under high-energy conditions with significant wave height ranging $0.8 - 3.3$ m. Optical flow-computed velocities are compared against time-averaged in situ measurements retrieved from one current profiler installed on a submerged reef. The computed circulation patterns are also compared against surf-zone drifter trajectories under different field conditions. Optical flow time-averaged velocities show a good agreement with current profiler measurements: coefficient of determination $(r^2) = 0.5 - 0.8$; root mean square error $(\mathrm{RMSE}) = 0.12 - 0.24$ m/s; mean error (bias) $= -0.09$ to -0.17

m/s; regression slope $= 1 \pm 0.15$; $\text{coherence}^2 = 0.4 - 0.6$. Despite an underestimation of offshore-directed velocities under persistent wave breaking across the reef, the optical flow was able to correctly reproduce the mean flow patterns depicted by drifter trajectories. Such patterns include rip-cell circulation, dominant onshore-directed surface flow and energetic longshore current. Our study suggests that open-source optical flow algorithms are a promising technique for coastal imaging applications, particularly under high-energy wave conditions when in situ instrument deployment can be challenging.

5.3.2 Introduction

Currents induced by wave breaking constitute the primary driving mechanism of sediment transport and morphological change in the nearshore (Castelle et al., 2006). Currents flowing along the shore (longshore currents) have the capacity to transport hundreds of thousands of cubic meters of sand per year, reshaping the underlying bathymetry and mobilizing nutrients, pollutants and biological species (Komar, 1998; Chickadel et al., 2003). Wave action in the breaker zone induces a net transport of water toward the shore, however, at certain locations along the coastline, the water returns seawards through relatively narrows zones as rip currents (Inman, 2002). Rip currents are concentrated fast-moving flows of water that extend from close to the shoreline through the surf zone, sometimes beyond the breaking region (Castelle et al., 2016b). These seaward-directed currents can pull swimmers offshore into deeper water making them the leading cause of fatal drowning and lifeguard rescues on beaches worldwide (Castelle et al., 2016a). Rip currents and associated surf-zone circulations are subject to tidal and wave group modulation as well as to local bathymetry variations making them highly variable in space and time, with flow pulsing within the infragravity (0.004 - 0.04 Hz) and very low frequency (VLF) band (<0.004 Hz) (MacMahan et al., 2006; Castelle et al., 2010a). In this context, characterizing the nearshore circulation system is crucial for efficient coastal infrastructure planning, reliable environmental assessment and appropriate beach safety strategy.

Traditional nearshore surf-zone velocity measurements are obtained by instruments deployed in situ collecting Eulerian or Lagrangian data. Examples of these instruments are electromagnetic current meters, acoustic sensors, and surface drifters (Rijn, 2007;

Inch, 2014). Although these measuring techniques are robust and accurate, they are usually limited to punctual measurements over short durations (Almar et al., 2016). Moreover, the deployment and periodic maintaining of the instruments require a significant amount of money, manpower and logistics resources (Streßer et al., 2017). Overall, collecting Eulerian and particularly Lagrangian data in high-energy beach environments is one of the greatest challenges (Castelle et al., 2016b). In order to overcome these limitations, remote sensing provides an attractive alternative.

Over the past decades, the use of low-cost shore-based video systems and more recently camera-equipped unmanned aerial vehicles (UAVs) have enabled access to high-resolution temporal and spatial data of the water surface layer (Holman et al., 2017; Splinter et al., 2018b; Andriolo et al., 2019). A few approaches based on optical remote sensing techniques have been developed to identify and characterize local surface currents associated with specific frequency bands. Dispersion relation fitting techniques (Young et al., 1985; Horstmann et al., 2017; Streßer et al., 2017) are one of such methods. Using the Doppler shifting of the surface gravity wave field, the surface velocity vector is estimated from the difference between observed wave phase velocity and that given by the linear dispersion relation (Horstmann et al., 2017). However, the use of the linear wave dispersion in the nearshore region is questionable since non-linear effects in wave hydrodynamics become significant (e.g., see Thornton and Guza, 1982). Moreover, the method requires a strong optical signature from the waves, which becomes problematic in the surf zone due to the presence of foam and broken waves.

Alternatively, the presence of foam have actually been exploited by optical tracking algorithms to estimate the surface flow velocity and the propagation speed of (broken) wave crests (Holland et al., 2001; Chickadel et al., 2003; Puleo et al., 2003; Almar et al., 2016; Dérian and Almar, 2017; Anderson et al., 2021). In the case of low wind, the remnant foam produced by breaking waves is assumed to act as a quasi-passive tracer being advected only by the underlying currents as long as the passing waves are removed. This assumption has been exploited to estimate mean longshore currents in the surf zone along a transect of pixels parallel to the shore (Chickadel et al., 2003; Almar et al., 2016).

For extraction of the two-dimensional velocity field, perhaps the most common and

well-documented video-based technique is particle image velocimetry (PIV) (Adrian, 1991; Thielicke and Stamhuis, 2014). This method essentially splits the image into several user-defined image segments or windows. The spatially-averaged displacement of a cluster of particles inside each window is computed over time using a cross-correlation approach. PIV-based techniques are typically performed in laboratory conditions using particle images (fluids containing reflective and neutrally buoyant tracer particles) to determine the velocity of the flow (Cox and Anderson, 2001; Kimmoun and Branger, 2007). Nevertheless, several studies have applied the PIV-based approach using shore-based and UAV video footage to estimate bore celerities and surface currents in the nearshore (surf zone and swash zone) (Puleo and Holland, 2000; Holland et al., 2001; Puleo et al., 2003; Perkovic et al., 2009; Wilson et al., 2014; Wilson and Berezhnoy, 2018; Chapman et al., 2019).

An alternative video-based technique that estimates the velocity field between consecutive images are optical flow algorithms (Horn and Schunck, 1981). Dérian and Almar (2017) presented a methodology based on an optical flow algorithm named "Typhoon" capable to estimate instantaneous nearshore surface currents from image sequences. More recently, Anderson et al. (2021) presented a new technique for processing surf-zone imagery called WAMFlow. Their approach consists of filtering the dominant optical clutter of incident waves from an image sequence by averaging frames over a sliding window in time with size of twice the dominant wave period. The resulting wave-averaged movie (WAM) contains residual foam features which are tracked using an optical flow algorithm to estimate the underlying mean flow motion inside the surf zone.

This paper builds on Anderson et al. (2021) similar wave-averaged approach. However, an alternative technique is proposed to remove the dominant wave optical signature present in the image sequence based on the use of a temporal Fourier low-pass filter. The present paper aims to compare for the first time optical flow-derived velocities against in situ velocity measurements from a fixed bottom-mounted Acoustic Doppler Current Profiler (ADCP). Optical flow estimates are also qualitatively compared with Lagrangian drifters deployed at the southern end of Anglet beach (Basque Coast, SW France) during an intensive field experiment carried out in October 2018 under

different wave, tide and wind conditions. Furthermore, this study provides some standard parameters for Liu (2017) MATLAB open-source optical flow program ("OpenOpticalFlow") so that anyone can reproduce and estimate wave-filtered surface velocity fields within the surf zone from consecutive images.

This paper is organized as follows. A brief introduction of the optical flow algorithm, as well as the physics-based equations, are detailed in section 5.3.3. The study site and the field experiment, including all available instruments, are described in section 5.3.4. The main processing steps before and after optical flow implementation are introduced in section 5.3.5. Results, performance and limitations of the optical flow method are presented in section 5.3.6 and further discussed in section 5.3.7 before conclusions are drawn in section 5.3.8.

5.3.3 Optical flow algorithm

Optical flow can be described as the apparent motion of individuals pixels (i.e., brightness patterns) between consecutive frames on the image plane (Horn and Schunck, 1981; Turaga et al., 2010). The present optical flow method is a differential approach based on a global formulation with a smoothness constraint which is capable to estimate the entire vector flow field simultaneously by solving a single equation (Dérian and Almar, 2017; Liu, 2017). The estimated pixel displacement and the known time interval between frames allow computing 2D velocity components within the entire image domain. The underlying assumption is that the image intensity from one frame to another remains invariant such that the time derivative of the image intensity can be accurately evaluated (Liu et al., 2012). This holds under the hypothesis that the pixel displacement is sufficiently small so that the pixel intensity remains constant (Horn and Schunck, 1981).

We used Liu (2017) MATLAB open-source optical flow program ("OpenOpticalFlow") to extract high-resolution velocity fields from an image sequence containing continuous patterns. The physical and mathematical foundations of Liu (2017) optical flow method are well established and have been validated for various fluid flow visualizations using laboratory, cloud and ocean images (Liu and Shen, 2008; Liu et al., 2012, 2015). The physics-based optical flow equation in image coordinates is given by:

$$\frac{\partial I}{\partial t} + \nabla \cdot (I\mathbf{u}) = f(x_1, x_2, I), \tag{5.1}$$

where I is the normalized image pixel intensity, $\mathbf{u} = (u_1, u_2)$ is the velocity vector with (x_1, x_2) coordinates in the image plane referred to as the optical flow and $f(x_1, x_2, I)$ is related to the boundary term and diffusion term. $\nabla\cdot$ is the divergence operator and $\nabla = \left(\frac{\partial}{\partial x_1}, \frac{\partial}{\partial x_2}\right)$ is the spatial gradient. Eq. 5.1 is a generic form of the projected-motion equations derived by Liu and Shen (2008) where the optical flow $\mathbf{u}$ is proportional to the path-averaged velocity of fluid or particles in flow visualizations. Eq. 5.1 is treated as an inverse problem since it is one equation with two unknowns (u_1, u_2). To determine the optical flow, a variational formulation with a first-order smoothness constraint is typically used (Horn and Schunck, 1981; Liu and Shen, 2008). Given I and f, we define a functional:

$$J(\mathbf{u}) = \int_\Omega \left[\frac{\partial I}{\partial t} + \nabla \cdot (I\mathbf{u}) - f\right]^2 dx_1 dx_2 + \lambda \int_\Omega \left(|\nabla u_1|^2 + |\nabla u_2|^2\right) dx_1 dx_2, \tag{5.2}$$

where λ is the Lagrange multiplier and Ω is the image domain. Minimization of the functional $J(\mathbf{u})$ leads to the Euler-Lagrange equation:

$$I\nabla\left[\frac{\partial I}{\partial t} + \nabla \cdot (I\mathbf{u}) - f\right] + \lambda\nabla^2\mathbf{u} = 0, \tag{5.3}$$

where $\nabla^2 = \left(\frac{\partial^2}{\partial x_1^2} + \frac{\partial^2}{\partial x_2^2}\right)$ is the Laplace operator and λ is the Lagrange multiplier that controls the smoothness of the field. In the special case where $\nabla\mathbf{u} = 0$ and $f = 0$, Eq. 5.1 reduces to the Horn and Schunck (1981) brightness constraint equation:

$$\frac{\partial I}{\partial t} + \mathbf{u} \cdot \nabla I = 0, \tag{5.4}$$

and further to the Euler-Lagrange equation originally given by Horn and Schunck (1981):

$$\left[\frac{\partial I}{\partial t} + \mathbf{u} \cdot \nabla I\right]\nabla I - \lambda\nabla^2\mathbf{u} = 0. \tag{5.5}$$

Eq. 5.3 and Eq. 5.5 are solved using the standard finite difference method with the Neumann condition $\frac{\partial \mathbf{u}}{\partial n} = 0$ on the image domain boundary $\partial\Omega$ (Liu and Shen, 2008; Wang et al., 2015). In computations, the solution of Eq. 5.5 is used as an initial approx-

imation for Eq. 5.3 for faster convergence. The subroutines inside OpenOpticalFlow (Liu, 2017) in charge of solving Eq. 5.5 and Eq. 5.3 are "horn_schunck_estimator.m" and "liu_shen_estimator.m", respectively. Further details on the mathematical development and error analysis of the optical flow method can be found in (Liu and Shen, 2008; Liu et al., 2015; Wang et al., 2015; Liu, 2017).

Liu (2017) OpenOpticalFlow program also includes additional subroutines for image pre-processing (e.g., Gaussian filter for local illumination correction and random noise removal) and a coarse-to-fine iterative scheme for improvement of the optical flow computation in case of large pixel displacements. A brief description of the relevant input parameters is presented in Appendix A and can be found in Liu (2017).

5.3.4 La Petite Chambre d'Amour beach experiment

5.3.4.1 Study site

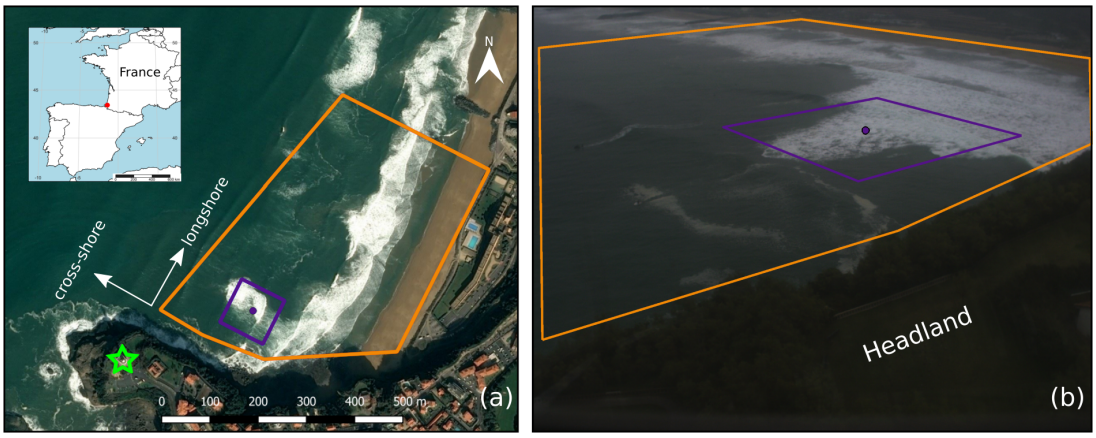

Figure 5.1 – (**a**) Study site of PCA beach, southwestern France. The green star indicates the location of the fixed camera system installed at the top of Biarritz lighthouse near the tip of the headland. (**b**) Example of a snapshot (oblique image) captured by the video monitoring system. The orange and purple polygons show the image-domains used for optical flow implementation. The orange domain corresponds to the drifter experiment area and the purple domain to the ADCP (purple dot) continuous recording within the submerged reef.

La Petite Chambre d'Amour (PCA) beach is the most southern stretch of the 4-km long sandy embayment of Anglet beach located on the Basque Coast, SW France (Figure 5.1). PCA beach is bounded by a prominent 500-m long rocky headland in the South and comprises a 90-m groin in the North. These two morphological characteris-

tics play an important role on the beach state and rip current location (Huguet et al., 2016). Close to the headland, a 20-m wide submerged rocky reef is present exerting persistent wave breaking and occasionally bathymetrically-controlled rips at low tide under low-energy waves (Mouragues et al., 2020b). The beach is composed of medium to coarse sand ($D_{50} \approx 2$ mm) and is classified as a high-energy intermediate beach with the presence of a double-bar (occasionally single-bar) system (Huguet et al., 2016). The relative steep beach face ($\tan\beta \approx 1/10$) favors the formation of beach cusps with shoreline dynamics strongly controlled by the geometry of the surf-zone sandbar (Birrien et al., 2013). The coast is predominantly exposed to Atlantic W-NW high-energy incoming swells with an average annual offshore significant wave height $H_s = 1.57$ m (up to 10 m during winter storms) and average peak wave period $T_p = 10$ s (Abadie et al., 2005). The tide is semi-diurnal characterized by a meso-macro tidal regime with an average range varying between 1.69 m (for neap tides) and 3.94 m (for spring tides) (Rodriguez-Padilla et al., 2020). Breaking waves are the dominant driver of nearshore currents, with tide elevation affecting breaking patterns and in turn modulating nearshore currents (Sous et al., 2020). As opposed to the northern Aquitaine open sandy beaches, PCA beach responds predominantly at individual storm frequency rather than at seasonal timescales (Huguet et al., 2016).

5.3.4.2 Field experiment

An intensive field campaign was performed at PCA beach from 3 to 26 October 2018 with the objective to investigate the nearshore current circulation and headland flows under a range of energetic wave conditions (Mouragues et al., 2020a). The 3-week field experiment involved a large display of instruments including four Acoustic Doppler Current Profilers (ADCPs), six surf-zone drifters and high-frequency video monitoring from a fixed video-camera and a camera-equipped UAV. In-situ directional wave and wind measurements were also continuously collected (every 30 min and 1 hr, respectively) by a permanent directional wave buoy located approximately 6 km offshore and by the Biarritz airport meteorological station (71 m altitude) located 3 km SE of the study site, respectively. Hourly water level measurements were retrieved from Saint-Jean-De-Luz tide gauge located 15 km SW of the study site. In the frame of the large-scale field exper-

iment described in Mouragues et al. (2020b), the present dataset gathers the data collected during the longest continuous fixed-camera video recording (08-15/Oct/2018) together with simultaneous Eulerian measurements collected from a single available ADCP installed over the submerged reef within the camera view field (Figure 5.1). The field conditions during this week are shown in Figure 5.2 and are described in the following subsection. In addition, the present study examines simultaneous video and drifter data during four days (on 18, 19, 22 and 23 October 2018) under different wave, wind and tide conditions (Table 5.1).

5.3.4.3 Field conditions and overall nearshore circulation

The 1-week (08-15/Oct/2018) continuous set of measurements used in this study (Figure 5.2) builds on the same experiment presented by Mouragues et al. (2020b). Overall, PCA beach was exposed to relatively energetic offshore wave conditions (average $H_s = 1.6$ m) with high-energy wave events ($H_s > 2$ m) with peak wave period T_p ranging from 7 to 15 s (Figure 5.2a,b). Offshore wave conditions also featured a wide range of wave angle of incidence ($-23 < \theta_p < 20°$; Figure 5.2c). The sign of the peak wave incidence θ_p (angle of wave incidence relative to the shore normal) indicates on which side of the headland waves were coming from. Wind conditions (Figure 5.2d,e) were relatively weak with mean wind speed values around 3 m/s coming primarily from the S-SE sector. A single moderate wind event was captured on 14 October 2018, reaching wind speed up to 12 m/s coming from the W-NW (roughly shore normal) direction. During the field experiment, PCA beach morphology corresponded to a low-tide terrace beach state (Wright and Short (1984) classification) with a mostly alongshore-uniform sandy bed that barely evolved throughout the experiment. The reader is referred to Mouragues et al. (2020a,b) for more information about PCA bathymetry details.

Mouragues et al. (2020b) classified wave-induced circulation patterns observed at PCA into three wave angle of incidence configurations. According to this classification, the 1-week dataset was identified as a deflection ($\theta_p > 0°$; 8-10/Oct/2018), shore-normal ($\theta_p = 0°$; 11/Oct/2018) and shadowed ($\theta_p < 0°$; 12-15/Oct/2018) configuration. During deflection configuration (8-10/Oct/2018), the ADCP captured longshore currents flowing toward the headland (Figure 5.2f). The seaward deflection of the

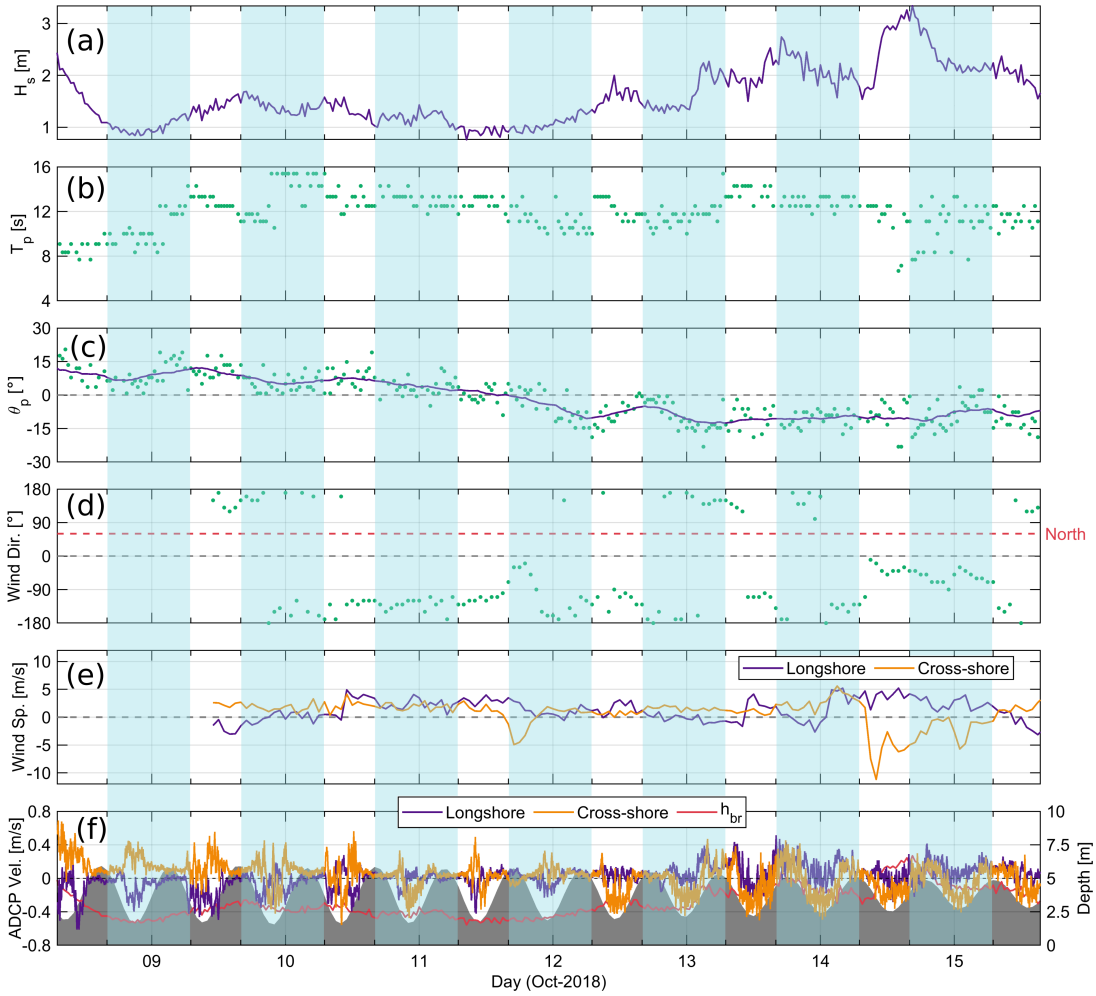

Figure 5.2 – Field conditions during the 1-week (08-15/Oct/2018) continuous ADCP recording. Offshore (**a**) significant wave height (H_s), (**b**) peak wave period (T_p) and (**c**) peak wave angle of incidence relative to the shore normal (θ_p; green dots) and its 12h-averaged values (purple line). (**d**) Wind direction; wind incidence relative to the shore normal (green dots). The red line shows the north direction with respect to the shore normal (60°). (**e**) Longshore (purple line) and cross-shore (orange line) wind speed components. (**f**) ADCP 5-min time-averaged surface longshore (purple line) and cross-shore (orange line) velocity components. Positive cross-shore (longshore) surface velocities values correspond to an offshore-directed (directed away from the headland) current (see Figure 5.1). The latter convention is the same for the wind speed components. The gray filled area represents the water depth time series at the ADCP location and the red line shows the temporal evolution of wave breaking water depth (h_{br}) defined as $h_{br} = H_s/0.5$. Non-shaded regions indicate video recording during daylight hours (blue shaded regions corresponds to nightlight hours). Field conditions during the drifter experiment are shown in Table 5.1, as drifters were deployed on 18, 19, 22 and 23 October 2018 outside of the 1-week ADCP recording period.

longshore current against the headland produced deflection rips with offshore surface velocities sporadically exceeding 0.4 m/s. On the single day of shore-normal configu-

ration (11/Oct/2018) the surface flow was characterized by cross-shore motions with surface velocities oscillating between -0.4 and 0.4 m/s. During the shadowed regime (12-15/Oct/2018) surface currents were primarily onshore directed flowing away from the headland driven by alongshore variations in wave breaking induced by the shadowing effect of the headland (Castelle et al., 2016b). Overall, surface currents were found to be strongly modulated by the tide, which coincided with a spring tide cycle with the water depth column varying from 1.5 to 5.9 m at the location of the ADCP (gray shaded region in Figure 5.2f). As opposed to open sandy beach embayments, PCA beach inherited geological features (headland and submerged reef) exert a strong control on nearshore circulation. A close inspection of the time evolution of wave breaking water depth, defined as $h_{br} = H_s/0.5$ for PCA field site, indicates that the ADCP is within the outer edge of the surf zone only around low tide for $H_s < 2$ m (red line in Figure 5.2f). Therefore, the submerged reef (where the ADCP is installed) is assumed to play a major control in flow dynamics as waves start to break over the reef when water depth decreases.

In the frame of the drifter experiment described in Mouragues et al. (2020b), four days of drifter deployments were selected to analyze PCA beach main circulation patterns under different oblique wave configurations with varying wave, wind and tide conditions (Table 5.1). In particular, during the rising neap low tide on 23 October 2018, a deflection rip was found to systematically advect drifters from the surf zone to at least 1,000 m offshore. The spatial structure of the rip consisted of an approximately 150-m wide rip neck along the headland with a wider rip head extending further offshore the headland. Lagrangian and Eulerian measurements registered mean surface velocities around 0.3 m/s in the rip neck and 0.35 m/s in the rip head along with VLF rip pulsations with characteristic periods around 30 and 50 min (Mouragues et al., 2020b; Sous et al., 2020).

Table 5.1 – Field conditions during the four days of drifter deployments. Offshore peak wave angle of incidence (θ_p) and wind direction incidence are relative to the shore normal.

	18/Oct/2018	**19/Oct/2018**	**22/Oct/2018**	**23/Oct/2018**	
Time [GMT]	11:52 to 13:57	07:26 to 10:28	07:42 to 10:34	08:02 to 08:35	08:36 to 11:38
Configuration	Shore-normal	Shadowed	Shore-normal	Deflection	Deflection
Drifter Deployments	16	28	46	5	30
H_s **[m]**	1.9	1.6	1	1.7	1.6
T_p **[s]**	14	13	11	13	11
θ_p **[°]**	0	-5	0	4	8
Wind Speed [m/s]	2.4	1.1	3.6	0.6	1.7
Wind Direction [°]	10	-50	30	-180	140
Tide Stage	Ebb	Flood	Flood	Ebb	Flood
Water Level Range [m]	0.66 to 0.08	-0.42 to 0.58	-1.49 to -0.46	-1.70 to -1.74	-1.75 to -0.13

5.3.4.4 Video data

High-frequency sampled images (1 Hz) recorded at 1624x1234 px were collected from a single permanent camera video station installed on the top of Biarritz lighthouse (70 m above mean sea level) located near the tip of the headland (green star in Figure 5.1). The resulting oblique images covered part of PCA near the headland, including the submerged reef and the surf zone. Unfortunately, only one of the four ADCPs deployed during the experiment was within the camera view field. In order to compare optical flow derived velocities against in-situ instruments, one week of continuous daylight video recording corresponding to simultaneous ADCP measurements were selected from 08/Oct/2018−07:00:00 to 15/Oct/2018−15:30:00 GMT. Moreover, Lagrangian measurements together with simultaneous video data were used to provide a spatial insight of the surface flow. Drifter trajectories were captured by the video system on four different days. Between 2 and 3.5-h burst of images were selected from each day of drifter deployment for further post-processing and analysis.

5.3.4.5 ADCP data

A single ADCP (Nortek Aquadopp Profiler 2 MHz) was deployed within the fixed camera view field approximately 280 m away from the video station (Figure 5.1). This ADCP

was used to retrieve current measurements to further validate optical flow surface velocities. The ADCP was mounted horizontally on an AquaCross aluminum frame (Figure 5.3) near the bottom of the submerged rocky reef between 1.5-5.9 m depth (depending on the tide elevation). 1-Hz continuous measurements of pressure and velocities along the water column were collected during 1 week (8-15 October 2018) for optical flow comparison. The pressure sensor was located 0.2 m above the seabed (δ_s). The velocity profile was measured over vertical cells (z_{cell}) of 0.1 m size (δ_c = cell size) after a blanking distance (δ_b) of 0.1 m from the instrument. Velocity measurements were assigned to the center of each cell starting with the bottom cell at 0.35 m ($z_{cell_1} = \delta_s + \delta_b + \delta_c/2$; Figure 5.3) above the sand bed.

Direct comparison of remotely sensed currents with fixed in situ instruments is not a trivial task (Dérian and Almar, 2017; Anderson et al., 2021). Video-derived velocities are extracted from the time-varying water surface layer which is locally influenced by instantaneous wave and wind conditions. On the other hand, conventional ADCPs typically discard data from the upper region of the water column leading to an inevitable spatial mismatch for a true velocity comparison. Upper cells emerge intermittently at the passage of a wave trough restricting the analysis within the water column below this elevation (Sous et al., 2020). To overcome this limitation, we make use of the concept of σ-layers which will be described below.

According to the shallowness parameter μ, the water surface at the location of the ADCP was characterized by weakly dispersive waves propagating in shallow waters ($\mu \approx 0.12$). The shallowness parameter μ is defined as:

$$\mu = (h_0 k)^2 , \tag{5.6}$$

where h_0 is the mean water depth and k the typical wave number ($k \approx 0.08$ 1/m). The pressure was used to reconstruct the water surface elevation using Bonneton et al. (2018) non-linear shallow water reconstruction formula, valid for weakly dispersive waves propagating in the shoaling and surf zone (see (Mouragues et al., 2019; Martins et al., 2020)):

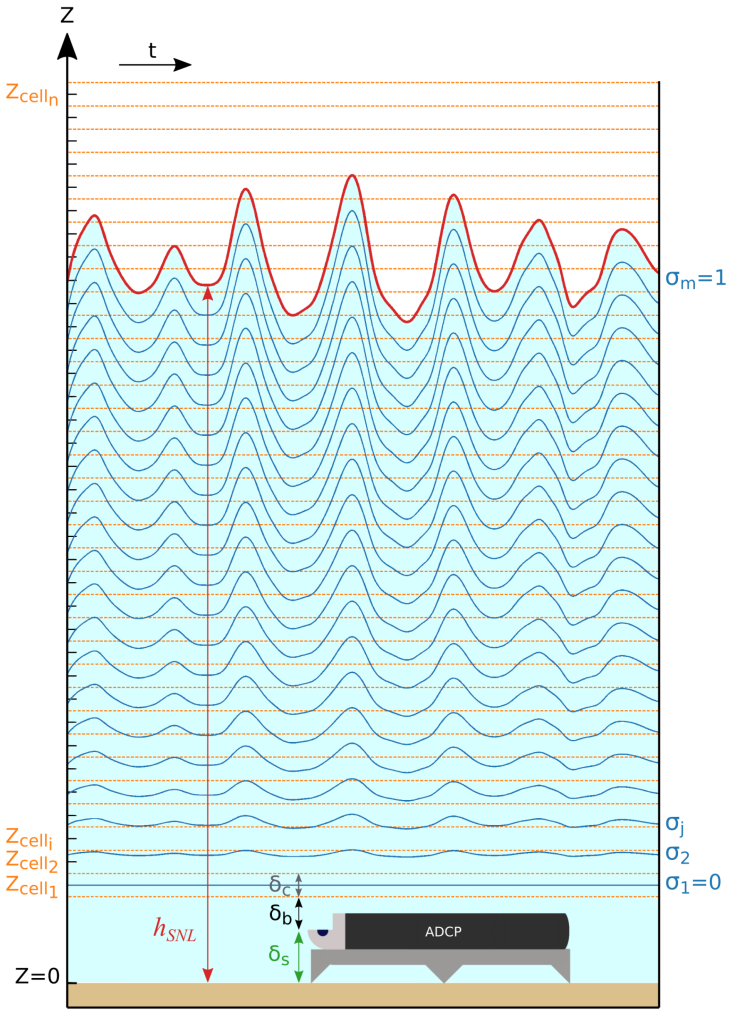

Figure 5.3 – Sketch showing the ADCP velocity measuring positions throughout the water column in terms of vertical cells (z_{cell}) and σ layers. The red line (h_{SNL}) represents the reconstructed water depth time evolution. δ_s indicates the pressure sensor height (green line) with respect to the bottom. The velocity profile is measured after a blanking distance (δ_b; black line) from the instrument. The measurements are assigned to the middle of each cell (δ_c= cell size) delimited by the orange dashed lines. The blue lines represent the user-defined σ layers normalized by the distance between the first cell and the water surface. σ layers are designed to follow the irregular shape of the water surface at different elevations of the water column. Velocities measurements at these positions are obtained by interpolating the vertical cells' velocity profile.

$$\zeta_H = \frac{P_s - P_{atm}}{\rho g} - h_0 + \delta_s, \tag{5.7}$$

$$\zeta_{SL} = \zeta_H - \frac{h_0}{2g}\left(1 - \left(\frac{\delta_s}{h_0}\right)^2\right)\frac{\partial^2 \zeta_H}{\partial t^2}, \tag{5.8}$$

$$\zeta_{SNL} = \zeta_{SL} - \frac{1}{g}\left(\frac{\partial}{\partial t}\left(\zeta_{SL}\frac{\partial \zeta_{SL}}{\partial t}\right) - \left(\frac{\delta_s}{h_0}\right)^2\left(\frac{\partial \zeta_{SL}}{\partial t}\right)^2\right), \tag{5.9}$$

where ζ_H is the hydrostatic reconstruction, ζ_{SL} the linear shallow water reconstruction, ζ_{SNL} the non-linear shallow water reconstruction above the mean water level, $\frac{\partial^2}{\partial t^2}$ the second-order time derivative, ρ the water density, g the gravity, P_s the pressure measured at distance δ_s above the bottom and P_{atm} the (constant) atmospheric pressure. The reconstructed water depth is defined as:

$$h_{SNL} = h_0 + \zeta_{SNL}. \tag{5.10}$$

For this study, the mean water depth h_0 and the reconstructed water surface ζ_{SNL} were computed consecutively over ~17-min segments throughout the whole time series. ADCP cells above the reconstructed water surface were discarded from the analysis and submerged cells were depth-normalized. ADCP horizontal velocities along the water column were transformed to a vertical σ coordinate system in order to measure the velocities close to the water surface consistent with video-camera derived optical flow estimation (see Figure 5.3). In addition, ADCP depth-averaged velocities were also computed for comparison with optical flow estimates. The σ coordinate system is expressed by a user-defined number of vertical layers m, hereafter referred to as σ-layers. Each σ-layer j is normalized by the distance between the first ADCP cell and the instantaneous water surface elevation:

$$\sigma_j = \frac{(j-1)\,\Delta z - z_{cell_1}}{h_{SNL} - z_{cell_1}}; \quad j = 1, 2, 3, ..., m; \quad \Delta z = \frac{h_{SNL} - z_{cell_1}}{m-1}. \tag{5.11}$$

The first sigma layer (σ_1) corresponding to the near-bottom is equal to zero and the last sigma layer corresponding to the water surface (σ_m) is equal to one. ADCP vertical cells z_{cell_i} are interpolated to each σ-layer σ_j before normalization. Regardless of the water depth, σ-layers are constrained to be equally divided along the water column so their individual value in terms of sigma (between 0 and 1) remains constant, whereas the thickness between σ-layers (Δz) in terms of meters is varying at each time step. σ-layers coincide with the irregular water wave surface within the water column and allow the calculation of residual velocity around the mean water surface level (Giddings

et al., 2014; Cheng, 2020). For the present study, 21 σ-layers were defined where each layer corresponded to 5% of the instantaneous water column. Moreover, the three σ-layers closest to the water surface were averaged (σ_{19}, σ_{20} and σ_{21}) and are hereafter referred to as the ADCP surface velocity measurements. Similarly, all the 21 σ-layers were averaged and are hereafter referred to as the ADCP depth-averaged velocity measurements.

5.3.4.6 Drifter data

Six GPS-tracked surf-zone drifters were released multiple times on four different days (on 18, 19, 22 and 23 October 2018) with the purpose of providing greater spatial coverage of rip cell circulation. Deployments lasted from 2 to 3.5 h (Table 5.1). Drifters were individually seeded over the submerged reef region using a jet ski or by swimmers under reasonably safe conditions. Drifters' positions logged at 2.5 Hz were locally stored on an SD card and transmitted in real-time to a shore station for visualization and retrieving strategy. The drifters were of a robust PVC design modified from that of Schmidt et al. (2003) consisting of a subaerial mast containing the GPS antenna and a submerged dampener (circular bottom plate) with external fins to reduce surfing effects and vertical motions (MacMahan et al., 2009). Drifters were provided by CMAR (Coastal Marine Applied Research, coastal consultancy at the University of Plymouth) which have been previously tested for the measurement of surf-zone flows (Austin et al., 2013; McCarroll et al., 2014; Scott et al., 2016). According to Mouragues et al. (2020b), drifter position and velocity uncertainties were estimated to be less than 3 m and approximately 0.1 m/s, respectively, with a maximum windage error of 0.1 m/s due to the effects of wind slippage (Murray, 1975) during drifter deployment.

5.3.5 Video processing

5.3.5.1 Image pre-processing

Following Rodriguez-Padilla et al. (2020), oblique images were first converted to grayscale, then stabilized and further geo-rectified through a photogrammetric transformation (Hartley and Zisserman, 2004) into a longshore/cross-shore local reference

frame with 1x1 m grid resolution. A direct linear transformation (Abdel-Aziz and Karara, 1971) was used to generate the plan-view images considering 16 spatially distributed surveyed ground control points (GCPs) on both land and water. To avoid tide-related inaccuracies in image rectification (Bergsma et al., 2016), each image was rectified onto a grid that was updated every 1-min in the vertical coordinate using interpolated water elevation measurements from a tide gauge located 15 km SW of the study site. The intrinsic parameters of the camera (e.g., image center coordinates, effective focal length and scale factors) were also taken into account to remove nonlinear effects such as radial distortion in the images (Holland et al., 1997). Two different sub-image domains were selected to reduce computational time when applying the optical flow algorithm: a 100x100 m square domain centered at the ADCP image location for the 1-week continuous surface currents measurements (purple polygon in Figure 5.1) and a 600x500 m domain for the drifter deployments (orange polygon in Figure 5.1).

The approach of the present study is to use the drifting foam, left after the passage of breaking waves, as a quasi-passive tracer and track it to estimate the water surface flow. When using optical flow over consecutive images, the main challenge is to avoid capturing the foam (or any water pixel parcel) moving at wave celerity. As shown in Figure 5.4, the visible sea-swell wave signature can be removed by applying a temporal Fourier low-pass filter on a pixel-by-pixel basis to the whole image sequence. This is an accurate alternative to remove waves in the frequency domain instead of applying a moving-average over consecutive frames as proposed by Anderson et al. (2021). Figure 5.4a shows a raw rectified frame containing readily visible alongshore patterns of propagating waves while Figure 5.4b shows the same frame after wave-filtering all pixels over time using a low-pass filter with cutoff-frequency f_c of 1/20 Hz. Figure 5.4c presents the pixel intensity power spectral density (PSD) computed at the image location of the ADCP (purple and orange dot) using raw and low-pass filtered images. The PSD computed from the raw image time series (purple line) contains the swell and wind sea wave signal centered at frequencies around 1/13.4 Hz and 1/6.6 Hz, respectively. This is in agreement with the average offshore peak wave period ($T_p = 12$ s) previously shown in Figure 5.2b. The low-pass filter cutoff-frequency f_c should be selected preferably below the lowest peak wave frequency f_p of the entire record,

to ensure that no wave-train is leaked into the image sequence and tracked by the optical flow algorithm. However, it is important to note that the selection of the cutoff-frequency f_c also regulates the degree of image smoothing. Maintaining a sufficient amount of texture (i.e., pixel intensity variations) in the image allows the optical flow algorithm to track fine-scale foam patterns. Thus, a trade-off between separating the optical wave signal and keeping the texture from the image should be considered. During the field experiment, the lowest peak wave frequency registered by the offshore buoy was $f_p = 1/15$ Hz (see Figure 5.2b). For this study, raw images were low-pass filtered using two different cutoff-frequencies: $f_c = 1/20$ Hz (as shown in Figure 5.4b,c) and $f_c = 1/60$ Hz. These two different set of low-pass filtered image sequences will be used as input for the optical flow algorithm to estimate two independent set of wave-filtered surface currents hereafter referred to as OF ($f_c = 1/20$ Hz) and OF ($f_c = 1/60$ Hz). Confronting the optical flow estimates using two sets of cutoff frequency will help understand the effect of the selection of f_c on the results.

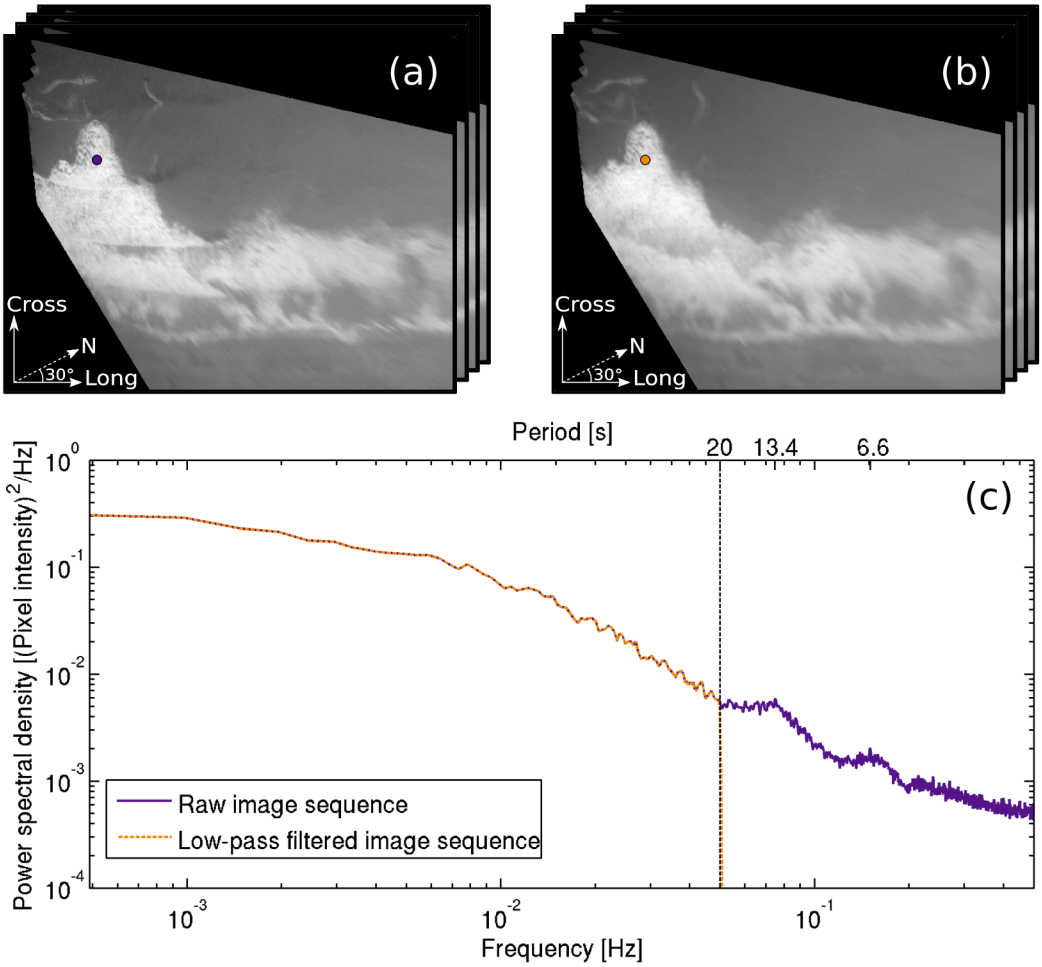

Figure 5.4 – Surface gravity waves removal from images. (**a**) Raw rectified image sequence containing visible waves; (**b**) rectified image sequence after wave-filtering. (**c**) Pixel intensity power spectral density (PSD) computed at the image location of the ADCP (purple and orange dot). The PSD is computed from the raw image time series (purple line) and the low-pass filtered image sequence (orange dashed line). The black dashed line corresponds to the cutoff frequency (1/20 Hz) of the low-pass filter previously applied to the raw image sequence.

5.3.5.2 Implementation and assessment

The optical flow algorithm was applied consecutively to more than 257,000 frames (71.5 h) in an area of 100x100 m at an image resolution of 1 m/px. The optical flow estimated surface velocities were spatially interpolated to the ADCP image location and compared against the instrument upper layer σ-velocities (average between σ_{19}, σ_{20} and σ_{21}) and depth-averaged velocities. Surface velocity time series and PSDs were computed from both, optical flow estimates and ADCP measurements for a qualitative comparison. Optical flow and ADCP velocity values corresponding to the time when the

ADCP was outside the surf zone ($h_{ADCP} > h_{br}$) were identified and excluded from the analysis to ensure the presence of foam and reduce optical flow near-zero velocities. Consequently, the 1-week daylight dataset was reduced by 53% of the original dataset to approximately 137,000 images (38 h). The PSDs of 1-week surface velocity time series were computed using Welch's method with 17 Hann-windowed non-overlapping records of 2 hours (approximately two segments per day). Similarly, the squared-coherence between ADCP and optical flow-derived velocities was estimated from the corresponding 1-week surface velocity time series using the same procedure. This resulted in each spectral estimate having 34 degrees of freedom and a spectral resolution of 0.00014 Hz.

5-min time-averaged optical flow and ADCP velocities associated with different ranges of significant wave height H_s were compared in order to assess the optical flow performance under different wave height conditions. Moreover, optical flow and ADCP velocities were averaged over a sliding window in time in order to reduce random noise. Different window sizes, ranging from 1 to 30 min, were selected for the moving average computation. For each window size selected, the resulting estimated and measured time-averaged velocities were quantitatively compared. Performance statistics, comprising the coefficient of determination (r^2), the root mean square error (RMSE), the mean error (bias) and the linear regression slope were computed to assess the optical flow ability to reproduce in situ measurements.

5.3.6 Results

5.3.6.1 1-week continuous surface currents measurements (08-15/Oct/2018)

Figure 5.5 shows the 5-min time-averaged surface velocity components time series corresponding to 1-week of daylight measurements. For the longshore surface velocity component (Figure 5.5a), the optical flow derived-velocities recreate fairly well the slow fluctuations found in ADCP surface measurements. However, northward-directed currents (positive longshore velocity values) appear to be slightly underestimated. Regarding the cross-shore component (Figure 5.5b), onshore-directed currents overall match well between optical flow and ADCP, while offshore-directed velocities are less in agree-

ment. This underestimation will be discussed in section 5.3.7. In general, the optical flow velocities obtained using low-pass filtered images with $f_c = 1/20$ Hz and $f_c = 1/60$ Hz are similar in pattern. However, OF ($f_c = 1/60$ Hz) present a smaller amplitude (i.e., smaller velocities values) with respect to OF ($f_c = 1/20$ Hz). It is important to note that near-zero optical flow values correspond to the time of high tide water elevation with $H_s < 2$ m when no wave breaking was present over the reef and no foam was available for tracking close to the ADCP location (see Figure 5.2f; blue shaded regions in Figure 5.5).

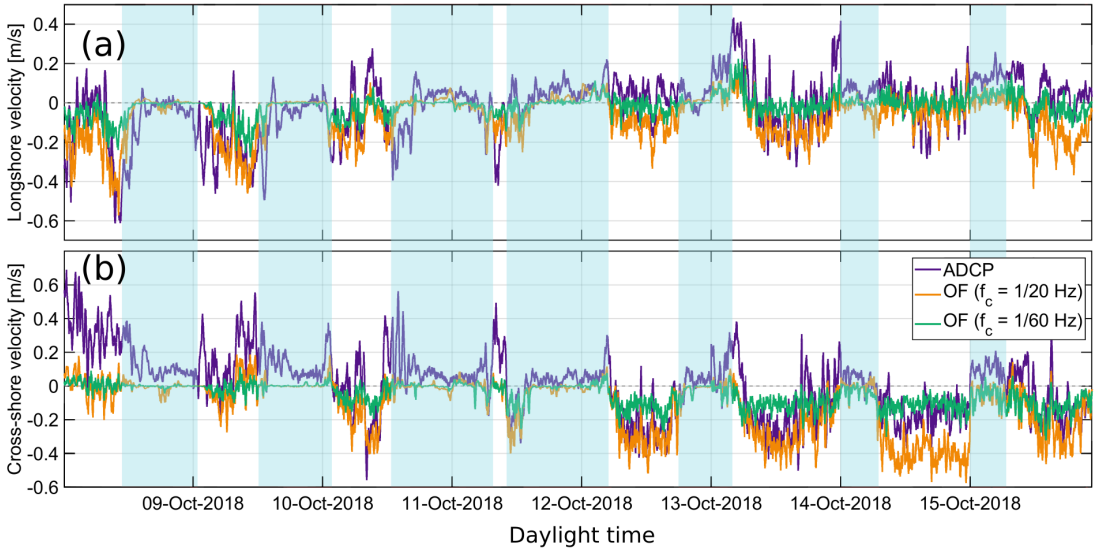

Figure 5.5 – Five minute time-averaged (**a**) longshore and (**b**) cross-shore surface velocity components time series from 8 to 15 October 2018. ADCP surface velocity measurements (average between σ_{19}, σ_{20} and σ_{21}) are displayed with a purple line. Optical flow velocity estimates computed from low-pass filtered images with $f_c = 1/20$ Hz and $f_c = 1/60$ Hz are shown with an orange and a green line, respectively. Positive cross-shore (longshore) surface velocities values correspond to an offshore-directed (directed away from the headland) current. Non-shaded (blue shaded) regions indicate the time when the ADCP is located inside (outside) the surf zone. For better visualization, surface velocities are concatenated in time to avoid gaps during nightlight hours.

Figure 5.6 shows the 5-min time-averaged ADCP and optical flow surface velocity components of Figure 5.5 as a comparison under different ranges of significant wave height H_s. Surface velocities were grouped into seven H_s bins of 0.5-m size. The corresponding statistics for each bin are summarized in Table 5.2 and 5.3 and depicted with histograms of different colors in Figure 5.6. Around 80% of the velocity data is concentrated between 1 and 2.5 m of H_s. OF ($f_c = 1/20$ Hz) and ADCP surface velocities within this range show a relatively good agreement ($r^2 \approx 0.5$ and $\mathrm{RMSE} \approx 0.2$ m/s). However, the bias and the skewed bivariate histograms indicate a northward- and offshore-directed current underestimation that becomes more evident for $H_s > 2.5$ m ($\mathrm{bias} \approx 0.2$ m/s).

Comparison between OF ($f_c = 1/60$ Hz) and ADCP surface velocities shows a smaller bias and less dispersion of the data with respect to OF ($f_c = 1/20$ Hz). Although r^2 suggests a similar linear agreement ($r^2 \approx 0.5$), optical flow velocities are overall smeared as shown in the histograms of Figure 5.6c,d. This is also evidenced by the steeper values of the regression slope ($\mathrm{slope} > 2$).

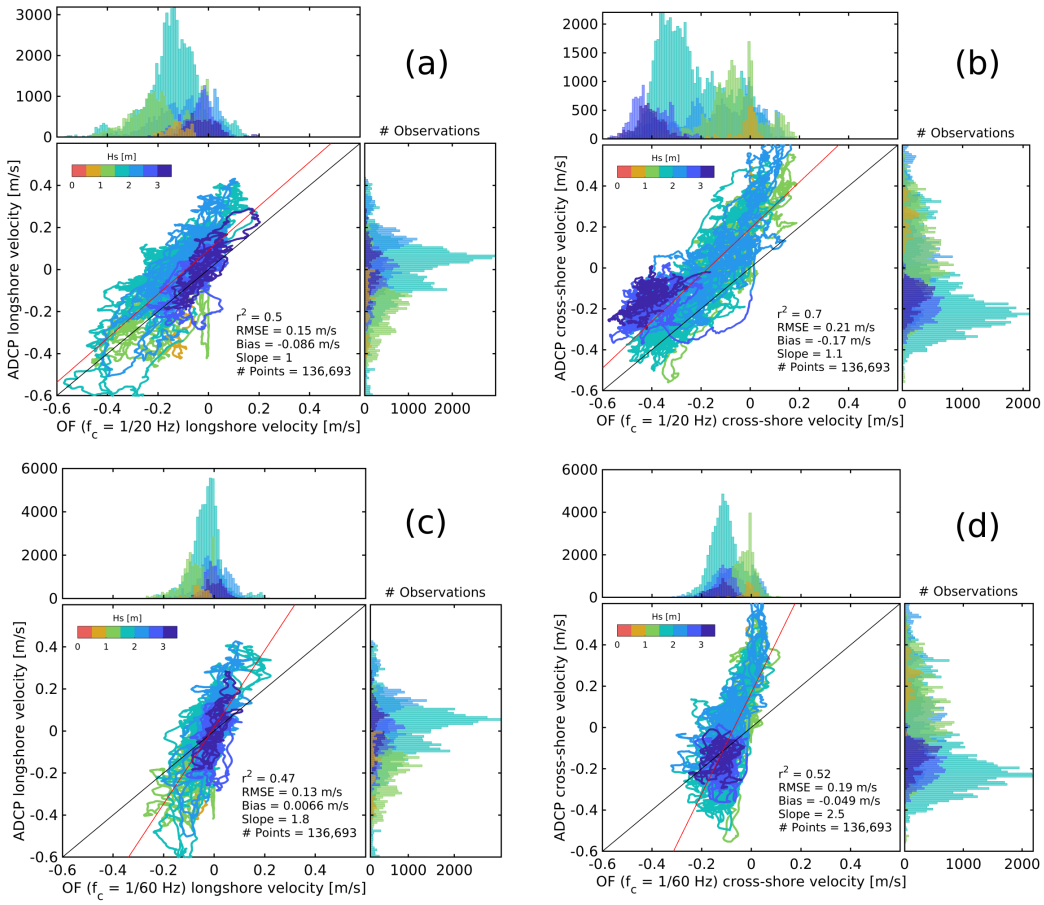

Figure 5.6 – Five minute time-averaged ADCP vs. optical flow surface velocity components from 8 to 15 October 2018 under different wave height conditions during low tide when the ADCP is located inside the surf zone. ADCP surface velocity measurements (average between σ_{19}, σ_{20} and σ_{21}) are compared against optical flow velocity estimates computed from low-pass filtered images with (**a-b**) $f_c = 1/20$ Hz and (**c-d**) $f_c = 1/60$ Hz. The colors denote the velocities associated with different ranges of offshore significant wave height H_s. The red line indicates the linear regression and the black line the 1:1 perfect match. Positive cross-shore (longshore) surface velocities values correspond to an offshore-directed (directed away from the headland) current.

Figure 5.7 quantifies the agreement between optical flow surface velocity estimates and ADCP measurements. ADCP measurements consisted of surface velocities (average between σ_{19}, σ_{20} and σ_{21}) and depth-averaged velocities (average of all σ-layers within the water column). The estimated and measured time series were moving-averaged and compared against different window size selections. Based only on r^2, the longshore surface velocity component (Figure 5.7a) is better reproduced by the optical flow when using low-pass filtered images with $f_c = 1/60$ Hz as input. Comparison between OF ($f_c = 1/60$ Hz) and ADCP surface velocities, for a window size larger than 10 min,

Table 5.2 – Five minute time-averaged ADCP vs. optical flow surface velocity components from 8 to 15 October 2018 under different ranges of offshore significant wave height H_s during low tide when the ADCP is located inside the surf zone. Optical flow velocities are computed from low-pass filtered images with $f_c = 1/20$ Hz.

ADCP vs. OF ($f_c = 1/20$ Hz)	**r^2**		**RMSE [m/s]**		**Bias [m/s]**		**Slope**		**# Points (%)**	
Velocity component	Long.	Cross.	Long.	Cross.	Long.	Cross.	Long.	Cross.	Long.	Cross.
$H_s < 0.5$ m	-	-	-	-	-	-	-	-	0 (0%)	
$0.5 \leq H_s < 1$ m	0.02	0.49	0.14	0.27	0.06	-0.26	0.45	1.52	3482 (3%)	
$1 \leq H_s < 1.5$ m	0.31	0.69	0.12	0.19	-0.01	-0.16	0.69	1.38	26879 (20%)	
$1.5 \leq H_s < 2$ m	0.63	0.74	0.16	0.17	-0.13	-0.13	1.16	1.35	60416 (44%)	
$2 \leq H_s < 2.5$ m	0.67	0.68	0.16	0.24	-0.13	-0.20	1.28	1.24	25920 (19%)	
$2.5 \leq H_s < 3$ m	0.41	0.13	0.08	0.23	-0.01	-0.21	1.02	0.33	12658 (9%)	
$H_s \geq 3$ m	0.69	0.59	0.07	0.27	-0.03	-0.27	1.29	0.59	7338 (5%)	
$H_s \geq 0$ m	0.50	0.70	0.15	0.21	-0.09	-0.17	1.00	1.13	136693 (100%)	

Table 5.3 – Five minute time-averaged ADCP vs. optical flow surface velocity components from 8 to 15 October 2018 under different ranges of offshore significant wave height H_s during low tide when the ADCP is located inside the surf zone. Optical flow velocities are computed from low-pass filtered images with $f_c = 1/60$ Hz.

ADCP vs. OF ($f_c = 1/60$ Hz)	**r^2**		**RMSE [m/s]**		**Bias [m/s]**		**Slope**		**# Points (%)**	
Velocity component	Long.	Cross.	Long.	Cross.	Long.	Cross.	Long.	Cross.	Long.	Cross.
$H_s < 0.5$ m	-	-	-	-	-	-	-	-	0 (0%)	
$0.5 \leq H_s < 1$ m	0.07	0.38	0.18	0.27	0.13	-0.26	1.15	1.72	3482 (3%)	
$1 \leq H_s < 1.5$ m	0.35	0.44	0.15	0.20	0.09	-0.12	1.37	2.93	26879 (20%)	
$1.5 \leq H_s < 2$ m	0.45	0.48	0.13	0.18	-0.02	0	1.73	2.35	60416 (44%)	
$2 \leq H_s < 2.5$ m	0.52	0.61	0.14	0.24	-0.05	-0.16	2.00	2.33	25920 (19%)	
$2.5 \leq H_s < 3$ m	0.06	0.01	0.10	0.11	0.03	0.08	0.72	0.20	12658 (9%)	
$H_s \geq 3$ m	0.58	0.02	0.08	0.07	-0.01	0.02	2.17	0.21	7338 (5%)	
$H_s \geq 0$ m	0.47	0.52	0.13	0.19	0.01	-0.05	1.82	2.45	136693 (100%)	

show r^2 values ranging from 0.55 up to 0.65 with associated RMSE between 0.12 and 0.11 m/s. Similarly, OF ($f_c = 1/60$ Hz) vs. ADCP depth-averaged velocities exhibit r^2 ranging from 0.5 up to 0.6 with lower RMSE between 0.10 and 0.08 m/s. A fair performance is still found when using low-pass filtered images with $f_c = 1/20$ Hz. OF ($f_c = 1/20$ Hz) vs. ADCP longshore velocity measurements (surface and depth-averaged velocities) show a consistent agreement ($r^2 = 0.5$) for any window size larger than 5 min, although RMSE values are relatively lower when compared against ADCP depth-averaged velocities (RMSE between 0.12 and 0.13) than with surface velocities (RMSE between 0.13 and 0.14). By contrast, ADCP cross-shore surface and depth-averaged velocities are better correlated with OF ($f_c = 1/20$ Hz) than with OF ($f_c = 1/60$ Hz) velocity estimates. For a window size larger than 5 min, r^2 values vary between 0.7-0.8 and 0.5-0.7, respectively (Figure 5.7b). OF ($f_c = 1/20$ Hz) vs. ADCP cross-shore

velocity RMSE decreases from 0.21 to 0.19 m/s as the window size increases from 5 to 30 min regardless if the optical flow estimates are compared against surface or depth-averaged ADCP velocities. On the other hand, as the window size increases from 5 to 30 min, OF ($f_c = 1/60$ Hz) vs. ADCP cross-shore surface velocity RMSE decreases from 0.13 to 0.12 m/s and OF ($f_c = 1/60$ Hz) vs. ADCP cross-shore depth-averaged velocity RMSE decreases from 0.11 to 0.08 m/s. In addition to r^2 and RMSE metrics, it is worth noting the values of the linear regression slope for both velocity components (Figure 5.7e,f). Slope values equal to one indicate a correct steepness for the one-to-one linear relationship between optical flow estimates and ADCP measurements. According to the regression slope, OF ($f_c = 1/20$) velocity estimates indeed reproduce better the ADCP measurements for both velocity components with slope values around 1 ± 0.15. Overall, as the window size is increased, high-frequency noise-related variability (i.e., RMSE) is reduced improving performance metrics (Figure 5.7c,d).

The bias has been intentionally omitted in Figure 5.7 as it poorly depends on the time-averaging window size. Regardless of the window size selection for the moving-average, the bias remain constant and correspond to the same values previously shown in Figure 5.6 and Table 5.2 and 5.3: OF ($f_c = 1/20$ Hz) vs. ADCP longshore velocity bias $= -0.09$ m/s, OF ($f_c = 1/20$ Hz) vs. ADCP cross-shore velocity bias $= -0.17$ m/s, OF ($f_c = 1/60$ Hz) vs. ADCP longshore velocity bias $= 0.01$ m/s and OF ($f_c = 1/20$ Hz) vs. ADCP cross-shore velocity bias $= -0.05$ m/s. Moreover, the bias does not appear to change with ADCP surface or depth-averaged velocity measurements.

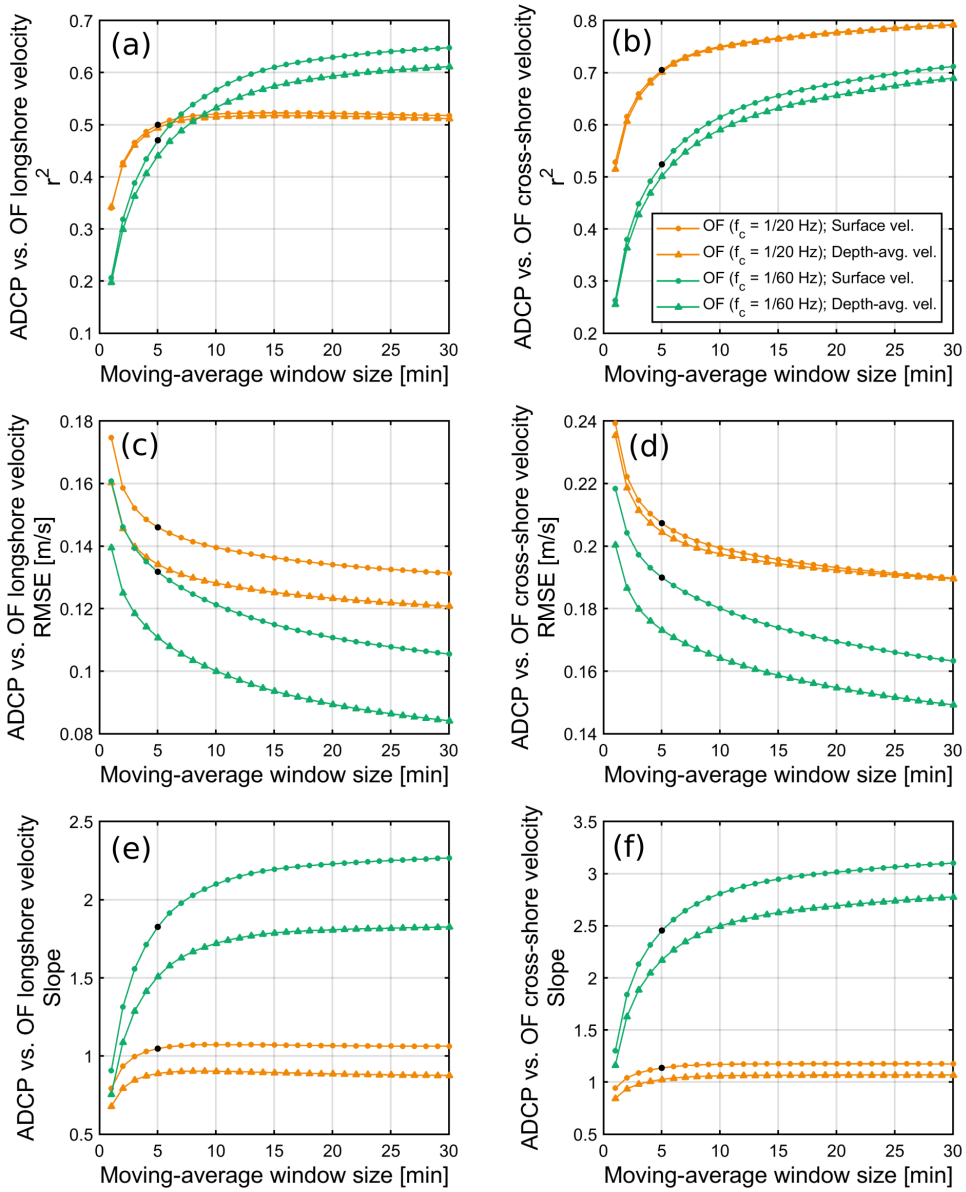

Figure 5.7 – Statistical parameters showing the agreement between ADCP vs. optical flow velocity components by changing the temporal moving-average window size. Data set from 8 to 15 October 2018 using low-pass filtered images with $f_c = 1/20$ Hz (orange line) and $f_c = 1/60$ Hz (green line) for optical flow input. Optical flow velocities are compared against ADCP surface velocities (average between σ_{19}, σ_{20} and σ_{21}; line with circles) and depth-averaged velocity measurements (average of all σ-layers; line with triangles). (**a-b**) Coefficient of determination (r^2), (**c-d**) root mean square error (RMSE) and (**e-f**) linear regression slope for longshore and cross-shore velocity components. The black dots correspond to the 5-min time-averaging window used in previous figures.

Figure 5.8 shows the surface velocity PSDs computed over the 17-averaged 2-h segments 1-week time series. The PSDs reveal a variety of signals present in both ADCP and optical flow time series (e.g., infragravity and VLF fluctuations). As expected, the velocity spectral energy associated with the sea-swell frequency band, previously removed from the image sequence, is subsequently attenuated for frequencies higher than the image low-pass filter cutoff-frequency ($f_c = 1/20$ Hz and $f_c = 1/60$ Hz; black dashed lines). The squared coherence is significant at the 95% confidence level in the infragravity frequency range (0.004 - 0.04 Hz) with values around 0.4 for the cross-shore velocity component. Nevertheless, the frequency region with the highest coherence (≈ 0.6) is associated with the VLF band (<0.004 Hz). Overall, the squared coherence shows a better agreement for OF ($f_c = 1/20$ Hz) velocities. The low spectral energy found in OF ($f_c = 1/60$ Hz) estimates is related to the low amplitude found in the surface velocity time series.

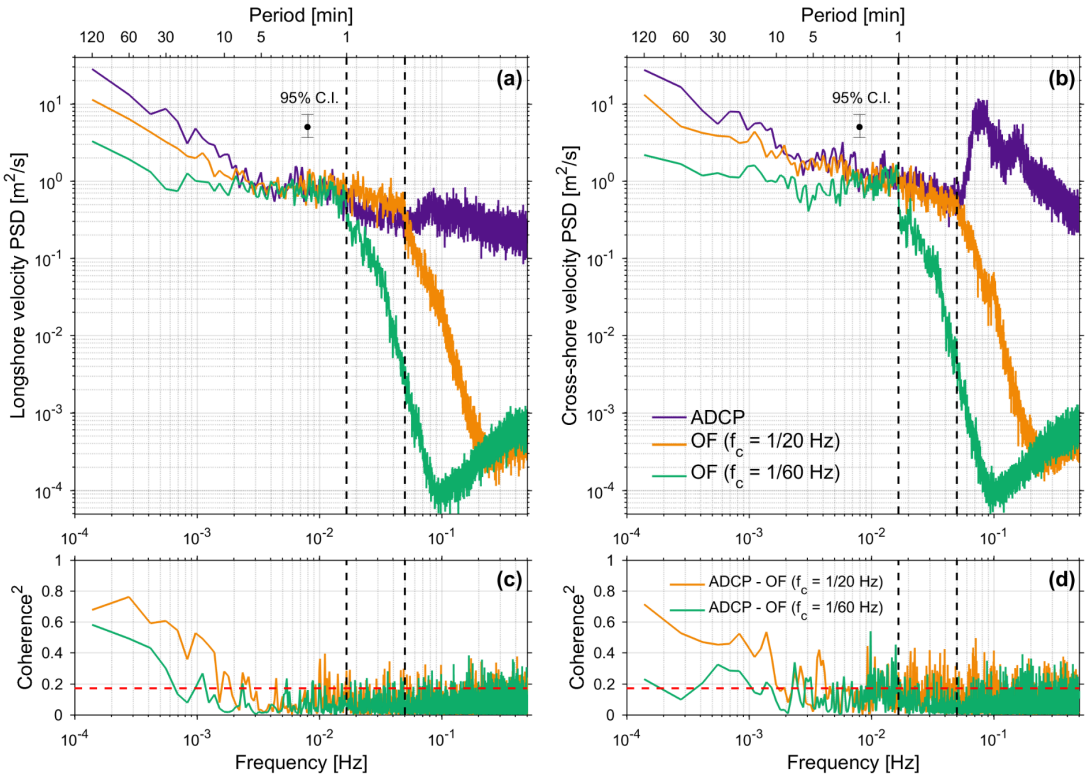

Figure 5.8 – Surface velocity components power spectral density (PSD) and squared coherence computed from the 1-week time series (8 to 15 October 2018) during low tide when the ADCP is located inside the surf zone. (**a**) Longshore and (**b**) cross-shore surface velocity auto-spectra. Squared coherence computed between ADCP and optical flow (**c**) longshore and (**d**) cross-shore surface velocity components along with the 95% confidence bar (red dashed lines). The purple lines indicate the PSDs computed from 1-Hz ADCP surface velocity measurements (average between σ_{19}, σ_{20} and σ_{21}). The orange and green lines show the PSDs generated from optical flow instantaneous (1 Hz) velocity estimates computed from low-pass filtered images with $f_c = 1/20$ Hz and $f_c = 1/60$ Hz, respectively. Frequencies equal to 1/20 and 1/60 Hz are shown with black dashed lines.

5.3.6.2 Drifter deployments

Figure 5.9 shows drifter tracks on 18, 19, 22 and 23 October 2018 along with corresponding optical flow stream plots under different field conditions (Table 5.1). The pixel intensity standard deviation image is also overlaid in each plot to highlight wave breaking spatial variability (e.g., surf zone and reef location) and foam availability during drifter deployment. Days corresponding to 18 and 19 October 2018 (Figure 5.9a,b,c,d) show evidence of primarily onshore-directed flows. Intermittent traces of foam along the headland made it possible to compute mean optical flow estimates outside the surf zone, although velocities in this region may not be reliable due to a lower number of

observations (Anderson et al., 2021). This is the main reason why only qualitatively streamlines are shown to represent the mean surface flow.

More complex circulations are described by the drifters on 22 October 2018 (Figure 5.9e,f). The presence of a quasi-steady circulation cell at the location of the reef is displayed under a combination of moderate-energy and shore-normal incident waves ($H_s = 1$ m; $T_p = 11$ s; $\theta_p = 0°$) around low tide. It is interesting to note the evolution of rip channels inside the surf zone which in turn influences the circulation. Nevertheless, optical flow estimation of the circulation patterns is consistent with the observed drifter tracks. Figure 5.9g presents the trajectories of the first set of drifters released around neap low tide on 23 October 2018, whereas Figure 5.9i shows the trajectories of the remaining drifters deployed during rising low tide. During low tide (Figure 5.9g,h), the wave-induced longshore current is deflected against the headland and affected by wave breaking across the reef resulting in a transient counter-clockwise circulation cell and a deflection rip. As the water level increases (Figure 5.9i,j), the reef exerts less control on rip dynamics allowing the dominant longshore current to completely deflect offshore resulting in a fully-developed deflection rip.

Movies were generated for the four days of drifter deployments and are provided as Supplementary Material (Video S1, Video S2, Video S3 and Video S4). The movies contain the 2-min time-averaged optical flow velocity field overlapped with drifter trajectories. Overall, optical flow is able to recreate satisfactorily the main circulation patterns described by drifters trajectories reproducing smaller circulation structures with a great spatial resolution. Moreover, results are in agreement with previous studies describing the same events (Mouragues et al., 2020b; Sous et al., 2020).

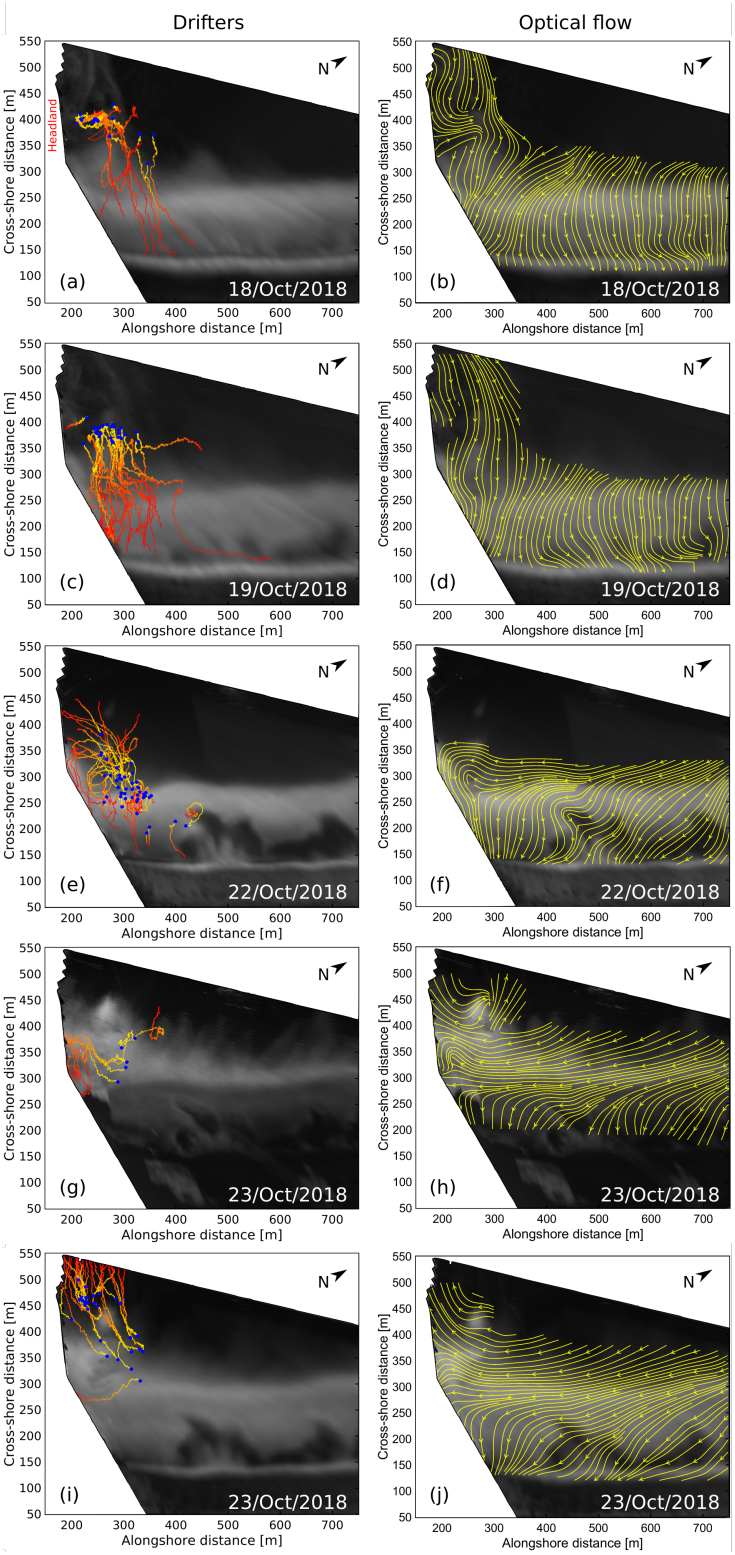

Figure 5.9 – Drifter trajectories (left panel) and optical flow image-derived velocity stream plots (right panel) corresponding to (**a,b**) 18, (**c,d**) 19, (**e,f**) 22 and (**g,h,i,j**) 23 October 2018. (**g,h**) Neap low tide and (**i,j**) rising low tide on 23 October 2018. For each event, the pixel intensity standard deviation image is overlaid to highlight wave breaking spatial variability and foam availability. The blue points indicate the location of drifter seeding. The headland is located within the white masked image region between 0 and 150 m in the alongshore distance.

5.3.7 Discussion

5.3.7.1 Comparison to other optical flow-based methods

In the context of coastal imagery, the shortcomings of the PIV approach and cross-correlation based methods, is that the estimated velocity field resolution is dependent on the size of the user-defined image segments (i.e., one displacement vector per image segment or window) being sparser than the input image resolution (Dérian and Almar, 2017). PIV is also prone to errors under conditions of insufficient surface texture, limiting it to spatially small areas (Puleo et al., 2003). On the other hand, the optical flow method is capable to provide a velocity vector at every pixel of the image. Despite the high potential of this technique, coastal applications are scarce (Philip and Pang, 2016; Dérian and Almar, 2017; Anderson et al., 2021) in contrast with PIV studies (Puleo and Holland, 2000; Holland et al., 2001; Puleo et al., 2003; Perkovic et al., 2009; Wilson et al., 2014; Wilson and Berezhnoy, 2018; Chapman et al., 2019).

Table 5.4 summarizes the performance of existing optical flow-based techniques previously reported in the literature (Dérian and Almar, 2017; Anderson et al., 2021) for estimating two-dimensional nearshore surface currents. The velocity outcomes provided by each method are compared with measurements from specific in situ instruments deployed under different field conditions at particular sites. The main difference between the three methods relies in the pre-processing of the images before the optical flow is applied. In Dérian and Almar (2017) method, a two-dimensional spatial high-pass median filter is applied to each image in order to enhance the foam texture. While this filter improves the fine-scale foam patterns from large-scale structures such as propagating wave rollers, it does not remove the optical wave signal from the images. Their method has the potential to compute instantaneous (wave-by-wave fluctuations) surface velocities, however, the optical flow algorithm is also subject to track pixels propagating at wave celerity and disregard the actual flow. By contrast, Anderson et al. (2021) and the present method filter the wave signal from the image sequence in order to track coherent foam patterns carried by the time-averaged flow, thus constraining the computed surface velocities below the sea-swell frequency band.

Dérian and Almar (2017) compared shore-based image-derived surface velocities

against near-bottom velocities collected from a single Acoustic Doppler Velocimeter (ADV) deployed within the swash zone. As the authors recognized, the comparison between optical flow estimates and instrument measurements was limited by their different location of the vertical profile. Despite drifter measurements acquired during the same field experiment were available (Castelle et al., 2014a; Scott et al., 2018), they were not considered in their analysis. On the other hand, Anderson et al. (2021) compared optical flow derived-velocities against surf-zone drifters velocities using 15x15 m spatial bins. As mentioned by Anderson et al. (2021), drifters were often subject to surfing effects from localized wave-breaking such that they experienced motions at the scale of wave-by-wave fluctuations suggesting that in situ drifter might be unreliable tools for estimating mean currents at the scale of wave groups.

Table 5.4 – Comparison of optical flow-based techniques previously reported in the literature for estimating nearshore surface currents under different field conditions at different sites.

Optical flow-based methods	Dérian and Almar (2017)(Dérian and Almar, 2017)		Anderson *et al.* (2021)(Anderson et al., 2021)		Present study	
	Typhoon		OpenCV		OpenOpticalFlow	
f_s [Hz]	2		2		1	
Image filtering approach	High-pass median filter		Moving-average		Low-pass filter	
Study site	Grand Popo Beach, Benin		Duck, USA		PCA Beach, France	
H_s range [m]	1.2 – 1.6		0.9 – 1.6		0.8 – 3.3	
T_p range [s]	10 – 12		8 – 12		7 – 15	
Water level range [m]	0.3 to 1.2		-0.14 to 0.90		1.5 to 5.9	
Wind speed range [m/s]	-		3.3 – 7.4		0 – 12	
In situ validation	ADV		Drifters		ADCP	
Nearshore region	Swash/Surf zone		Surf zone		Surf zone	
Velocity component	Longshore	Cross-shore	Longshore	Cross-shore	Longshore	Cross-shore
Number of points	8130	8130	>90	>90	136,992	136,992
r^2 range	0.13 – 0.29	0.05 – 0.58	-	-	0.35 – 0.51	0.51 – 0.80
RMSE range [m/s]	0.22 – 0.65	0.12 – 0.58	0.15	0.13	0.12 – 0.17	0.19 – 0.24

5.3.7.2 Low-pass filter cutoff-frequency selection

The optical flow algorithm is very sensitive to the image input and the selection of the cutoff-frequency for the temporal low-pass filter can have a great impact on the final velocity estimates. OF ($f_c = 1/60$ Hz) velocity estimates presented lower velocities and less spectral energy than ADCP measurements. For the temporal low-pass filter, using a cutoff-frequency of 1/60 Hz is equivalent to averaging images consecutively over 1 min. By proceeding with this selection, the dominant sea-swell band is evidently removed

from the image sequence, however, all residual foam features become smeared and over-smoothed resulting in lower and underestimated velocity values (see histograms in Figure 5.6c,d). Furthermore, time-averaging these values can result in velocities close to zero with still a good linear correspondence to ADCP measurements with low RMSE and low bias. This can lead to a misinterpretation of good performance, as shown by the regression slope (Figure 5.6c,d and Figure 5.7e,f) and the damped velocity time series (Figure 5.5). By contrast, OF ($f_c = 1/20$ Hz) velocity estimates demonstrate satisfactory agreement with surf-zone drifters tracks and ADCP measurements under relatively high-energy waves ($H_s < 2.5$ m). Velocity RMSE of less than 0.25 m/s is a reasonably satisfactory result considering that the spatial resolution of the image grid is 1 m and the pixel footprint at the ADCP location is 0.6 m. On the other hand, the apparent bias and overall underestimation in offshore-directed currents (overestimation in onshore-directed currents) can be explained by other sources of error (see subsection 5.3.7.4).

5.3.7.3 ADCP measurements: surface vs. depth-averaged velocities

Directly comparing remote sensing products with in situ instruments is complicated. Optical flow estimates are representative of the motions occurring in the water surface layer, whereas, in the case of the ADCP, velocities corresponding to the upper region of the water column are usually removed to avoid possible errors associated with sidelobe interference, bubble injection, Stokes drift and wind contamination. Thus, it is difficult to evaluate "true" errors as velocities are compared from different locations of the vertical profile. However, for this particular study, the fact that r^2 and RMSE do not differ as much when compared against ADCP surface or depth-averaged velocities suggests that the vertical variability of the flow is nearly depth-uniform. Figure 5.10 illustrates three representative 2-h time-averaged velocity profiles in σ coordinates. The velocity profiles were computed under different angles of wave incidence at low tide (around 2 and 3 m of water depth). The three configurations indicate shallow water flows with no significant vertical gradient, consistent with previous observations around the ADCP location (Sous et al., 2020; Mouragues et al., 2020b). These results show evidence of a nearly depth-uniform flow, however, for other locations inside the surf zone the vi-

sual surface layer might not always be representative of the entire water column. In case of strong vertical shear, the proposed ADCP transformation to σ coordinates can be an alternative to derive velocities near the water surface consistent with video-derived estimates. However, caution must be exercised given the inherent limitations of the instrument when measuring close to the free surface.

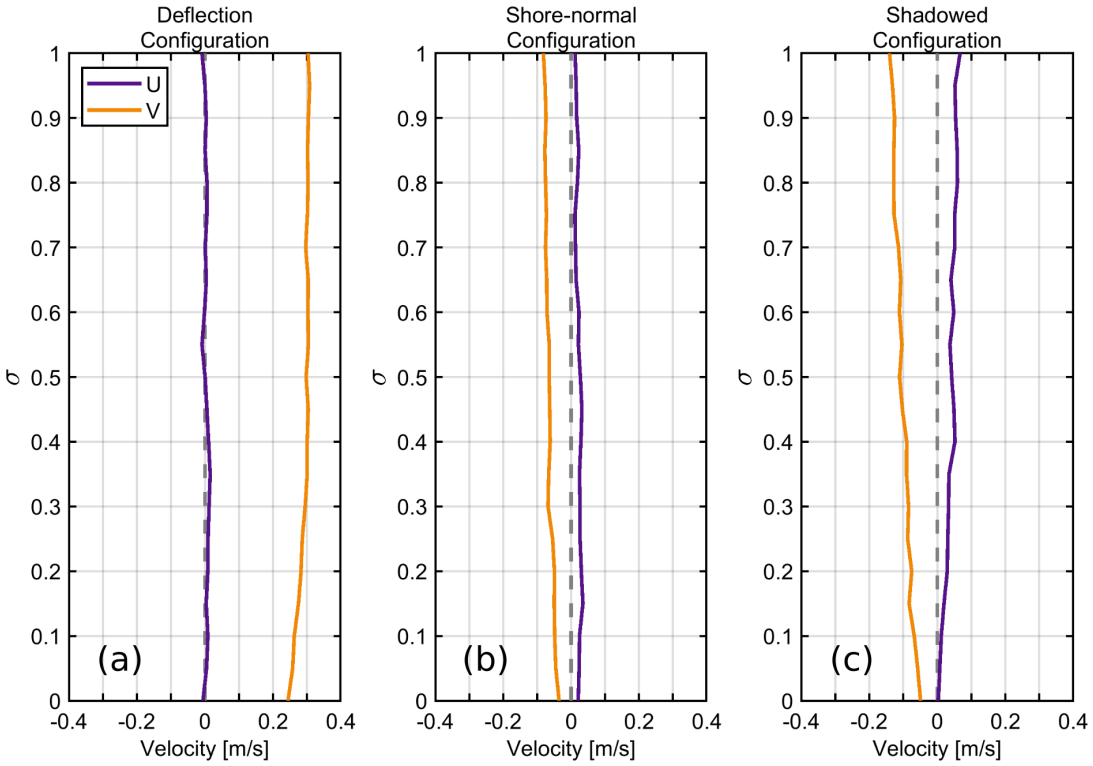

Figure 5.10 – ADCP 2-h burst-averaged σ-velocity profiles under different offshore incident wave obliquity at low tide. (**a**) Deflection configuration (08/Oct/2018−08-10:00:00 GMT), (**b**) shore-normal configuration (11/Oct/2018−11-13:00:00 GMT) and (**c**) shadowed configuration (15/Oct/2018−12-14:00:00 GMT). Longshore ($U > 0$; current directed away from the headland) and cross-shore ($V > 0$; offshore-directed current) velocity components are shown in purple and orange colors, respectively.

5.3.7.4 Sources of error

It should be noted that optical flow struggled to reproduce offshore-directed velocities at the ADCP location as revealed in the cross-shore velocity time series (Figure 5.5b) and the one-to-one comparison (Figure 5.6b). This can be mainly attributed to wave breaking. Although the frequency band corresponding to sea-swell waves is removed from the images, the source of foam, induced by wave breaking, appears as a blob that increases

and spreads with time in the onshore direction following the filtered pre-existing wave front. Figure 5.11 illustrates the instantaneous circulation flow under wave breaking at two different instants separated by 7 s. In this representative example, ADCP velocities indicate a depth-uniform offshore-directed flow (as previously suggested). A close inspection of the optical flow velocity field near the ADCP location (Figure 5.11a,c) reveals instead a transient clockwise circulation cell which after 7 s (Figure 5.11b,d) is modified to be aligned with the incoming filtered wave front moving toward the shore. This effect is also observed with the isolated foam blob advancing around coordinates with alongshore distance = 410 m and cross-shore distance = 350 m (green polygon). However, this issue occurs in any region where strong wave breaking is present (e.g., reef and sandbar) and is also observed with low-pass filtered images with $f_c = 1/60$ Hz. This suggests that the optical flow can erroneously track foam patches at the instant of their creation potentially masking true underlying velocities at those times. Therefore, a proper definition for the $f(x_1, x_2, I)$ term inside the physics-based optical flow equation (Eq. 5.1) is needed in order to account for specific foam properties such as source and dissipation rates, or alternatively, remove the velocity estimates associated with pixels that break in post-processing (Anderson et al., 2021).

Surface velocity accuracy can also be limited by windage effects. Ideally, foam is expected to be advected only by the underlying currents, however, under high wind conditions, wind stress can induce surface currents that can advect the foam in a different direction than the desired surface/near-surface water flow. This could be probably the case during the relatively strong wind event on 14 October 2018, when wind speed reached up to 12 m/s. Other video-related sources of errors such as unwanted camera movement (e.g., produced by wind) (Bouvier et al., 2019; Rodriguez-Padilla et al., 2020), overlapping camera boundaries and tide dependent inaccuracies in georectification (Bergsma et al., 2016) may also affect the performance of the optical flow-based technique and should be properly addressed before the optical flow method is applied.

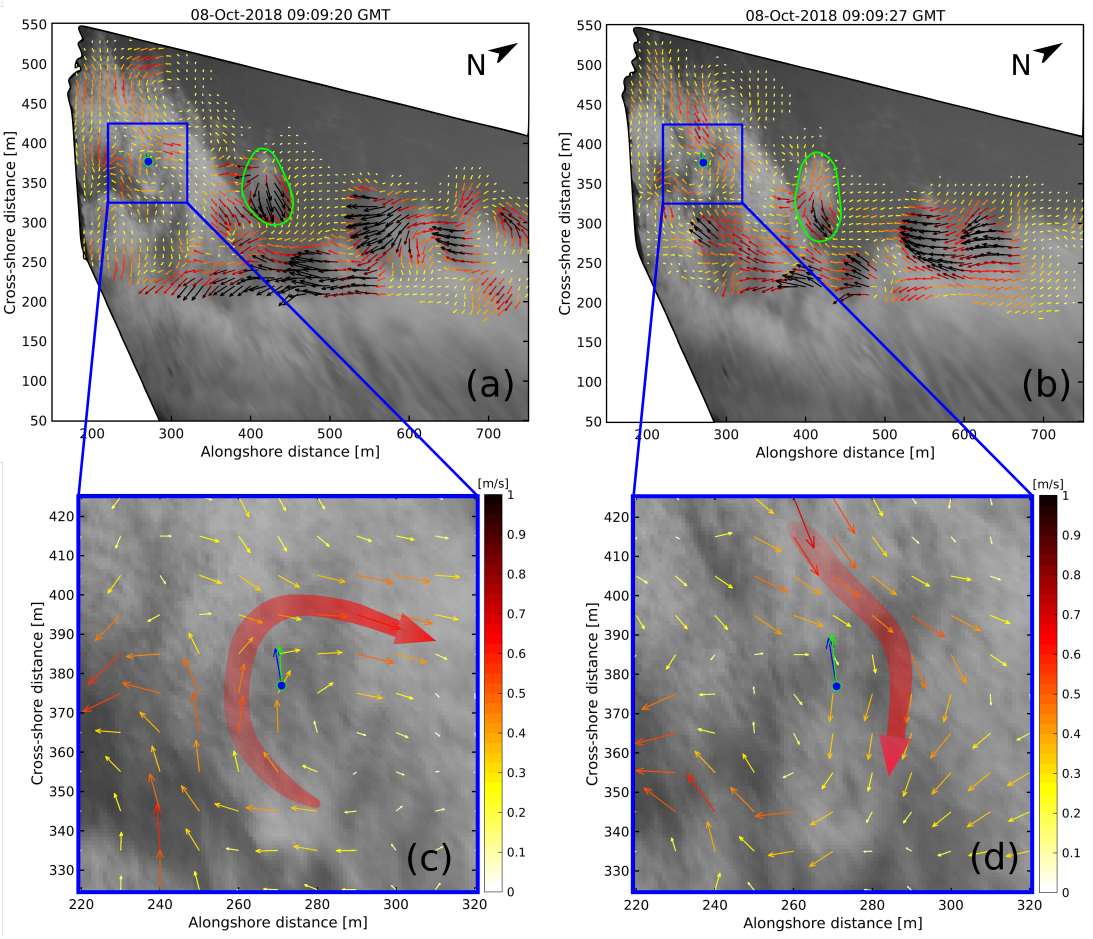

Figure 5.11 – Influence of wave breaking on optical flow velocity estimates. Example of filtered breaking waves captured at instant (**a**) 08/Oct/2018−09:09:20 GMT and (**b**) 7 s after. (**c,d**) The same instants are shown for the image-region associated with the ADCP location depicted with blue color. Instantaneous OF ($f_c = 1/20$ Hz) velocity arrows are displayed every 10 m for better visualization. The blue and green arrows correspond to 20-s time-averaged ADCP surface and depth-averaged velocities, respectively. Optical flow and ADCP arrows are scaled the same. The thick red arrow represents the optical flow-derived dominant circulation for each instant. The green dashed line polygon illustrates an example of the creation of a foam blob advancing toward the shore induced by wave breaking.

5.3.7.5 Recommendations and future work

Optical flow is a powerful technique, however, certain factors and limitations must be considered in order to obtain satisfactory results. The first assumption, inherent to any optical flow algorithm, is that the pixel intensity between two consecutive frames should be nearly constant. Therefore, it is preferable to correct the scene illumination (e.g., by histogram equalization) before applying the optical flow method to increase accuracy. As described in Appendix A, we used a subroutine included in Liu (2017)

OpenOpticalFlow algorithm to correct the local illumination intensity changes between frames. Brightness variations can also be constrained to small changes if a coarse-to-fine scheme is used (see Appendix A) or if frames are sampled at a high rate (>1 Hz). However, this can have a direct impact on storage resources. An alternative to overcome this issue, as proposed by Anderson et al. (2021), is to downsample the number of frames (e.g., by a factor of 5) once the dominant optical sea-swell wave signal is filtered from the image sequence, and then further apply the optical flow algorithm. Image temporal downsampling is possible after removing the wave clutter since the residual foam is smoothed in such a way that brightness variations between consecutive frames are kept low. However, filtering the optical signature from the images is a key step that must not be overlooked.

As shown in Figure 5.5, it is important to discard velocity values associated with pixels outside the surf zone or regions where no foam is present, otherwise, the optical flow algorithm will assign velocity values close to zero and underestimate the actual surface flow. For the ADCP pixel location we deduced the time when the instrument was inside the surf zone based on the water depth and kept only those corresponding velocity values. On the other hand, for the drifter experiments we removed all time-averaged velocities smaller than 0.02 m/s to ensure that the remaining velocities (streamlines) corresponded to regions where foam was present (e.g., surf zone). Future work should include a post-processing step, similar to the one proposed by Anderson et al. (2021), to automatically identify and isolate foam regions based on a local pixel brightness variation threshold between frames in order to discard spurious velocities when there is limited texture on the water surface to track.

It should be noted that the intermittent wave breaking region where the ADCP was deployed was a particularly challenging location for the optical flow algorithm to produce accurate velocity estimations. Therefore, we propose that further research should be undertaken by mounting current profilers distributed at different locations within the surf zone to provide the optical flow algorithm the optimal conditions for a consistent comparison.

5.3.8 Conclusions

In this paper, we presented an alternative method to filter the dominant optical signal associated with sea-swell waves from an image sequence. Waves were removed from the image time series by applying a temporal Fourier low-pass filter to each pixel of the image. After image-wave-filtering, the residual foam left by wave breaking was used as a quasi-passive tracer and was assumed to be advected primarily by the underlying flow; wind conditions during the experiment were relatively weak with mean wind speed values around 3 m/s. Foam trajectories within the surf zone were tracked using Liu (2017) open-source optical flow algorithm ("OpenOpticalFlow") to derive wave-filtered surface velocities (comprising frequencies below 1/20 Hz and 1/60 Hz). We proposed an approach based on depth-normalization of the water profile (σ-layers) to retrieve surface velocities from ADCP measurements. A transformation of z to σ coordinates ensures that the velocities derived from the ACDP are as consistent as possible with those estimated from the optical flow algorithm. Optical flow-derived velocities were compared with ADCP time-averaged surface and depth-averaged velocities. ADCP measurements displayed nearly depth-uniform time-averaged velocities. Time-averaged optical flow velocity estimates, using low-pass filtered images with $f_c = 1/20$ Hz as input, showed to be in good agreement with ADCP measurements ($r^2 = 0.5 - 0.8$; $\mathrm{RMSE} = 0.12 - 0.24$ m/s; bias $= -0.09$ to -0.17 m/s; $\mathrm{slope} = 1 \pm 0.15$; $\mathrm{coherence}^2 = 0.4 - 0.6$). By contrast, optical flow-derived velocities, using low-pass filtered images with $f_c = 1/60$ Hz as input, were overall underestimated due to an over-smooth of the foam features. In any case, optical flow offshore-directed velocities were systematically underestimated. This outcome can be justified by waves breaking over the reef (i.e., ADCP location) that produce and advect foam persistently toward the shore. The onshore-directed motion of the foam, induced by wave breaking, can differ from the actual underlying flow and can inadvertently be captured by the optical flow algorithm. Despite this apparent limitation, optical flow was able to qualitatively reproduce with a good agreement the mean current circulation patterns described by drifter trajectories under different wave, tide and wind conditions. Among these patterns, a rip-circulation cell was captured as well as a prominent and persistent rip current flowing against the headland (deflection rip). Such findings highlight the

ability to detect rip currents and associated circulations at different time-averaging scales providing new insights into surf-zone hydrodynamics and invaluable resources for beach safety strategy.

5.4 Implications and potential of optically derived wave-filtered surface currents

The nearshore is difficult to study comprehensively using only in situ data as a large number of instruments are required to adequately sample the time and spatial scales associated with nearshore circulation (10 s−1000s meters) (Perkovic et al., 2009). As stated by MacMahan et al. (2010), comprehensive kinematic fluid characteristics of the surf zone motions is hindered by the lack of synoptically observed flow fields. For these reasons, the optical current meter technique presented in this work has the potential for providing new insight into fundamental surf zone dynamics not obtainable with previous in situ measurements or remote sensing products.

The ability to continuously quantify surf zone circulation patterns over a large area using a simple low-cost video system has the potential to reveal variability on time scales ranging from tidal level changes (a few hours) to beach state progressions occurring on the order of weeks to seasons. To our knowledge, there are no other observational approaches that can map surf-zone (wave-filtered) surface currents on comparable spatial and temporal scales.

An illustrative example of the ability to capture short-term temporal variability is provided in Figure 5.12, where estimated wave-filtered surface velocities were averaged over 20 minutes for low tide and high tide on 22 October 2018 under shore-normal incident waves. At low tide (Figure 5.12a), the intensity of wave breaking on the sandbar became amplified, more foam was generated, the surf zone became wider (100 m) and the swash zone contained less energy. This hydrodynamic and morphodynamic configuration enabled complex circulation patterns. The mean vorticity field was computed following (MacMahan et al., 2010) to highlight the positive vorticity associated with the counter-clockwise rip circulation cell (at the location of the reef) and the eddy

formed inside the rip channel (Figure 5.12b). By contrast, at high tide (Figure 5.12c), the surf zone width decreased (50 m) with intermittent breaking on the sandbar and a swash zone noticeable in the timex and pixel intensity standard deviation image (Figure 5.12c,d). Variability (standard deviation) ellipses show the mean surface velocities along with their temporal variability at high tide.

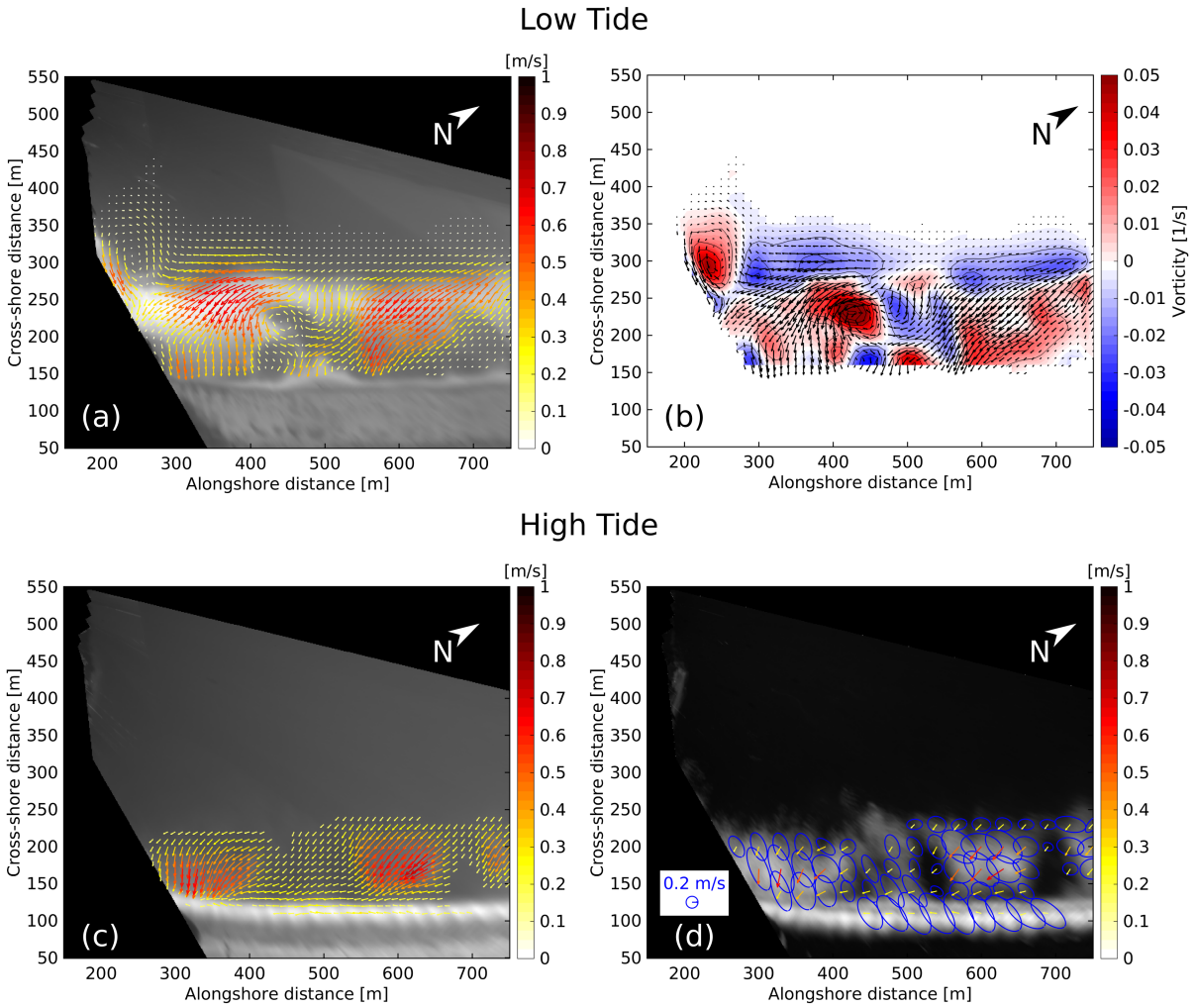

Figure 5.12 – Mean optical flow-derived products from 20-min video recording on 22 October 2018 at low tide and high tide. (**a**) Mean surface velocity vector field overlaid on the 20-min timex image and (**b**) associated vorticity field computed at low tide. (**c**) Mean surface velocity vector field overlaid on the 20-min timex image and (**d**) associated variability ellipses overlaid on the 20-min pixel intensity standard deviation computed at high tide.

Longshore sediment transport is the single most important agent of coastal change along most of the world coastlines (Chickadel et al., 2003). Longshore transport of sediment, pollutants and biological species is driven primarily by longshore mean currents

which are induced by an obliquely incident wave field. Figure 5.13 shows the potential in estimating the longshore current structure from video. Intensity and cross-shore extent of the longshore current can be analyzed to understand the hydro/morphodynamic factors that control and modulate the current patterns. Optical flow-derived velocities may also be useful to study very low frequency motions (<0.004 Hz) such as shear waves, a type of motion in the surf zone associated with longshore current instabilities (Bowen and Holman, 1989; Oltman-Shay et al., 1989). On the other hand, time series analysis techniques, such as harmonic analysis can be applied to individual pixel grid locations to separate the tidal constituents from other fluctuations in order to estimate tidal currents in coastal environments such as tidal inlets or estuary mouths.

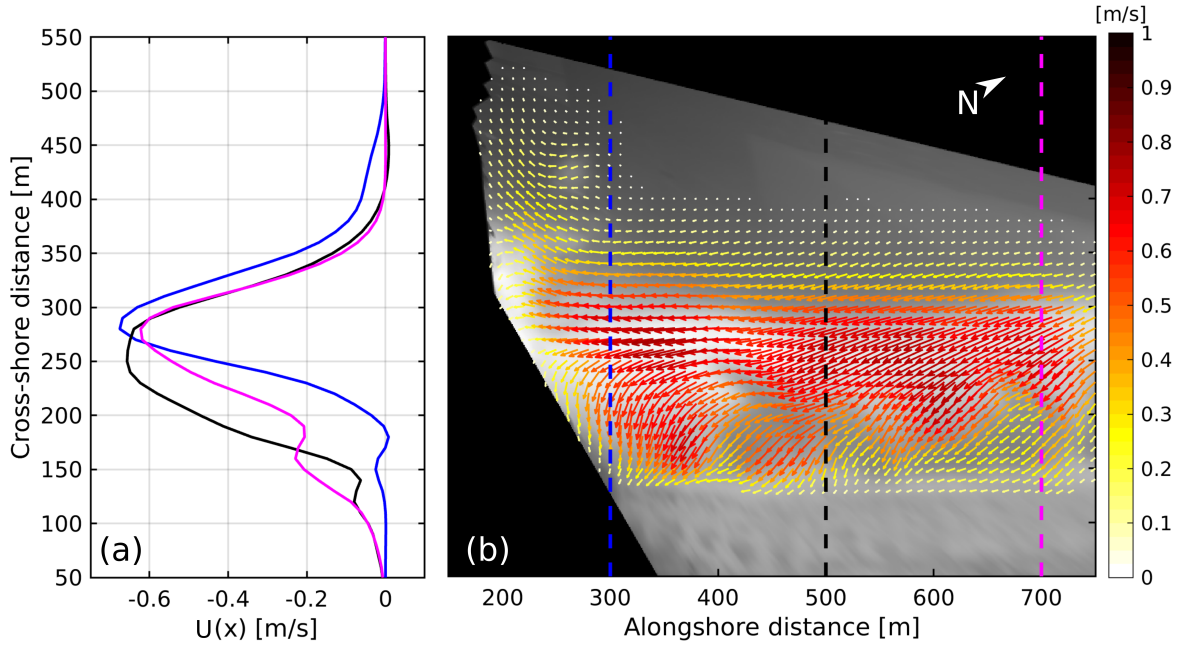

Figure 5.13 – Optical flow-derived velocities on 23 October 2018 corresponding to the deflection rip event. (**a**) 3.5-h mean cross-shore profile of the longshore current at different locations (U < 0; current directed toward the headland); the cross-shore transects (dashed lines) are indicated with different colors. (**b**) Optical flow surface velocity vector field overlaid on the 3.5-h timex image.

Chapter 6

Conclusions and perspectives

Contents

6.1 General conclusions

This work primarily focused on the development and implementation of optical remote sensing techniques to study nearshore morphodynamic and hydrodynamic processes under high energy wave conditions in a meso-macro tidal environment. A side objective was to assess the extent to which remote sensing techniques could provide reliable data under harsh field conditions and propose new processing approaches to guarantee an optimal accuracy in the final video-derived product. The data used in this thesis builds (mainly) upon the comprehensive 3-week field experiment carried out on October 2018 in one of Anglet beaches (SW France), La Petite Chambre d'Amour, where I had the opportunity to participate and collaborate with researchers from other institutions such as from the University of Plymouth and Université Pau et Pays de l'Adour. In this final chapter, the general results are summarized and concluding remarks are

briefly discussed. Finally, the results are placed in perspective and future investigation is proposed.

6.1.1 Image stabilization

We developed an efficient semi-automatic procedure to stabilize an image sequence using state-of-the-art techniques in order to remove unwanted camera movement after video acquisition. We investigated the impact of camera viewing angle deviation when monitoring the nearshore. Our results show that camera movements occur on a wide range of timescales and induce large geo-rectification errors at the fixed video monitoring station of Anglet, which is often the case but is disregarded for many other video stations worldwide. One primary problem with existing stabilization methods is that they are sensitive to changes in brightness and contrast making them prone to failure. This method provides a robust solution to stabilize an either continuous or sub-sampled image sequence under varying illumination with the ability to process large databases.

The image stabilization method required the presence and identification of different land-sub-image regions containing static recognizable features (referred to as keypoints), such as corners or salient points. Keypoints were matched against themselves after computing their two-dimensional displacement with respect to a reference frame. The vertical (tilt) and horizontal (azimuthal) pixel displacement was obtained using a cross-correlation algorithm with sub-pixel accuracy (Guizar-Sicairos et al., 2008a) together with a Canny edge detection filter (Canny, 1986). Pairs of keypoints were afterwards used as control points to fit a geometric transformation in order to align the whole frame with the reference image. The stabilization method was applied to 5 years of daily images collected from a three-camera permanent video system located at Anglet Beach, 70 m above mean sea level. Azimuth, tilt and roll deviations with respect to the initial frame were computed for each camera. In addition, 2.5 km of shoreline were manually digitized for the outstanding winter period of 2013/2014 using non-stabilized and stabilized rectified images to estimate the real-world horizontal positioning error due to camera movement.

The three cameras presented motion during all the time series and showed a particular annual signal in azimuth and tilt deviation. This can potentially be attributed

to the sun position and thermal expansion fluctuations. Camera movement amplitude reached approximately 10 pixels in azimuth, 30 pixels in tilt and 0.4° in roll, together with a quasi-steady counter-clockwise trend over the 5 year time series period. Moreover, camera viewing angle deviations were found to induce large rectification errors up to 400 m at a distance of 2.5 km from the camera. The mean shoreline apparent position was also affected by an approximately 10-20 m bias during the 2013/2014 winter period.

6.1.2 Nearshore bathymetric mapping from video imagery

For three consecutive weeks we estimated bathymetry maps every 30 min during daylight hours using a video-based linear depth inversion algorithm *cBathy* (Holman et al., 2013) to examine PCA beach morphological response under a wide range of wave ($H_s = 0.5 - 3.3$ m; $T_p = 6 - 15$ s) and tide ($\sim$4 m) conditions. The assessment was carried out by comparing concurrent video-derived bathymetries with in situ topo- bathymetric measurements collected during the beginning and end of the field experiment. Comparisons between surveyed and video-derived bathymetric estimates showed a similar performance with respect to previous studies (Brodie et al., 2018) with an overall RMSE = 0.29$-$0.37 m and bias = 0.56$-$0.57 m. However, the temporal evolution of estimated bathymetries revealed large discrepancies in depth (a systematic overestimation in depth fluctuating between 1 and 1.5 m over the whole domain). The sea bed was found to vary instantaneously with the tide, which is non-physical. We suspect that the tide-dependent depth inconsistency is attributed to a rectification issue that will require further investigation. Meanwhile, the error seems to be closely related to the (varying) reference level at which the oblique image is projected, which in case of inaccuracy, could potentially induce positioning errors and mistakenly feed the cBathy algorithm. To overcome this problem, we filtered out the spurious high-frequency depth-modulation signal to keep only the slow-varying (>2 days) changes in depth.

The smoothed bathymetry time evolution showed the transition from a Low Tide Terrace (LTT) to a Transverse Bar and Rip (TBR) beach state according to Wright and Short (1984) classification. During the beginning of the field experiment, the sandy bed

morphology was reasonably uniform alongshore showing a terrace bar attached to the shore with a slight central crest located around 250 m in the cross-shore. Comparison between surveys revealed the formation of an alonghore uniform sandbar centered at cross-shore position = 300 m with a net deposition of sand (around 1-m of accretion) within the reef region. This result is consistent with the gradual accumulation of sand registered in the video-derived bathymetry estimates during the end of the experiment, when an energetic wave event (waves up to 3 m high) occurred. As shown in the bathymetric surveys, the sand accretion is suspected to be driven by onshore sediment transport, as all the region outside the surf zone (beyond the camera domain) eroded during the course of the experiment. Furthermore, change in wave and tidal regime induced the formation of a rip channel incising the sandbar, resulting in increased neashore alongshore variability. .

Overall, cBathy-derived bathymetries were consistently overestimated with respect to the surveys (and ADCP water depth measurements) with larger differences for the upper part of the beach and the shallow region around the reef. As we encountered a systematic tide-dependent bias, probably originated from a rectification inaccuracy, it is difficult to assess the extent to which the vertical offset may be caused by nonlinear effects and wave-current interactions reducing the validity of the linear dispersion relation on which cBathy is based.

6.1.3 Optically derived wave-filtered surface currents

We explored the potential of computing 2-D wave-filtered surface currents from video images by tracking the drifting foam, left after the passage of breaking waves, using an open-source optical flow algorithm (Liu, 2017). This algorithm looks for nearby pixels of the same brightness intensity assuming small motion between frames. The optical flow algorithm relies on a global formulation with a smoothness constraint which is capable to provide a velocity vector at every pixel of the image resolving the entire flow simultaneously.

We proposed a new approach, based on a Fourier Low-pass filter, to remove the dominant optical signal associated with sea-swell waves from an image sequence to avoid tracking propagating waves instead of the desired foam assumed to be advected

only by the flow. For the first time, we compared optical flow-derived velocities with in situ current profiler measurements under high-energy wave conditions ($H_s = 0.8 - 3.3$ m) during one week of simultaneous measurements. In addition, we validated optical flow-derived circulation patterns with surf-zone drifter trajectories under different field conditions. Our results show that the optical flow method is capable to reproduce mean surface velocities below the sea-swell frequency band with a fair agreement ($r^2 = 0.5 - 0.8$; RMSE$= 0.12 - 0.24$ m/s) and is able to capture time-averaged circulation structures inside the surf zone with a great spatial resolution.

PCA beach inherited geological features (headland and submerged reef) exert a strong control on nearshore circulation. At low tide, under shore-normal waves, the submerged reef plays a mayor control in flow dynamics inducing cross-shore motions and a rip cell circulation as waves start to break over the reef. On the other hand, obliquely incident waves result either in a shadowed or deflection configuration depending on which side of the headland waves are coming from. During shadowed configuration, surface currents are primarily onshore directed flowing away from the headland driven by alongshore variations in wave breaking induced by the shadowing effect of the headland. By contrast, during deflection configuration, the longshore current is deflected against the headland resulting in a strong seaward flow extending well beyond the surf zone. These three main circulation regimes, previously described for the same experiment in Mouragues et al. (2020a,b) using drifter measurements and a small number of current profilers, were recreated fairly well by the optical flow time-averaged surface velocity estimations.

6.2 Research perspectives

Many research groups worldwide use video monitoring systems to remotely sense nearshore hydrodynamics and morphodynamics. Remote sensors are less invasive, are easier to deploy and maintain, and offer wider areal coverage than typical arrays of in situ instruments (Perkovic et al., 2009). The increasingly proliferation of low-cost and flexible new platforms such as UAVs, swift cameras, CoastSnap (Harley et al., 2018), etc., offers an attractive option to collect image products and derive measurements of

the nearshore. Whether it is with fixed video station or camera-equipped UAV, the image processing techniques should, in principle, be transferable and compatible between platforms. As a demonstration, Figure 6.1 shows the image stabilization method proposed in this thesis applied to an UAV flight in order to remove the unwanted movement of a random frame. Overall, we observe that there is a satisfactory performance of the method.

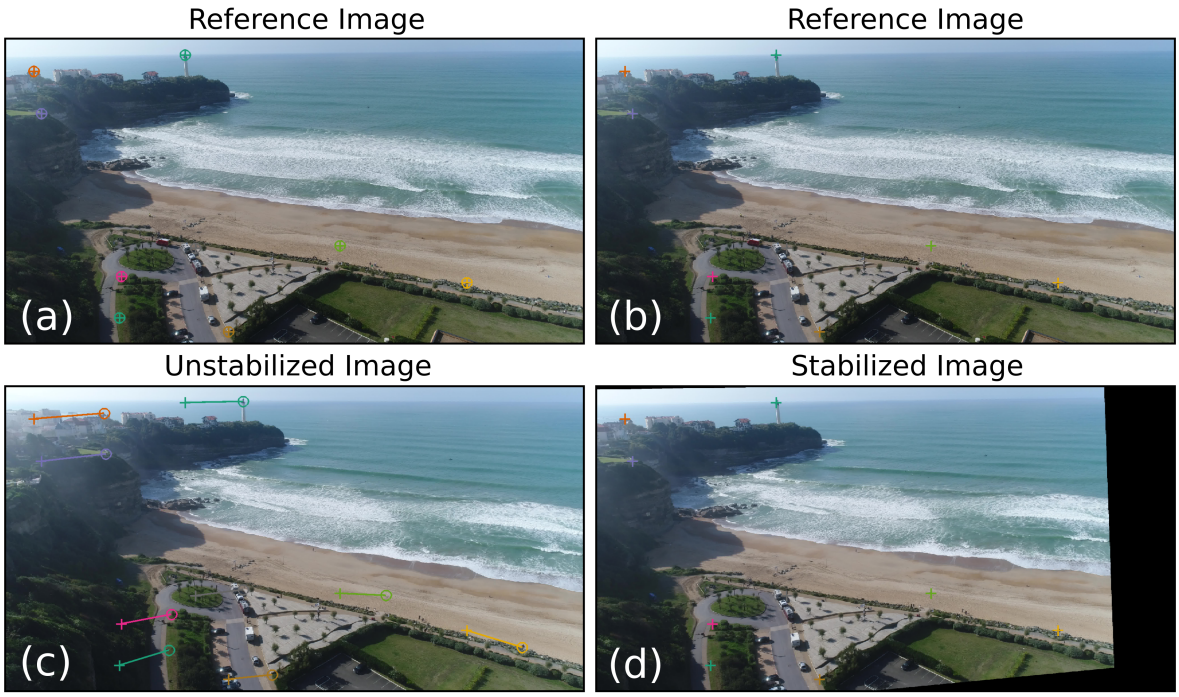

Figure 6.1 – Two snapshots captured from a drifting UAV-flight. (**a,b**) Reference image, (**c**) unstabilized image and (**d**) stabilized image. The colored crosses are the user-defined static keypoints with respect to the reference image, whereas the circles indicate their shifted position.

Further work could be to use the UAV data collected during Anglet field experiment to examine the offshore part of the deflection rip which was systemically outside from the fixed camera view field. This could help to further understand the structure of such rips as they detach offshore from the headland. However, this is only possible if enough foam is advected by the deflection rip so it can be tracked by the optical flow algorithm.

Optical flow video-based technique has the potential to provide unprecedented insight into surf zone hydrodynamic processes at scales that were previously difficult to reach. As we applied the optical flow-based method to an optical video camera, surface velocities can only be estimated during daylight hours. However, infrared video

cameras are not constrained by this limitation. The same optical flow method can be applied to infrared imagery to track the remnant foam (which is typically cooler than the surface water and/or recently generated foam; Wilson et al. 2014) at any time either daylight or nightlight hours. This could also be the case for X-band radar imagery if enough sea-clutter is available for tracking.

Video-derived surface currents can provide critical contextual data for both theoretical and applied nearshore studies. From the perspective of hazard to recreational beach users, identification and awareness of rip currents are essential for coastal and beach safety (Castelle et al., 2016b). In this sense, the optical current meter enables to monitor both the average and transient circulation, such as flash rips, for which the location of occurrence is random. The rapid development of webcams and UAVs together with the recent growing body of machine learning recognition algorithms offer the possibility to provide quantitative information at a reasonable instrumental and computational cost (Dérian and Almar, 2017). Operational use of this optical flow-based current meter using low-cost image platforms combined with open-source computer vision algorithms to automatically detect rip currents could provide crucial near-real time safety messages to beach users before entering the water.

To sum up, in this thesis we proved that nearshore remote sensing is a promising and still ongoing discipline with the capability to link observations with specific geophysical quantities. This study opens new perspectives to routinely improve camera geometry of video monitoring systems and to further derive higher quality remotely sensed hydrodynamic and morphological products. Furthermore, this work opens up new avenues for frequently monitoring rip currents and associated circulations, which is critical for scientific interests and beach safety strategy. We therefore think that our findings will impact the coastal community and our methods will be used by many research groups worldwide.

List of publications and presentations

Contents

I . Scientific publications

First author:

- **Rodríguez-Padilla, I.**, Castelle, B., Marieu, V., Bonneton, P., Mouragues, A., Martins, K., and Morichon, D. (2021). Wave-Filtered Surf Zone Circulation under High-Energy Waves Derived from Video-Based Optical Systems. *Remote Sensing*, 13(10):1874.

- **Rodríguez-Padilla, I.**, Castelle, B., Marieu, V., and Morichon, D. (2020). A Simple and Efficient Image Stabilization Method for Coastal Monitoring Video Systems. *Remote Sensing*, 12(1):70.

Co-author:

- Mouragues, A., Bonneton, P., Castelle, B., Marieu, V., Barrett, A., Bonneton, N., Detand, G., Martins, K., McCarroll, J., Morichon, D., Poate, T., **Rodríguez-Padilla, I.**, Scott, T., and Sous, D. (2020a). Field Observations of Wave-induced Headland Rips. *Journal of Coastal Research*, 95(SI):578–582.

- Mouragues, A., Bonneton, P., Castelle, B., Marieu, V., Jak McCarroll, R., **Rodríguez-Padilla, I.**, Scott, T., and Sous, D. (2020b). High-Energy Surf Zone Currents and Headland Rips at a Geologically Constrained Mesotidal Beach. *Journal of Geophysical Research: Oceans*, 125(10):e2020JC016259. e2020JC016259 10.1029/2020JC016259.

II . Participation in conferences, meetings and workshops

- **Rodríguez-Padilla, I.**, Castelle, B., Marieu, V., Bonneton, P., Mouragues, A., Martins, K., and Morichon, D. (2021). The Use of Optical Flow to Estimate Nearshore Surface Currents From Video Imagery (2021). *8th edition of the Coastal Dynamics Conference*, Delft, Netherlands, **Poster**.

- **Rodríguez-Padilla, I.**, Castelle, B., Marieu, V., and Morichon, D. (2020). Alternative Image Stabilization Method for Coastal Video Monitoring Systems. *Virtual International Conference on Coastal Engineering*, **Oral**.

- **Rodríguez-Padilla, I.** (2019). Alternative Image Stabilization Method for Video Systems. *Third CIRN Boot Camp & CoastSnap Users Group Meeting*, Toulouse, France, **Oral**.

Bibliography

Aarnink, J. (2017). Bathymetry mapping using drone imagery.

Aarninkhof, S. and Roelvink, J. (1999). Argus-based monitoring of intertidal beach morphodynamics. In *Proceedings of Coastal Sediments 99*, pages 2429–2444.

Aarninkhof, S., Ruessink, B., and Roelvink, J. (2005). Nearshore subtidal bathymetry from time-exposure video images. *Journal of Geophysical Research: Oceans*, 110(C6).

Aarninkhof, S., Wijnberg, K., Roelvink, D., and Reniers, A. (2006). 2dh-quantification of surf zone bathymetry from video. In *Coastal Dynamics 2005: State of the Practice*, pages 1–14.

Aarninkhof, S. G. and Ruessink, B. G. (2004). Video observations and model predictions of depth-induced wave dissipation. *IEEE Transactions on Geoscience and Remote Sensing*, 42(11):2612–2622.

Aarninkhof, S. G., Turner, I. L., Dronkers, T. D., Caljouw, M., and Nipius, L. (2003). A video-based technique for mapping intertidal beach bathymetry. *Coastal Engineering*, 49(4):275–289.

Aarninkhof, S. G. J. (2003). Nearshore bathymetry derived from video imagery.

Abadie, S., Butel, R., Dupuis, H., and Brière, C. (2005). Paramètres statistiques de la houle au large de la côte sud-aquitaine. *Comptes rendus geoscience*, 337(8):769–776.

Abdel-Aziz, Y. and Karara, H. (1971). Direct linear transformation from comparator coordinates into object space co-ordinates. In *Proc. ASP/UI Symposium on Close-range Photogrammetry*.

Accensi, M. and Maisondieu, C. (2015). Homere. ifremer-laboratoire comportement des structures en mer.

Adrian, R. J. (1991). Particle-imaging techniques for experimental fluid mechanics. *Annual Review of Fluid Mechanics*, 23(1):261–304.

Alexander, P. S. and Holman, R. A. (2004). Quantification of nearshore morphology based on video imaging. *Marine geology*, 208(1):101–111.

Almar, R., Bergsma, E. W., Maisongrande, P., and de Almeida, L. P. M. (2019). Wave-derived coastal bathymetry from satellite video imagery: A showcase with pleiades persistent mode. *Remote Sensing of Environment*, 231:111263.

Almar, R., Bonneton, P., Senechal, N., and Roelvink, D. (2009). Wave celerity from video imaging: a new method. In *Coastal Engineering 2008: (In 5 Volumes)*, pages 661–673. World Scientific.

Almar, R., Cienfuegos, R., Catalán, P., Birrien, F., Castelle, B., and Michallet, H. (2011). Nearshore bathymetric inversion from video using a fully non-linear boussinesq wave model. *Journal of Coastal Research*, pages 20–24.

Almar, R., Cienfuegos, R., Catalán, P. A., Michallet, H., Castelle, B., Bonneton, P., and Marieu, V. (2012a). A new breaking wave height direct estimator from video imagery. *Coastal Engineering*, 61:42 – 48.

Almar, R., Larnier, S., Castelle, B., Scott, T., and Floc'h, F. (2016). On the use of the radon transform to estimate longshore currents from video imagery. *Coastal Engineering*, 114:301 – 308.

Almar, R., Ranasinghe, R., Sénéchal, N., Bonneton, P., Roelvink, D., Bryan, K. R., Marieu, V., and Parisot, J.-P. (2012b). Video-based detection of shorelines at complex meso–macro tidal beaches. *Journal of Coastal Research*, 28(5):1040–1048.

Anderson, D., Bak, A. S., Brodie, K. L., Cohn, N., Holman, R. A., and Stanley, J. (2021). Quantifying optically derived two-dimensional wave-averaged currents in the surf zone. *Remote Sensing*, 13(4):690.

Andriolo, U., Sánchez-García, E., and Taborda, R. (2019). Operational use of surfcam online streaming images for coastal morphodynamic studies. *Remote Sensing*, 11(1):78.

Austin, M. J., Scott, T. M., Russell, P. E., and Masselink, G. (2013). Rip current prediction: development, validation, and evaluation of an operational tool. *Journal of coastal research*, 29(2):283–300.

Battjes, J. A. and Janssen, J. (1978). Energy loss and set-up due to breaking of random waves. In *Coastal engineering 1978*, pages 569–587.

Bay, H., Ess, A., Tuytelaars, T., and Gool, L. V. (2008). Speeded-up robust features (surf). *Computer Vision and Image Understanding*, 110(3):346 – 359. Similarity Matching in Computer Vision and Multimedia.

Bell, P. S. (1999). Shallow water bathymetry derived from an analysis of x-band marine radar images of waves. *Coastal Engineering*, 37(3-4):513–527.

Bell, P. S. and Osler, J. C. (2011). Mapping bathymetry using x-band marine radar data recorded from a moving vessel. *Ocean dynamics*, 61(12):2141–2156.

Benedet, L., Pierro, T., and Henriquez, M. (2007). Impacts of coastal engineering projects on the surfability of sandy beaches. *Shore and Beach*, 75(4):3.

Bergsma, E., Conley, D., Davidson, M., and O'Hare, T. (2016). Video-based nearshore bathymetry estimation in macro-tidal environments. *Marine Geology*, 374:31–41.

Bergsma, E. W. and Almar, R. (2018). Video-based depth inversion techniques, a method comparison with synthetic cases. *Coastal Engineering*, 138:199–209.

Bergsma, E. W., Almar, R., de Almeida, L. P. M., and Sall, M. (2019). On the operational use of uavs for video-derived bathymetry. *Coastal Engineering*, 152:103527.

Bergsma, E. W. J. (2017). *Application of an improved video-based depth inversion technique to a macrotidal sandy beach*. PhD thesis, University of Plymouth.

Bian, X., Shao, Y., Zhang, C., Xie, C., and Tian, W. (2020). The feasibility of assessing swell-based bathymetry using sar imagery from orbiting satellites. *ISPRS Journal of Photogrammetry and Remote Sensing*, 168:124–130.

Birkemeier, W. A. and Mason, C. (1984). The crab: A unique nearshore surveying vehicle. *Journal of Surveying Engineering*, 110(1):1–7.

Birrien, F., Castelle, B., Dailloux, D., Marieu, V., Rihouey, D., and Price, T. (2013). Video observation of megacusp evolution along a high-energy engineered sandy beach: Anglet, sw france. *Journal of Coastal Research*, 65(SIv2):1727–1732.

Blenkinsopp, C., Matias, A., Howe, D., Castelle, B., Marieu, V., and Turner, I. (2016). Wave runup and overwash on a prototype-scale sand barrier. *Coastal Engineering*, 113:88 – 103. Barrier Dynamics Experiment II: sediment processes across a large-scale sand barrier.

Bogle, J., Bryan, K., Black, K., Hume, T., and Healy, T. (2001). Video observations of rip formation and evolution. *Journal of Coastal Research*, pages 117–127.

Bonneton, P., Lannes, D., Martins, K., and Michallet, H. (2018). A nonlinear weakly dispersive method for recovering the elevation of irrotational surface waves from pressure measurements. *Coastal Engineering*, 138:1 – 8.

Boudière, E., Maisondieu, C., Ardhuin, F., Accensi, M., Pineau-Guillou, L., and Lepesqueur, J. (2013). A suitable metocean hindcast database for the design of marine energy converters. *International Journal of Marine Energy*, 3:e40–e52.

Bouguet, J.-Y. (2015). Camera calibration toolbox for matlab. Available online: http://www.vision.caltech.edu/bouguetj/calib_doc/, (2015).

Bouvier, C. (2019). *Barres d'avant-côte et trait de côte: dynamique, couplage et effets induits par la mise en place d'un atténuateur de houle*. PhD thesis, Université de Bordeaux.

Bouvier, C., Balouin, Y., Castelle, B., and Holman, R. (2019). Modelling camera viewing angle deviation to improve nearshore video monitoring. *Coastal Engineering*, 147:99 – 106.

Bouvier, C., Balouin, Y., Castelle, B., and Valentini, N. (2020). Video depth inversion at a microtidal site exposed to prevailing low-energy short-period waves and episodic severe storms. *Journal of Coastal Research*, 95(SI):1021–1026.

Bowen, A. and Holman, R. A. (1989). Shear instabilities of the mean longshore current: 1. theory. *Journal of Geophysical Research: Oceans*, 94(C12):18023–18030.

Brodie, K. L., Palmsten, M. L., Hesser, T. J., Dickhudt, P. J., Raubenheimer, B., Ladner, H., and Elgar, S. (2018). Evaluation of video-based linear depth inversion performance and applications using altimeters and hydrographic surveys in a wide range of environmental conditions. *Coastal Engineering*, 136:147–160.

Canny, J. (1986). A computational approach to edge detection. *IEEE Trans. Pattern Anal. Mach. Intell.*, 8(6):679–698.

Castelle, B., Almar, R., Dorel, M., Lefebvre, J.-P., Sénéchal, N., Anthony, E. J., Laibi, R., Chuchla, R., and Penhoat, Y. d. (2014a). Rip currents and circulation on a high-energy low-tide-terraced beach (grand popo, benin, west africa). *Journal of Coastal Research*, (70):633–638.

Castelle, B., Bonneton, P., Senechal, N., Dupuis, H., Butel, R., and Michel, D. (2006). Dynamics of wave-induced currents over an alongshore non-uniform multiple-barred sandy beach on the aquitanian coast, france. *Continental shelf research*, 26(1):113–131.

Castelle, B., Bujan, S., Ferreira, S., and Dodet, G. (2017a). Foredune morphological changes and beach recovery from the extreme 2013/2014 winter at a high-energy sandy coast. *Marine Geology*, 385:41 – 55.

Castelle, B. and Coco, G. (2012). The morphodynamics of rip channels on embayed beaches. *Continental Shelf Research*, 43:10–23.

Castelle, B., Dodet, G., Masselink, G., and Scott, T. (2017b). A new climate index controlling winter wave activity along the atlantic coast of europe: The west europe pressure anomaly. *Geophysical Research Letters*, 44(3):1384–1392.

Castelle, B., Marieu, V., Bujan, S., Ferreira, S., Parisot, J.-P., Capo, S., Sénéchal, N., and Chouzenoux, T. (2014b). Equilibrium shoreline modelling of a high-energy meso-macrotidal multiple-barred beach. *Marine Geology*, 347:85 – 94.

Castelle, B., Marieu, V., Bujan, S., Splinter, K. D., Robinet, A., Sénéchal, N., and Ferreira, S. (2015). Impact of the winter 2013–2014 series of severe western europe storms on a double-barred sandy coast: Beach and dune erosion and megacusp embayments. *Geomorphology*, 238:135 – 148.

Castelle, B., McCarroll, R. J., Brander, R. W., Scott, T., and Dubarbier, B. (2016a). Modelling the alongshore variability of optimum rip current escape strategies on a multiple rip-channelled beach. *Natural Hazards*, 81(1):663–686.

Castelle, B., Michallet, H., Marieu, V., Leckler, F., Dubardier, B., Lambert, A., Berni, C., Bonneton, P., Barthélemy, E., and Bouchette, F. (2010a). Laboratory experiment on rip current circulations over a moveable bed: Drifter measurements. *Journal of Geophysical Research: Oceans*, 115(C12).

Castelle, B., Ruessink, B., Bonneton, P., Marieu, V., Bruneau, N., and Price, T. D. (2010b). Coupling mechanisms in double sandbar systems. part 1: Patterns and physical explanation. *Earth Surface Processes and Landforms*, 35(4):476–486.

Castelle, B., Scott, T., Brander, R., and McCarroll, R. (2016b). Rip current types, circulation and hazard. *Earth-Science Reviews*, 163:1 – 21.

Catálan, P. A. and Haller, M. C. (2008). Remote sensing of breaking wave phase speeds with application to non-linear depth inversions. *Coastal Engineering*, 55(1):93–111.

Chalom, E., Asa, E., and Biton, E. (2013). Measuring image similarity: an overview of some useful applications. *IEEE Instrumentation Measurement Magazine*, 16(1):24–28.

Chang Li and Yangke Liu (2011). Global motion estimation based on sift feature match for digital image stabilization. In *Proceedings of 2011 International Conference on Computer Science and Network Technology*, volume 4, pages 2264–2267.

Chapman, H. R., O'Connor, H., Starek, M. J., and Kar, D. C. (2019). A framework for determination of ocean wave properties using unmanned aerial systems. In *Proceedings of the International Conference on Scientific Computing (CSC)*, pages 35–39. The Steering Committee of The World Congress in Computer Science, Computer ....

Cheng, P. (2020). On residual velocities in sigma coordinates in narrow tidal channels. *Acta Oceanologica Sinica*, 39(5):1–10.

Chickadel, C. C., Holman, R. A., and Freilich, M. H. (2003). An optical technique for the measurement of longshore currents. *Journal of Geophysical Research: Oceans*, 108(C11).

Clarke, T. A. and Fryer, J. G. (1998). The development of camera calibration methods and models. *The Photogrammetric Record*, 16(91):51–66.

Coco, G., Payne, G., Bryan, K. R., Rickard, D., Ramsay, D., and Dolphin, T. (2005). The use of imaging systems to monitor shoreline dynamics. In *1st International Conference on Coastal Zone management and Engineering in the Middle East*.

Cox, D. T. and Anderson, S. L. (2001). Statistics of intermittent surf zone turbulence and observations of large eddies using piv. *Coastal Engineering Journal*, 43(2):121–131.

Davidson, M., Splinter, K., and Turner, I. (2013). A simple equilibrium model for predicting shoreline change. *Coastal Engineering*, 73:191–202.

Davidson, M. and Turner, I. (2009). A behavioral template beach profile model for predicting seasonal to interannual shoreline evolution. *Journal of Geophysical Research: Earth Surface*, 114(F1).

Davidson, M., Van Koningsveld, M., de Kruif, A., Rawson, J., Holman, R., Lamberti, A., Medina, R., Kroon, A., and Aarninkhof, S. (2007). The coastview project: Developing video-derived coastal state indicators in support of coastal zone management. *Coastal Engineering*, 54(6-7):463–475.

De Vries, S., Hill, D., De Schipper, M., and Stive, M. (2011). Remote sensing of surf zone waves using stereo imaging. *Coastal Engineering*, 58(3):239–250.

Didier, D., Bernatchez, P., Augereau, E., Caulet, C., Dumont, D., Bismuth, E., Cormier, L., Floc'h, F., and Delacourt, C. (2017). Lidar validation of a video-derived beachface topography on a tidal flat. *Remote Sensing*, 9(8):826.

Dugan, J., Morris, W., Vierra, K., Piotrowski, C., Farruggia, G., and Campion, D. (2001). Jetski-based nearshore bathymetric and current survey system. *Journal of coastal research*, pages 900–908.

Dérian, P. and Almar, R. (2017). Wavelet-based optical flow estimation of instant surface currents from shore-based and uav videos. *IEEE Transactions on Geoscience and Remote Sensing*, 55(10):5790–5797.

El-gayar, M., Soliman, H., and meky, N. (2013). A comparative study of image low level feature extraction algorithms. *Egyptian Informatics Journal*, 14(2):175 – 181.

Enjalbert, C., Castelle, B., Rihouey, D., and Dailloux, D. (2011). High-frequency video observation of a geologically-constrained barred-beach: La grande plage de biarritz (france). *Journal of Coastal Research*, pages 70–74.

Faig, W. (1975). Calibration of close-range photogrammetric systems: Mathematical formulation. *Photogrammetric engineering and remote sensing*, 41(12).

Fischler, M. A. and Bolles, R. C. (1981). Random sample consensus: A paradigm for model fitting with applications to image analysis and automated cartography. *Commun. ACM*, 24(6):381–395.

Fuchs, R. A. (1953). Depth determination on beaches by wave velocity methods. Technical report, CALIFORNIA UNIV BERKELEY WAVE RESEARCH LAB.

Gao, J. (2009). Bathymetric mapping by means of remote sensing: methods, accuracy and limitations. *Progress in Physical Geography*, 33(1):103–116.

Giddings, S. N., Monismith, S. G., Fong, D. A., and Stacey, M. T. (2014). Using depth-normalized coordinates to examine mass transport residual circulation in estuaries with large tidal amplitude relative to the mean depth. *Journal of physical oceanography*, 44(1):128–148.

Grilli, S. T. (1998). Depth inversion in shallow water based on nonlinear properties of shoaling periodic waves. *Coastal Engineering*, 35(3):185–209.

Guizar-Sicairos, M., Thurman, S. T., and Fienup, J. R. (2007). Efficient image registration algorithms for computation of invariant error metrics. In *Adaptive Optics: Analysis and Methods/Computational Optical Sensing and Imaging/Information Photonics/Signal Recovery and Synthesis Topical Meetings on CD-ROM*, page SMC3. Optical Society of America.

Guizar-Sicairos, M., Thurman, S. T., and Fienup, J. R. (2008a). Efficient subpixel image registration algorithms. *Opt. Lett.*, 33(2):156–158.

Guizar-Sicairos, M., Thurman, S. T., and Fienup, J. R. (2008b). Efficient subpixel image registration by cross-correlation. Available online: https://www.mathworks.com/matlabcentral/fileexchange/18401-efficient-subpixel-image-registration-by-cross-correlation, (accessed on 2 February 2019).

Harley, M., Kinsela, M., Sánchez-García, E. S., and Vos, K. (2018). Coastsnap: Crowdsourced shoreline change mapping using smartphones. In *AGU Fall Meeting Abstracts*, volume 2018, pages EP52D–26.

Harrison, S. R., Bryan, K. R., and Mullarney, J. C. (2017). Observations of morphological change at an ebb-tidal delta. *Marine Geology*, 385:131–145.

Hartley, R. and Zisserman, A. (2004). *Multiple View Geometry in Computer Vision*. Cambridge University Press, 2 edition.

Holland, K. and Holman, R. (1997). Video estimation of foreshore topography using trinocular stereo. *Journal of Coastal Research*, pages 81–87.

Holland, K., Puleo, J., and Kooney, T. (2001). Quantification of swash flows using video-based particle image velocimetry. *Coastal Engineering*, 44(2):65–77.

Holland, K. T. and Holman, R. A. (1999). Wavenumber-frequency structure of infragravity swash motions. *Journal of Geophysical Research: Oceans*, 104(C6):13479–13488.

Holland, K. T., Holman, R. A., Lippmann, T. C., Stanley, J., and Plant, N. (1997). Practical use of video imagery in nearshore oceanographic field studies. *IEEE Journal of Oceanic Engineering*, 22(1):81–92.

Holland, K. T., Palmsten, M. L., et al. (2018). Remote sensing applications and bathymetric mapping in coastal environments. *Advances in Coastal Hydraulics*, pages 375–411.

Holland, T. K. (2001). Application of the linear dispersion relation with respect to depth inversion and remotely sensed imagery. *IEEE Transactions on Geoscience and Remote Sensing*, 39(9):2060–2072.

Holman, R. and Chickadel, C. (2005). Optical remote sensing estimates of the incident wave angle field during ncex. In *Coastal Engineering 2004: (In 4 Volumes)*, pages 1072–1081. World Scientific.

Holman, R. and Haller, M. C. (2013). Remote sensing of the nearshore. *Annual review of marine science*, 5:95–113.

Holman, R., Plant, N., and Holland, T. (2013). cbathy: A robust algorithm for estimating nearshore bathymetry. *Journal of Geophysical Research: Oceans*, 118(5):2595–2609.

Holman, R. and Stanley, J. (2007). The history and technical capabilities of argus. *Coastal Engineering*, 54(6):477 – 491. The CoastView Project: Developing coastal video monitoring systems in support of coastal zone management.

Holman, R. and Stanley, J. (2013). cbathy bathymetry estimation in the mixed wave-current domain of a tidal estuary. *Journal of Coastal Research*, (65):1391–1396.

Holman, R. A., Brodie, K. L., and Spore, N. J. (2017). Surf zone characterization using a small quadcopter: Technical issues and procedures. *IEEE Transactions on Geoscience and Remote Sensing*, 55(4):2017–2027.

Holman, R. A., Sallenger, A. H., Lippmann, T. C., and Haines, J. W. (1993). The application of video image processing to the study of nearshore processes. *Oceanography*, 6(3):78–85.

Holman, R. A., Symonds, G., Thornton, E. B., and Ranasinghe, R. (2006). Rip spacing and persistence on an embayed beach. *Journal of Geophysical Research: Oceans*, 111(C1).

Honegger, D. A., Haller, M. C., and Holman, R. A. (2019). High-resolution bathymetry estimates via x-band marine radar: 1. beaches. *Coastal Engineering*, 149:39–48.

Honegger, D. A., Haller, M. C., and Holman, R. A. (2020). High-resolution bathymetry estimates via x-band marine radar: 2. effects of currents at tidal inlets. *Coastal Engineering*, 156:103626.

Horn, B. K. and Schunck, B. G. (1981). Determining optical flow. In *Techniques and Applications of Image Understanding*, volume 281, pages 319–331. International Society for Optics and Photonics.

Horstmann, J., Stresser, M., and Carrasco, R. (2017). Surface currents retrieved from airborne video. In *OCEANS 2017 - Aberdeen*, pages 1–4.

Hsieh, S. and Kao, C. (2010). A study of the feature-based digital image stabilization system. *Journal of the Chinese Institute of Engineers*, 33(4):635–641.

Huguet, J.-R., Castelle, B., Marieu, V., Morichon, D., and de Santiago, I. (2016). Shoreline-sandbar dynamics at a high-energy embayed and structurally-engineered sandy beach: Anglet, sw france. *Journal of Coastal Research*, 75(SI):393–397.

Ibaceta, R., Almar, R., Lefebvre, J.-P., Mensah-Senoo, T., Laryea, W., Castelle, B., Senechal, N., du Penhoat, Y., Laibi, R., and Hounkonnou, N. (2014). A new high frequency remote sensing based method: application to the swash zone of a very high reflective beach under high energetic conditions (grand popo, benin). *Actes des XIIIèmes Journées Nationales Génie Côtier-Génie Civil*.

Inch, K. (2014). Surf zone hydrodynamics: Measuring waves and currents. *Geomorphological Techniques*, 3:1–13.

Inman, D. L. (2002). Nearshore processes. Retrieved from https://escholarship.org/uc/item/204201x5.

Jackson, D. and Short, A. (2020). *Sandy beach morphodynamics*. Elsevier.

Jin, J. S., Zhigang Zhu, and Guangyou Xu (2000). A stable vision system for moving vehicles. *IEEE Transactions on Intelligent Transportation Systems*, 1(1):32–39.

Jin, J. S., Zhu, Z., and Xu, G. (2001). Digital video sequence stabilization based on 2.5d motion estimation and inertial motion filtering. *Real-Time Imaging*, 7(4):357 – 365.

Johnson, J. (1949). Wave-velocity method of depth determination by aerial photographs. Technical report, CALIFORNIA UNIV BERKELEY INST OF ENGINEERING RESEARCH.

Kalman, R. E. (1960). A new approach to linear filtering and prediction problems.

Kaplan, D. M., Largier, J., and Botsford, L. W. (2005). Hf radar observations of surface circulation off bodega bay (northern california, usa). *Journal of Geophysical Research: Oceans*, 110(C10).

Kimmoun, O. and Branger, H. (2007). A particle image velocimetry investigation on laboratory surf-zone breaking waves over a sloping beach. *Journal of Fluid Mechanics*, 588:353.

Komar, P. D. (1998). Beach processes and sedimentation. prentice hall. *New Jersey*, 539.

Kulkarni, S., Bormane, D., and Nalbalwar, S. (2017). Video stabilization using feature point matching. *Journal of Physics: Conference Series*, 787:012017.

Laporte-Fauret, Q., Marieu, V., Castelle, B., Michalet, R., Bujan, S., and Rosebery, D. (2019). Low-cost uav for high-resolution and large-scale coastal dune change monitoring using photogrammetry. *Journal of Marine Science and Engineering*, 7(3):63.

Lee, Z., Carder, K. L., Mobley, C. D., Steward, R. G., and Patch, J. S. (1999). Hyperspectral remote sensing for shallow waters: 2. deriving bottom depths and water properties by optimization. *Applied optics*, 38(18):3831–3843.

Lim, A., Ramesh, B., Yang, Y., Xiang, C., Gao, Z., and Lin, F. (2017). Real-time optical flow-based video stabilization for unmanned aerial vehicles. *Journal of Real-Time Image Processing*.

Lippmann, T. and Holman, R. (1990). The spatial and temporal variability of sand bar morphology. *Journal of Geophysical Research: Oceans*, 95(C7):11575–11590.

Lippmann, T. C. and Holman, R. A. (1989). Quantification of sand bar morphology: A video technique based on wave dissipation. *Journal of Geophysical Research: Oceans*, 94(C1):995–1011.

Lippmann, T. C. and Holman, R. A. (1991). Phase speed and angle of breaking waves measured with video techniques. In *Coastal Sediments*, pages 542–556. ASCE.

Liu, T. (2017). Openopticalflow: an open source program for extraction of velocity fields from flow visualization images. *Journal of Open Research Software*, 5(1).

Liu, T., Merat, A., Makhmalbaf, M., Fajardo, C., and Merati, P. (2015). Comparison between optical flow and cross-correlation methods for extraction of velocity fields from particle images. *Experiments in Fluids*, 56(8):166.

Liu, T. and Shen, L. (2008). Fluid flow and optical flow. *Journal of Fluid Mechanics*, 614:253–291.

Liu, T., Wang, B., and Choi, D. S. (2012). Flow structures of jupiter's great red spot extracted by using optical flow method. *Physics of Fluids*, 24(9):096601.

Lowe, D. G. (1999). Object recognition from local scale-invariant features. In *Proceedings of the Seventh IEEE International Conference on Computer Vision*, volume 2, pages 1150–1157 vol.2.

Lowe, D. G. (2004). Distinctive image features from scale-invariant keypoints. *International Journal of Computer Vision*, 60(2):91–110.

Lyzenga, D. R., Malinas, N. P., and Tanis, F. J. (2006). Multispectral bathymetry using a simple physically based algorithm. *IEEE Transactions on Geoscience and Remote Sensing*, 44(8):2251–2259.

Lyzenga, G. A. and Ahrens, T. J. (1978). The relation between the shock-induced free-surface velocity and the postshock specific volume of solids. *Journal of Applied Physics*, 49(1):201–204.

MacMahan, J. (2001). Hydrographic surveying from personal watercraft. *Journal of surveying engineering*, 127(1):12–24.

MacMahan, J., Brown, J., Brown, J., Thornton, E., Reniers, A., Stanton, T., Henriquez, M., Gallagher, E., Morrison, J., Austin, M. J., et al. (2010). Mean lagrangian flow behavior on an open coast rip-channeled beach: A new perspective. *Marine Geology*, 268(1-4):1–15.

MacMahan, J., Brown, J., and Thornton, E. (2009). Low-Cost Handheld Global Positioning System for Measuring Surf-Zone Currents. *Journal of Coastal Research*, 2009(253):744 – 754.

MacMahan, J. H., Thornton, E. B., and Reniers, A. J. (2006). Rip current review. *Coastal Engineering*, 53(2-3):191–208.

Madsen, A. and Plant, N. (2001). Intertidal beach slope predictions compared to field data. *Marine Geology*, 173(1):121 – 139.

Mancini, S., Olsen, R. C., Abileah, R., and Lee, K. R. (2012). Automating nearshore bathymetry extraction from wave motion in satellite optical imagery. In *Algorithms and Technologies for Multispectral, Hyperspectral, and Ultraspectral Imagery XVIII*, volume 8390, page 83900P. International Society for Optics and Photonics.

Martins, K., Bonneton, P., and Michallet, H. (2021). Dispersive characteristics of non-linear waves propagating and breaking over a mildly sloping laboratory beach. *Coastal Engineering*, 167:103917.

Martins, K., Bonneton, P., Mouragues, A., and Castelle, B. (2020). Non-hydrostatic, non-linear processes in the surf zone. *Journal of Geophysical Research: Oceans*, 125(2):e2019JC015521.

Masselink, G., Scott, T., Poate, T., Russell, P., Davidson, M., and Conley, D. (2016). The extreme 2013/2014 winter storms: hydrodynamic forcing and coastal response along the southwest coast of england. *Earth Surface Processes and Landforms*, 41(3):378–391.

Matas, J., Krsek, P., Urban, M., Obdrzálek, Š., and Nohỳl, J. (2003). Geometric and photometric image stabilization for detection of significant events in video from a low flying unmanned aerial vehicles. Technical report, Research Report K333–16/03, CTU–CMP–2003–11, Department of Cybernetics ....

McCarroll, R. J., Brander, R. W., Turner, I. L., Power, H. E., and Mortlock, T. R. (2014). Lagrangian observations of circulation on an embayed beach with headland rip currents. *Marine Geology*, 355:173 – 188.

McCarroll, R. J., Masselink, G., Valiente, N. G., Scott, T., King, E. V., and Conley, D. (2018). Wave and tidal controls on embayment circulation and headland bypassing for an exposed, macrotidal site. *Journal of Marine Science and Engineering*, 6(3):94.

Mobley, C. D., Sundman, L. K., Davis, C. O., Bowles, J. H., Downes, T. V., Leathers, R. A., Montes, M. J., Bissett, W. P., Kohler, D. D., Reid, R. P., et al. (2005). Interpretation of hyperspectral remote-sensing imagery by spectrum matching and look-up tables. *Applied Optics*, 44(17):3576–3592.

Mouragues, A., Bonneton, P., Castelle, B., Marieu, V., Barrett, A., Bonneton, N., Detand, G., Martins, K., McCarroll, J., Morichon, D., Poate, T., Padilla, I. R., Scott, T., and Sous, D. (2020a). Field Observations of Wave-induced Headland Rips. *Journal of Coastal Research*, 95(SI):578–582.

Mouragues, A., Bonneton, P., Castelle, B., Marieu, V., Jak McCarroll, R., Rodriguez-Padilla, I., Scott, T., and Sous, D. (2020b). High-energy surf zone currents and headland rips at a geologically constrained mesotidal beach. *Journal of Geophysical Research: Oceans*, 125(10):e2020JC016259. e2020JC016259 10.1029/2020JC016259.

Mouragues, A., Bonneton, P., Lannes, D., Castelle, B., and Marieu, V. (2019). Field data-based evaluation of methods for recovering surface wave elevation from pressure measurements. *Coastal Engineering*, 150:147–159.

Murray, S. P. (01 Apr. 1975). Trajectories and speeds of wind-driven currents wear the coast. *Journal of Physical Oceanography*, 5(2):347 – 360.

Nieto, M. A., Garau, B., Balle, S., Simarro, G., Zarruk, G. A., Ortiz, A., Tintoré, J., Álvarez Ellacuría, A., Gómez-Pujol, L., and Orfila, A. (2010). An open source, low cost video-based coastal monitoring system. *Earth Surface Processes and Landforms*, 35(14):1712–1719.

Novi, L., Raffa, F., and Serafino, F. (2020). Comparison of measured surface currents from high frequency (hf) and x-band radar in a marine protected coastal area of the ligurian sea: Toward an integrated monitoring system. *Remote Sensing*, 12(18):3074.

Oltman-Shay, J., Howd, P., and Birkemeier, W. (1989). Shear instabilities of the mean longshore current: 2. field observations. *Journal of Geophysical Research: Oceans*, 94(C12):18031–18042.

Ortiz Cayon, R. J. (2013). *Online video stabilization for UAV. Motion estimation and compensation for unnamed aerial vehicles*. PhD thesis, Politecnico Di Milano.

Paduan, J. D. and Graber, H. C. (1997). Introduction to high-frequency radar: reality and myth. *oceanography*, 10(2):36–39.

Palmsten, M. L. and Holman, R. A. (2012). Laboratory investigation of dune erosion using stereo video. *Coastal engineering*, 60:123–135.

Palmsten, M. L. and Splinter, K. D. (2016). Observations and simulations of wave runup during a laboratory dune erosion experiment. *Coastal Engineering*, 115:58–66.

Pape, L., Plant, N., and Ruessink, B. (2010). On cross-shore migration and equilibrium states of nearshore sandbars. *Journal of Geophysical Research: Earth Surface*, 115(F3).

Pearre, N. S. and Puleo, J. A. (2009). Quantifying seasonal shoreline variability at rehoboth beach, delaware, using automated imaging techniques. *Journal of Coastal Research*, pages 900–914.

Perkovic, D. (2008). *Radar remote sensing of currents and waves in the nearshore zone*. University of Massachusetts Amherst.

Perkovic, D., Lippmann, T. C., and Frasier, S. J. (2009). Longshore surface currents measured by doppler radar and video piv techniques. *IEEE transactions on geoscience and remote sensing*, 47(8):2787–2800.

Perugini, E., Soldini, L., Palmsten, M. L., Calantoni, J., and Brocchini, M. (2019). Linear depth inversion sensitivity to wave viewing angle using synthetic optical video. *Coastal Engineering*, 152:103535.

Philip, S. and Pang, A. (2016). Detecting and visualizing rip current using optical flow. In *EuroVis (Short Papers)*, pages 19–23.

Pianca, C., Holman, R., and Siegle, E. (2014). Mobility of meso-scale morphology on a microtidal ebb delta measured using remote sensing. *Marine Geology*, 357:334–343.

Pianca, C., Holman, R., and Siegle, E. (2015). Shoreline variability from days to decades: Results of long-term video imaging. *Journal of Geophysical Research: Oceans*, 120(3):2159–2178.

Plant, N., Holman, R., Freilich, M., and Birkemeier, W. (1999). A simple model for interannual sandbar behavior. *Journal of Geophysical Research: Oceans*, 104(C7):15755–15776.

Plant, N. G., Holland, K. T., and Haller, M. C. (2008). Ocean wavenumber estimation from wave-resolving time series imagery. *IEEE Transactions on Geoscience and Remote Sensing*, 46(9):2644–2658.

Plant, N. G. and Holman, R. A. (1997). Intertidal beach profile estimation using video images. *Marine Geology*, 140(1-2):1–24.

Power, H., Holman, R., and Baldock, T. (2011). Swash zone boundary conditions derived from optical remote sensing of swash zone flow patterns. *Journal of Geophysical Research: Oceans*, 116(C6).

Price, T. and Ruessink, B. (2011). State dynamics of a double sandbar system. *Continental Shelf Research*, 31(6):659–674.

Price, T. D. and Ruessink, B. (2013). Observations and conceptual modelling of morphological coupling in a double sandbar system. *Earth Surface Processes and Landforms*, 38(5):477–489.

Puleo, J. and Holland, K. (2000). Field observations of three-dimensional swash flow patterns and morphodynamics. In *Proceedings of the 27th International Conference on Coastal Engineering*, pages 637–650.

Puleo, J. A., Farquharson, G., Frasier, S. J., and Holland, K. T. (2003). Comparison of optical and radar measurements of surf and swash zone velocity fields. *Journal of Geophysical Research: Oceans*, 108(C3).

Quartel, S. (2009). Temporal and spatial behaviour of rip channels in a multiple-barred coastal system. *Earth Surface Processes and Landforms*, 34(2):163–176.

Radermacher, M., Wengrove, M., van Thiel de Vries, J., and Holman, R. (2014). Applicability of video-derived bathymetry estimates to nearshore current model predictions. *Journal of Coastal Research*, (70):290–295.

Rawat, P. and Singhai, J. (2011). Review of motion estimation and video stabilization techniques for hand held mobile video. *Signal & Image Processing: An International Journal (SIPIJ) Vol*, 2.

Rijn, L. C. (2007). *Manual sediment transport measurements in rivers, estuaries and coastal seas*. Aqua publications.

Rodríguez-Padilla, I., Castelle, B., Marieu, V., Bonneton, P., Mouragues, A., Martins, K., and Morichon, D. (2021). Wave-filtered surf zone circulation under high-energy waves derived from video-based optical systems. *Remote Sensing*, 13(10):1874.

Rodriguez-Padilla, I., Castelle, B., Marieu, V., and Morichon, D. (2020). A simple and efficient image stabilization method for coastal monitoring video systems. *Remote Sensing*, 12(1):70.

Rosten, E. and Drummond, T. (2005). Fusing points and lines for high performance tracking. *Tenth IEEE International Conference on Computer Vision (ICCV'05) Volume 1*, 2:1508–1515 Vol. 2.

Ruessink, B., Pape, L., and Turner, I. (2009). Daily to interannual cross-shore sandbar migration: Observations from a multiple sandbar system. *Continental Shelf Research*, 29(14):1663–1677.

Rutten, J., de Jong, S. M., and Ruessink, G. (2016). Accuracy of nearshore bathymetry inverted from x-band radar and optical video data. *IEEE Transactions on Geoscience and Remote Sensing*, 55(2):1106–1116.

Schmidt, W. E., Woodward, B. T., Millikan, K. S., Guza, R. T., Raubenheimer, B., and Elgar, S. (01 Jul. 2003). A gps-tracked surf zone drifter. *Journal of Atmospheric and Oceanic Technology*, 20(7):1069 – 1075.

Schwendeman, M. and Thomson, J. (2015). A horizon-tracking method for shipboard video stabilization and rectification. *Journal of Atmospheric and Oceanic Technology*, 32(1):164–176.

Scott, T., Austin, M., Masselink, G., and Russell, P. (2016). Dynamics of rip currents associated with groynes â€" field measurements, modelling and implications for beach safety. *Coastal Engineering*, 107:53 – 69.

Scott, T., Castelle, B., Almar, R., Senechal, N., Floc'h, F., and Detandt, G. (2018). Controls on flash rip current hazard on low-tide terraced tropical beaches in west africa. *Journal of Coastal Research*, (81):92–99.

Senechal, N., Coco, G., Bryan, K. R., and Holman, R. A. (2011). Wave runup during extreme storm conditions. *Journal of Geophysical Research: Oceans*, 116(C7).

Shand, T. D., Bailey, D. G., and Shand, R. D. (2012). Automated detection of breaking wave height using an optical technique. *Journal of Coastal Research*, 28(3):671–682.

Short, A. D. and Masselink, G. (1999). Embayed and structurally controlled beaches. *Handbook of beach and shoreface morphodynamics*, 1(999):230–249.

Simarro, G., Calvete, D., Luque, P., Orfila, A., and Ribas, F. (2019). Ubathy: A new approach for bathymetric inversion from video imagery. *Remote Sensing*, 11(23):2722.

Simm, J. D., Brampton, A., Beech, N., and Brooke, J. (1996). *Beach management manual*. CIRIA London.

Sous, D., Castelle, B., Mouragues, A., and Bonneton, P. (2020). Field measurements of a high-energy headland deflection rip current: Tidal modulation, very low frequency pulsation and vertical structure. *Journal of Marine Science and Engineering*, 8(7).

Souza, M. R. and Pedrini, H. (2018). Digital video stabilization based on adaptive camera trajectory smoothing. *EURASIP Journal on Image and Video Processing*, 2018(1):37.

Splinter, K. D., Gonzalez, M. V., Oltman-Shay, J., Rutten, J., and Holman, R. (2018a). Observations and modelling of shoreline and multiple sandbar behaviour on a high-energy meso-tidal beach. *Continental Shelf Research*, 159:33–45.

Splinter, K. D., Harley, M. D., and Turner, I. L. (2018b). Remote sensing is changing our view of the coast: Insights from 40 years of monitoring at narrabeen-collaroy, australia. *Remote Sensing*, 10(11).

Splinter, K. D., Holman, R. A., and Plant, N. G. (2011a). A behavior-oriented dynamic model for sandbar migration and 2dh evolution. *Journal of Geophysical Research: Oceans*, 116(C1).

Splinter, K. D., Strauss, D. R., and Tomlinson, R. B. (2011b). Assessment of post-storm recovery of beaches using video imaging techniques: A case study at gold coast, australia. *IEEE Transactions on geoscience and remote sensing*, 49(12):4704–4716.

Splinter, K. D., Turner, I. L., Davidson, M. A., Barnard, P., Castelle, B., and Oltman-Shay, J. (2014). A generalized equilibrium model for predicting daily to interannual shoreline response. *Journal of Geophysical Research: Earth Surface*, 119(9):1936–1958.

Splinter, K. D., Turner, I. L., Reinhardt, M., and Ruessink, G. (2017). Rapid adjustment of shoreline behavior to changing seasonality of storms: observations and modelling at an open-coast beach. *Earth Surface Processes and Landforms*, 42(8):1186–1194.

Stockdon, H. and Holman, R. (1996). Accuracy of depth estimation techniques based on video observations of wave celerity. *Transactions, American Geophysical Union*, 77:399.

Stockdon, H. F. and Holman, R. A. (2000). Estimation of wave phase speed and nearshore bathymetry from video imagery. *Journal of Geophysical Research: Oceans*, 105(C9):22015–22033.

Streßer, M., Carrasco, R., and Horstmann, J. (2017). Video-based estimation of surface currents using a low-cost quadcopter. *IEEE Geoscience and Remote Sensing Letters*, 14(11):2027–2031.

Szeliski, R. (2010). *Computer vision: algorithms and applications*. Springer Science & Business Media.

Sánchez-García, E., Balaguer-Beser, A., and Pardo-Pascual, J. (2017). C-pro: A coastal projector monitoring system using terrestrial photogrammetry with a geometric horizon constraint. *ISPRS Journal of Photogrammetry and Remote Sensing*, 128:255 – 273.

Taborda, R. and Silva, A. (2012). Cosmos: A lightweight coastal video monitoring system. *Computers & Geosciences*, 49:248–255.

Tareen, S. A. K. and Saleem, Z. (2018). A comparative analysis of sift, surf, kaze, akaze, orb, and brisk. In *2018 International Conference on Computing, Mathematics and Engineering Technologies (iCoMET)*, pages 1–10.

Thielicke, W. and Stamhuis, E. (2014). Pivlab–towards user-friendly, affordable and accurate digital particle image velocimetry in matlab. *Journal of open research software*, 2(1).

Thornton, E. B. and Guza, R. (1982). Energy saturation and phase speeds measured on a natural beach. *Journal of Geophysical Research: Oceans*, 87(C12):9499–9508.

Thuan, D. H., Almar, R., Marchesiello, P., and Viet, N. T. (2019). Video sensing of nearshore bathymetry evolution with error estimate. *Journal of Marine Science and Engineering*, 7(7):233.

Tolman, H. L. (1991). A third-generation model for wind waves on slowly varying, unsteady, and inhomogeneous depths and currents. *Journal of Physical Oceanography*, 21(6):782–797.

Torii, A., Havlena, M., and Pajdla, T. (2011). Omnidirectional image stabilization for visual object recognition. *International Journal of Computer Vision*, 91(2):157–174.

Tsai, R. (1987). A versatile camera calibration technique for high-accuracy 3d machine vision metrology using off-the-shelf tv cameras and lenses. *IEEE Journal on Robotics and Automation*, 3(4):323–344.

Turaga, P., Chellappa, R., and Veeraraghavan, A. (2010). Advances in video-based human activity analysis: Challenges and approaches. In Zelkowitz, M. V., editor, *Advances in Computers*, volume 80 of *Advances in Computers*, pages 237 – 290. Elsevier.

Turner, I. L. (2006). Discriminating modes of shoreline response to offshore-detached structures. *Journal of waterway, port, coastal, and ocean engineering*, 132(3):180–191.

Turner, I. L., Whyte, D., Ruessink, B., and Ranasinghe, R. (2007). Observations of rip spacing, persistence and mobility at a long, straight coastline. *Marine Geology*, 236(3):209 – 221.

Uunk, L., Wijnberg, K. M., and Morelissen, R. (2010). Automated mapping of the intertidal beach bathymetry from video images. *Coastal engineering*, 57(4):461–469.

van Dongeren, A., Plant, N., Cohen, A., Roelvink, D., Haller, M. C., and Catalán, P. (2008). Beach wizard: Nearshore bathymetry estimation through assimilation of model computations and remote observations. *Coastal Engineering*, 55(12):1016 – 1027.

Van Enckevort, I. and Ruessink, B. (2003). Video observations of nearshore bar behaviour. part 2: alongshore non-uniform variability. *Continental Shelf Research*, 23(5):513–532.

van Enckevort, I. M. J., Ruessink, B. G., Coco, G., Suzuki, K., Turner, I. L., Plant, N. G., and Holman, R. A. (2004). Observations of nearshore crescentic sandbars. *Journal of Geophysical Research: Oceans*, 109(C6).

Van Son, S., Lindenbergh, R., De Schipper, M., De Vries, S., and Duijnmayer, K. (2009). Using a personal watercraft for monitoring bathymetric changes at storm scale. In *Hydro9 Conference, 10-12 November 2009, Cape Town, South Africa*.

Vieira, M., Guimarães, P. V., Violante-Carvalho, N., Benetazzo, A., Bergamasco, F., and Pereira, H. (2020). A low-cost stereo video system for measuring directional wind waves. *Journal of Marine Science and Engineering*, 8(11).

Vousdoukas, M., Pennucci, G., Holman, R., and Conley, D. (2011a). A semi automatic technique for rapid environmental assessment in the coastal zone using small unmanned aerial vehicles (suav). *Journal of Coastal Research*, pages 1755–1759.

Vousdoukas, M. I., Ferreira, P. M., Almeida, L. P., Dodet, G., Psaros, F., Andriolo, U., Taborda, R., Silva, A. N., Ruano, A., and Ferreira, Ó. M. (2011b). Performance of intertidal topography video monitoring of a meso-tidal reflective beach in south portugal. *Ocean Dynamics*, 61(10):1521–1540.

Wang, B., Cai, Z., Shen, L., and Liu, T. (2015). An analysis of physics-based optical flow. *Journal of Computational and Applied Mathematics*, 276:62 – 80.

Wang, R. and Tao, D. (2016). Non-local auto-encoder with collaborative stabilization for image restoration. *IEEE Transactions on Image Processing*, 25(5):2117–2129.

Wang, Y. M., Li, Y., and Zheng, J. B. (2010). A camera calibration technique based on opencv. In *The 3rd International Conference on Information Sciences and Interaction Sciences*, pages 403–406.

Wengrove, M. E., Henriquez, M., De Schipper, M. A., Holman, R., and Stive, M. (2013). Monitoring morphology of the sand engine leeside using argus' cbathy. In *Coastal Dynamics 2013: 7th International Conference on Coastal Dynamics, Arcachon, France, 24-28 June 2013*. Bordeaux University.

Williams, W. (1947). The determination of gradients on enemy-held beaches. *The Geographical Journal*, 109(1/3):76–90.

Wilson, G. and Berezhnoy, S. (2018). Surfzone state estimation, with applications to quadcopter-based remote sensing data. *Journal of Atmospheric and Oceanic Technology*, 35(10):1881–1896.

Wilson, G., Özkan-Haller, H., Holman, R., Haller, M., Honegger, D., and Chickadel, C. (2014). Surf zone bathymetry and circulation predictions via data assimilation of remote sensing observations. *Journal of Geophysical Research: Oceans*, 119(3):1993–2016.

Wilson, G. W., Özkan-Haller, H., and Holman, R. (2010). Data assimilation and bathymetric inversion in a two-dimensional horizontal surf zone model. *Journal of Geophysical Research: Oceans*, 115(C12).

Winckler, P. (2020). *Introducción al modelado de procesos costeros (V2, 2020)*.

Wright, L. and Short, A. (1984). Morphodynamic variability of surf zones and beaches: A synthesis. *Marine Geology*, 56(1):93 – 118.

Wright, L. and Thom, B. (1977). Coastal depositional landforms: a morphodynamic approach. *Progress in Physical Geography*, 1(3):412–459.

Young, I. R., Rosenthal, W., and Ziemer, F. (1985). A three-dimensional analysis of marine radar images for the determination of ocean wave directionality and surface currents. *Journal of Geophysical Research: Oceans*, 90(C1):1049–1059.

Zhao, Z., Ye, D., Zhang, X., Chen, G., and Zhang, B. (2016). Improved direct linear transformation for parameter decoupling in camera calibration. *Algorithms*, 9(2).

Appendix

Contents

A Optical flow algorithm setup

The relevant parameters used for Liu (2017) OpenOpticalFlow algorithm are listed in Table A.1.

As previously mentioned in subsection 5.3.3, OpenOpticalFlow uses the Horn-Schunck estimator for an initial solution and the Liu-Shen estimator for a refined solution of Eq. 5.3. The term $f(x_1, x_2, I)$ depends on a specific flow visualization. For a transport of a scalar (i.e. foam concentration), it is related to the molecular diffusion plus the boundary term. For simplicity, we defined $f(x_1, x_2, I) = 0$, a reasonable approximation for most fluid mechanics problems where the convection is dominant as shown in Liu and Shen (2008); Liu (2017). The Lagrange multipliers "lambda_1" and "lambda_2" (λ in Eq. 5.5 and 5.3) are selected for the Horn-Schunck and Liu-Shen estimators, respectively. The Lagrange multipliers act like a diffusion coefficient in the corresponding Euler-Lagrange equations (Eq. 5.3 and 5.5) and tend to smooth out finer flow structures (Liu et al., 2012, 2015; Liu, 2017). There is no rigorous theory for determining the Lagrange multiplier in the variational formulation of the optical flow equation. Within a considerable range of the Lagrange multipliers, the solution is not significantly sensitive to its selection (Liu and Shen, 2008; Liu et al., 2012, 2015; Liu, 2017; Wang et al., 2015).

The pixel displacement between frames should be small (typically less than 5 px depending on the size of image patterns (Liu, 2017)). Otherwise, the time derivative of the image intensity will be underestimated in the finite difference method and the optical flow error would be significant (Liu et al., 2012). To handle large displacements (e.g., >10 px), a coarse-to-fine iterative scheme is adopted to improve the accuracy of optical flow computation (Liu, 2017). First, the raw images are downsampled by a suitable scale factor (parameter called "scale_im") using the wavelet transform (Dérian and Almar, 2017) so that the displacements in pixels remain small enough (1-5 px). Next, the optical flow algorithm is applied to the downsampled images to estimate a coarse-grained velocity field. Finally, the original resolution velocity field is recovered by iterations (parameter called "no_iteration") using an image-shifting (image-warping) algorithm with an embedded spatial interpolation scheme (Liu et al., 2015). Usually, one or two iterations are sufficient (Liu, 2017). In addition to the main program, (Liu, 2017) OpenOpticalFlow include two image pre-processing routines (Gaussian filters) for removing small random noise and correcting the effect of local illumination intensity change. The mask size of the Gaussian filter is given by the parameter called "size_filter" and the standard deviation of the Gaussian filter is 0.6 of the mask size. The standard deviation (or size) of the Gaussian filter is given by the parameter called "size_average" in the program. A full description of the parameters and subroutines involved in the usage of OpenOpticalFlow can be found in (Liu, 2017).

For this study, the Lagrange multipliers in the Horn-Schunck and Liu-Shen estimators were set at 20 and 2000, respectively. In the coarse-to-fine scheme, raw images were initially downsampled by 2 (reduced to 50% of their original size) and then refined to their original resolution by the first iteration. The mask sizes of the Gaussian filter for removing small random noise was set to 4 px in the raw images, while the standard deviation of the Gaussian filter was set at 60% of the mask size. The mask size of the filter for correcting the effect of the changing illumination intensity was fixed at 30 px for the raw images (Table A.1).

Table A.1 – Optical flow input parameters and settings.

Parameter	**Notation**	**Value**	**Note**
Lagrange multipliers	lambda_1 for the Horn-Schunk estimator	20	regularization parameters in
	lambda_2 for the Liu-Shen estimator	2000	variational solution
scale factor for downsampling of raw images	scale_im	0.5	reduction of initial image size in coarse-to-fine scheme
number of iterations	no_iteration	1	iteration in coarse-to-fine scheme
Gaussian filter size	size_filter	4 px	removing random image noise
Gaussian filter size	size_average	30 px	correction for local illumination intensity change